UiT
THE ARCTIC UNIVERSITY OF NORWAY

FACULTY OF SCIENCE AND TECHNOLOGY

Department of Geosciences

Shallow gas accumulations and fluid flow in the vicinity of the Goliat field, SW Barents Sea

Renate Strugstad Paulsen

Master's thesis in Geology, GEO-3900

May 2017

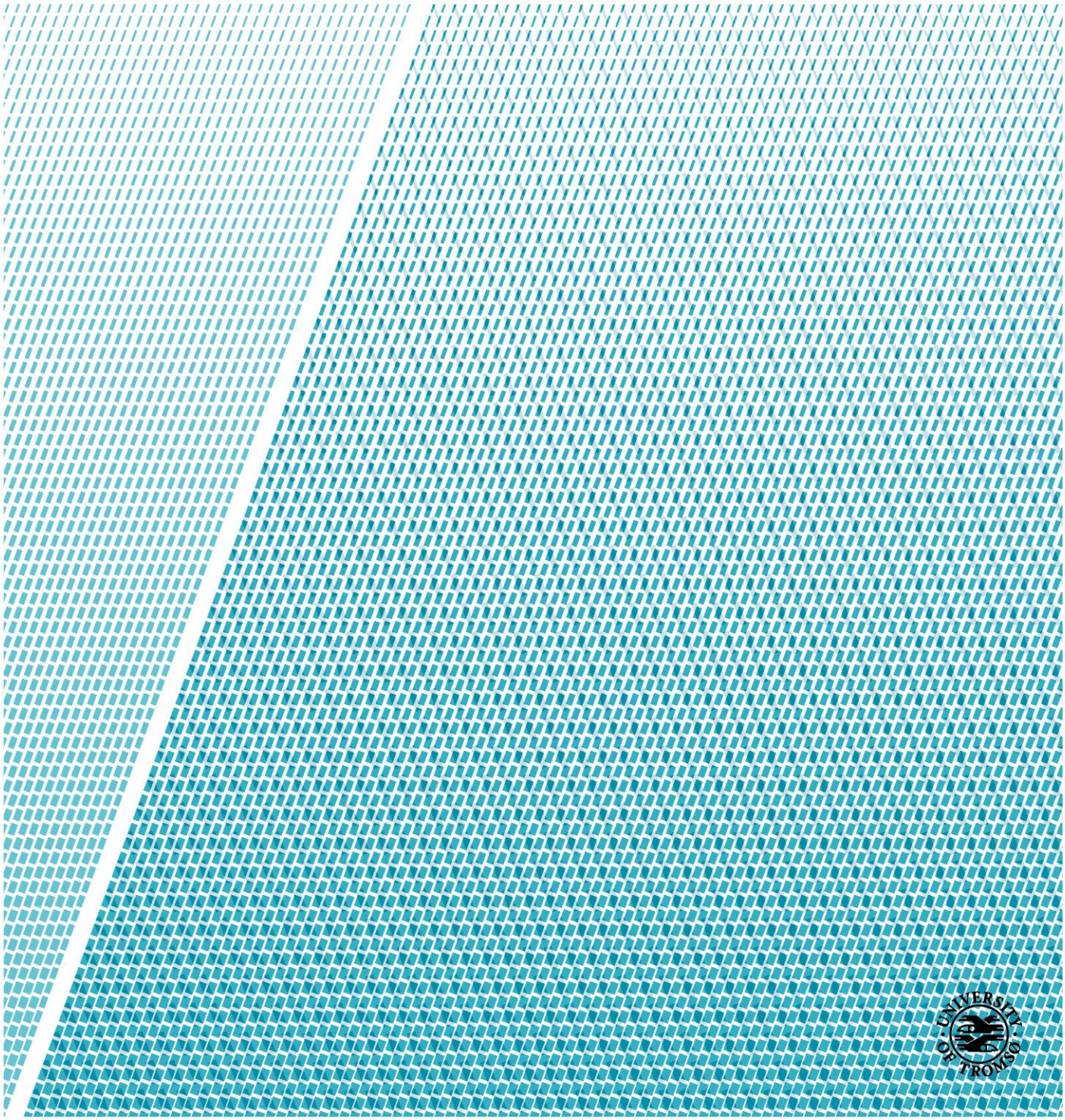

Abstract

This thesis focuses on the Goliat area located in the Hammerfest Basin, SW Barents Sea. The overall aim of this study is to increase the understanding of fluid flow processes between deeper thermogenic sources, and shallow gas accumulations. Indications of an active fluid flow system has been observed throughout the southwestern Barents Sea. Much of the fluid flow from deep hydrocarbon reservoirs has been associated with the denudation history of the Barents Sea. Well-known fluid flow features like pipes or pockmarks appear on seismic images and multibeam bathymetry data and provide evidence for fluid migration. A single seismic data set from the Goliat field area, provided by Eni Norge, has been interpreted for possible indications of fluid flow features and shallow gas accumulation.

This study focusses mostly on the sedimentary formations above the Base Cretaceous Unconformity (BCU). Two main sets of faults are categorized: deep-seated faults extending downwards from the BCU and into the Permian strata, and shallow faults affecting the Kolmule and Torsk Formations. Within the shallow faults, two different sets of polygonal faults are interpreted. One polygonal fault system affecting only a small interval within the lower Kolmule Formation, and the other is a set of reactivated polygonal faults affecting both the Kolmule and Tosk Formations.

As the SW Barents Sea has undergone several phases of uplift and erosion, different sets of faults have been active at different times. The change and orientation of lithospheric stress causes different sets of faults to be open as potential fluid migration pathways. This makes it possible for fluids to migrate and accumulate at different stratigraphic levels in the subsurface. Pockmarks and fluid flow features above the upper regional unconformity (URU) implies an active fluid flow system after the Plio-Pleistocene glaciation.

Amplitude anomalies are often associated with the presence of free gas in the subsurface. The presence and distribution of amplitude anomalies in this work indicates that there is a relation between the deeper-lying hydrocarbon reservoirs and both deep-seated and shallow faults. The observation of pockmarks on the seafloor increases the possibility of free gas to be present in the area.

Acknowledgement

I would like to first thank my supervisor, Associate Professor Stefan Bünz for making it possible for me to write this thesis, and for providing me with the necessary resources to complete the research. His help and guidance when it comes to the seismic, writing and the Petrel software has been invaluable.

Further, I would like to thank Eni Norge for giving me the opportunity to work as a summer intern, and for providing me with the seismic dataset for this thesis. A special thanks to Lead Geophysicist Johan Leutscher at Eni, for being a mentor and always being available when I have needed help, or had questions about the seismic dataset.

My peers from UiB, UiT and friends, you know who you are, and I could never have done this without the many coffee-, lunch breaks and pizza meetings. Ane, thank you for providing me with coffee every morning at the office, I will be forever in debt, and Lene for making my one-man office a dual office and for making sure that I actually get work done.

A note of mention to CAGE (Centre for Arctic Gas Hydrate, Environment and Climate) for inviting me to join the seismic acquisition cruise with R/V Helmer Hanssen last summer, introducing me to on-board seismic processing and the practical work behind acquiring seismic. It was such an interesting and fun experience. A special thanks to Malin here, for proofreading my thesis and helping me with the structuring.

Finally, I would give my sincere appreciation to my father, John Eirik Paulsen, who helped tremendously with his academic input, and who encouraged me to study geology. My sister Maryon, for always helping me with her geological and academic background and my mum, Ingrid for always being just a short phone call away when I needed it. A special thanks to my better half for correcting my English and encouraging me at all times. Thank you for taking me camping and sledding with your dogs. It really helpt me keep my mind at the right place, and providing the much-needed “off-time” from the office.

Renate Strugstad Paulsen

Tromsø, Mai 2017

Contents

1 Introduction

The following chapter and subchapters are meant as an introduction to the theory behind the later results and findings. The results and findings will then be incorporated in the discussion at the end. The structure of this thesis is built up around the theory of faults and how faults may act as conduits for fluids in the subsurface. It has therefore been necessary to link the theory of faults to fluid flow in the subsurface, and how they may relate to shallow gas accumulations. To do this, seismic data provided by Eni Norge has been studied and interpreted, with focus on extracting different attribute maps to enhance amplitude anomalies and faults in the subsurface.

1.1 Objectives

The main focus of this master thesis is to map the occurrences of shallow fluid flow features such as shallow gas accumulations, leakage features and indicators of gas hydrates on the southcentral border of the Goliat Field in SW Barents Sea (Fig 1.1). This thesis defines "shallow" as any feature above the Base Cretaceous Unconformity. Another important focus is to establish an understanding of the stratigraphy and the structural features here and in the overburden of the Goliat Field. Previous studies from the area (e.g. Chand et al. (2009) and Ostanin et al. (2012) suggests that there is a dynamic fluid flow system in the area. The objective of this thesis is to improve our understanding of the origin and controlling mechanisms for the occurrences and development of shallow gas accumulations, focussed fluid flow features along faults and/or as chimneys and pipe structures, and potential gas hydrate occurrence in the area. The study will also investigate any potential relationship with the structural development and the denudation history of the study area, as well as a potential link with the deep-seated hydrocarbon reservoirs. The study is carried out by interpreting 3D seismic data and well-log data for correlation of stratigraphic units. The 3D seismic data set is located in the southwest Barents Sea at the southwest margin of the Hammerfest Basin, near the Finnmark Platform (Fig. 1.1). Seismic attributes will be used to visualize and map both the vertical and lateral distributions of the different structural elements and fluid flow features in the area.

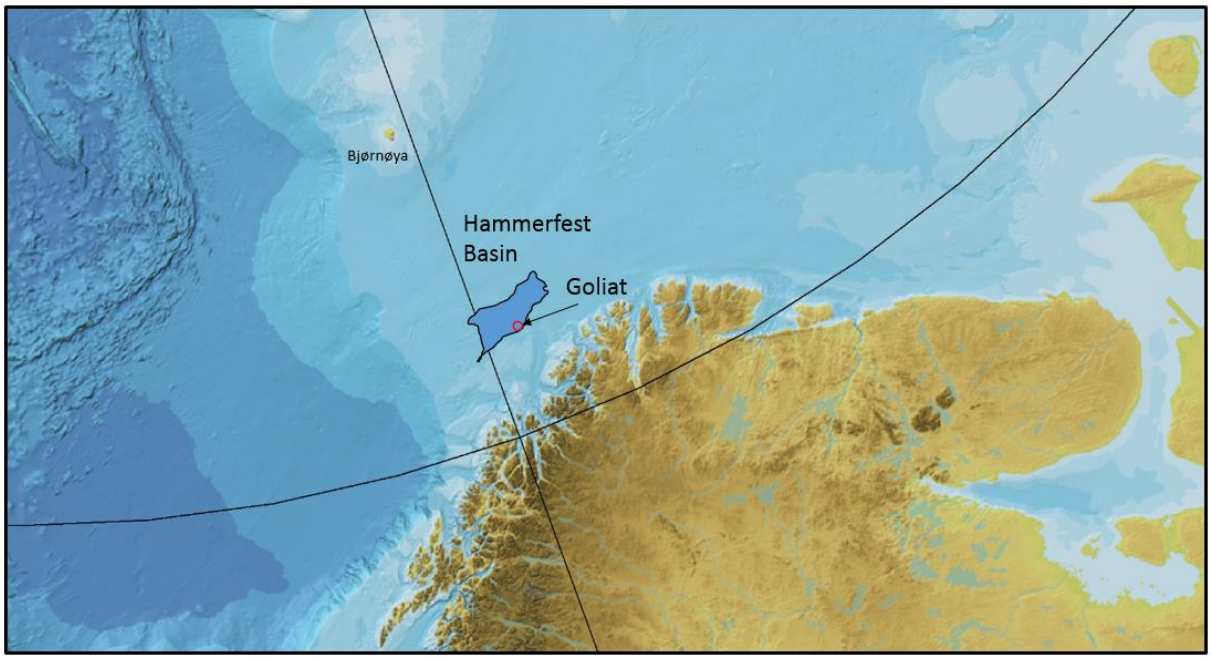

Figure 1.1 *Overview of the Barents Sea and the location of Goliat within the Hammerfest Basin. Map is obtained from the Atlas of Submarine Glacial Landforms*

1.2 Faults

Faults often play an important role regarding focused fluid flow activity. The southwestern Barents Sea has been tectonically active several times in the past, leading to a complex structural setting, with development of different set of faults affecting different stratigraphic levels. Although not the primary focus of the work, it is therefore also important to map and interpret their distribution on the seismic, and investigate their relationship to fluid flow activity.

1.2.1 Understanding faults

Faults can be described as a discontinuity, or a narrow zone with shear displacement along it. The definition of faults bears similarities (and are sometimes used synonymously) with fractures, but often we refer to faults as composite structures who display offsets of more than one meter (Fossen and Gabrielsen, 2005). Both fractures and faults can play an important role as migration pathways for fluids. The migration of fluids along fault planes allows deeper-seated reservoir to expel fluids to higher-level stratigraphy, and in some cases to the sea floor. Faults, however, can be challenging to interpret correct on seismic data, which makes an understanding of the regional tectonic regime in the area and expected structures important in

addition to a basic understanding of general fault behaviour. Also important is a possible study of exposed analogues if accessible.

1.2.2 Fault types

Faults are usually classified based on the dip angle of the fault plane and the relative direction and displacement of it. A fault with a fault surface dipping more than 45° is a high angle fault, and if the fault surface dip is less than 45° it is a low angle fault. Faults are also categorised by the relative displacement, which means the net distance and direction the hanging wall and footwall will move with respect to another. Dip-slip faults will have movement parallel to the fault surface, Strike-slip faults have approx. parallel to horizontal movement to the strike of the fault surface, while oblique-slip faults will have slip inclined obliquely on the fault surface (Twiss and Moores, 1992). In addition, the relative movement of the fault blocks decides whether it is a reverse or thrust fault where the hanging wall moves up relative to the footwall (contraction faults), or a normal fault where the hanging wall moves down relative to the hanging wall (extension faults). Generally, normal faults will have a steeper angle than reverse faults.

The different type of faults mentioned above, all have different orientations of the principal stresses (stress regime). Anderson (1951) theorized that in all different tectonic stress regimes (extensional, compressional or strike-slip), there would be one horizontal and two vertical principal stresses, considering that there is no shear stress at the earth's surface. The fault regime can then be determined by considering which of the principal stress orientation are vertical (Fig 1.2) (Fossen, 2016).

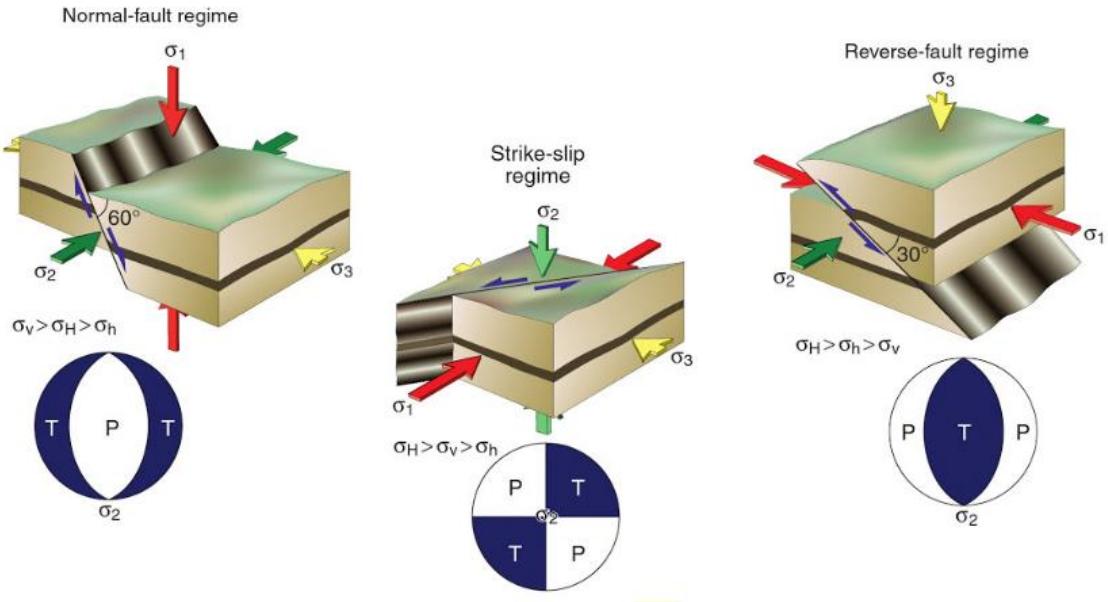

Figure 1.2 *The figure illustrates the Anderson's classification of three different fault regimes, normal (extensional), Strike-slip and reverse (compressional) and the relationship to the principal stresses' orientation. Fields of compression (P) and tension (T) is shown as spherical projections.* σ_v *= vertical stress,* σ_h *= minimum horizontal stress,* σ_H *= maximum horizontal stress. Figure after Fossen (2016).*

1.2.3 Fault initiation and reactivation:

In the sub-surface, the rocks will experience stress from all directions, which will give rise to a stress field. The stress field is best represented as an infinite number of traction vector of any possible orientation. The stress on a surface is a vector, σ; defined by the relationship between the force and the area the force is acting upon. The stress can change from place to place on a surface. The two main stress vectors are the normal stress σ_n where the vector is oriented normal to the surface, and the shear stress σ_s, where the vector runs parallel with the surface. If the effective stress overcomes the internal strength of the rock, it will fracture (Fig. 1.5) (Fossen and Gabrielsen, 2005).

In three dimensions, there will be three stress components acting on each of the surfaces of a cube. To simplify this, the nine stress vector components are presented in a 2nd order stress tensor matrix (equation 1.1). The stress components are shown visually in Fig. 1.3 Here, all the normal stress components are found along the diagonal (σ_{11}, σ_{22}, σ_{33}) and the shear stress components are under and above this diagonal (Fossen and Gabrielsen, 2005).

$$\begin{vmatrix} \sigma_{xx} & \sigma_{xy} & \sigma_{xz} \\ \sigma_{yx} & \sigma_{yy} & \sigma_{yz} \\ \sigma_{zx} & \sigma_{zy} & \sigma_{zz} \end{vmatrix} = \begin{vmatrix} \sigma_{11} & \sigma_{12} & \sigma_{13} \\ \sigma_{21} & \sigma_{22} & \sigma_{23} \\ \sigma_{31} & \sigma_{32y} & \sigma_{33} \end{vmatrix} \qquad (Equation\ 1.1)$$

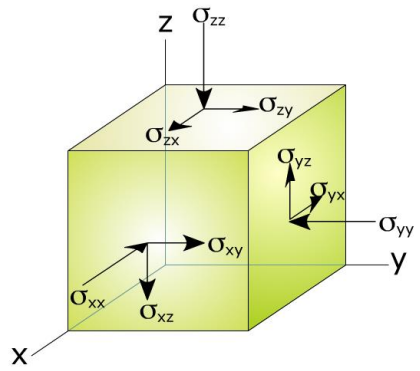

Figure 1.3 *Stress components working on each of the surfaces of a cube. Only the positive stress components are shown in the figure. Equal components with negative notation is found on the surfaces not visible on this figure. σ_{xx}, σ_{yy} and σ_{zz} are normal stresses, the others represents the shear stresses along the axis. Figure from Fossen and Gabrielsen (2005)*

1.2.4 Mohr's circle.

The Mohr diagram is a convenient and simple way to display the stress acting on any given point at a surface by putting the principal stress components (σ_1- σ_3) in a diagram where the vertical axis represents the shear stress σs, and the horizontal axis represents the normal stress, σ_n. Principal stress components are plotted on the horizontal axis, where σ_1 is the maximum principal stress and σ_3 is the minimum stress component. The distance between σ_1 and σ_3 forms the diameter in a circle with centre $((\sigma_1+\sigma_3)/2)$ (Fig. 1.4). This gives the stress field in two dimensions, and it is possible to find the shear stress acting upon any surface containing σ_2. The diameter of the circle is determined by σ_1- σ_3 and it also represents the differential stress, which decides whether the rock will fracture or not.

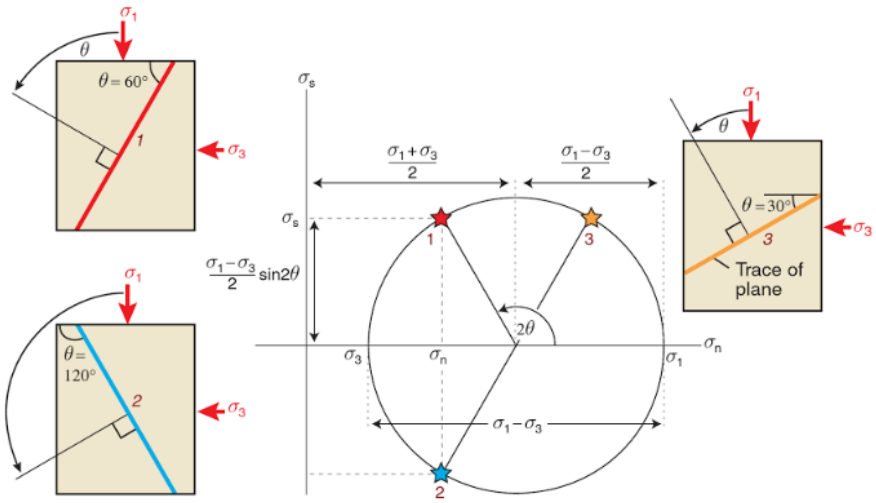

Figure 1.4 *Illustration of the Mohr's circle. The θ shows the angle between the largest stress axis and the normal of a chosen plane. Note that the angles are doubled. Figure after Fossen (2016).*

Whether a rock finds itself in a stable or unstable condition depends on the failure envelope. The Coulomb failure criteria predicts when a rock with given physical properties will fracture. If the Mohr circle touches the envelope it will be in a critical state, and if it crosses the envelope, the state of stress is unstable, the rock cannot withstand the stress, and thus it fractures. It is therefore not possible for a rock to cross the envelope, and the state of stress is said to be impossible (Twiss and Moores, 1992).

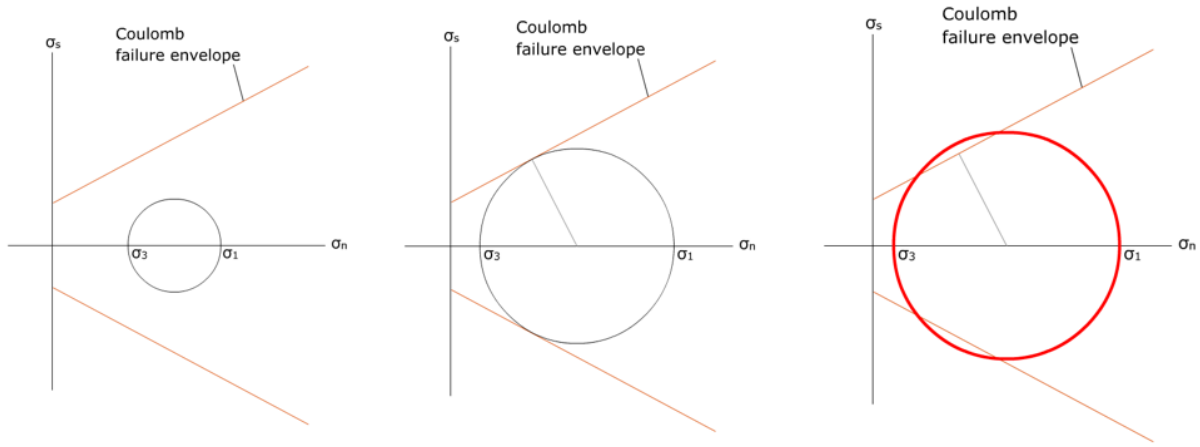

Figure 1.5 a) *stable stress situation given the failure criteria shown in the Mohr diagram.* ***b)*** *Critical situation where the Mohr's circle tangents the line representing the failure criteria.* ***c)*** *Unstable and impossible stress situation. The rock with fail before this situation can occur. Figure is modified after Fossen and Gabrielsen (2005)*

Coulombs failure criterion given in equation 1.2 shows how failures occur in brittle and porous rocks.

$$\sigma_s = C + \sigma_n tan\phi \qquad (Equation\ 1.2)$$

Here, the σs and σn are the normal and shear stresses acting on a potential fracture plane in the moment of initiation of the fracture. C is the rocks cohesion, describing the critical shear stress needed to initiate shear movement along a plane oriented so that the σ_n on the plane equals zero. It is also known as the rocks uniaxial compressive strength. The ϕ is a constant known as the material's angle of internal friction, which is the slope of the envelope (Fossen and Gabrielsen, 2005). Rocks containing fluids experience pore pressures, and if the pore-pressure increases in the rock, which is normally under stable conditions, it can force the initiation of failure as the reduction of the effective stress pushes the Mohr circle to the left on the σ_n axis, without reducing the diameter (meaning that the differential stress stays the same). If the pore pressure

is high enough the Mohr circle may be forced to cross the envelope, and rupture (Fossen and Gabrielsen, 2005).

Faults and fractures lower the cohesion strength of the rock, so the amount of energy required to reactivating faults are lower compared to initiating new faults (Fossen and Gabrielsen, 2005). Therefore, the differential stress would be lower with reactivation, as the fault will follow the same fault planes where the stress will be accommodated by frictional sliding, and the fracture holds no cohesion.

1.2.5 Polygonal faults

In sedimentary basin around the world, uniformly developed fault arrays are seen on high resolution seismic, often confined to a specific succession or stratigraphic unit. These fault arrays are known as polygonal faults and tend to form in sediments dominantly consisting of clay-sized particles, i.e. they are layer bound. They are laterally extensive arrays of extensional faults, with a polygonal expression on the surface (Fig.1.6) (Cartwright, 2011). They were first documented in the North Sea basin in the lower Tertiary mud rocks (Cartwright, 1994). There is still an ongoing debate on the mechanisms behind the formation of polygonal faults, and several have been proposed, such as (1) synerisis, contraction and liquid expulsion (Cartwright and Lonergan, 1996; Dewhurst et al., 1999). (2) Thermal and chemical contraction due to diagenesis with opal-A to opal-CT reactions (Davies et al., 2009; Cartwright, 2011; Davies and Ireland, 2011), (3) density inversion (Henriet et al., 1989) and (4) low coefficients of residual friction (Goulty, 2008). For shallow plays, polygonal faults may serve as conduits for fluids as they represent areas of potential overpressure (Lonergan and Cartwright, 1999; Stuevold et al., 2003; Cartwright, 2007), they are therefore important in the study of shallow fluid accumulation. Polygonal faults are normal (extensional) dip-slip faults in their kinematics. The dip of the fault plane usually range from ~50-80°, but deeper tiers tend to show fault systems with lower angles, ~20-50° (Lonergan et al., 1998). On the contrary, to most extensional faults, polygonal faults are not directly related to tectonic activity. The genesis of polygonal faults is neither compressional nor extensional, but they may act as zones of weakness under later tectonic events where they can be reactivated as compressional or extensional faults, giving the impressions that the initially polygonal faults are of extensional or compressional character (Ostanin et al., 2012). Polygonal faults are found, particularly in extensional basins worldwide (Cartwright and Dewhurst, 1998).

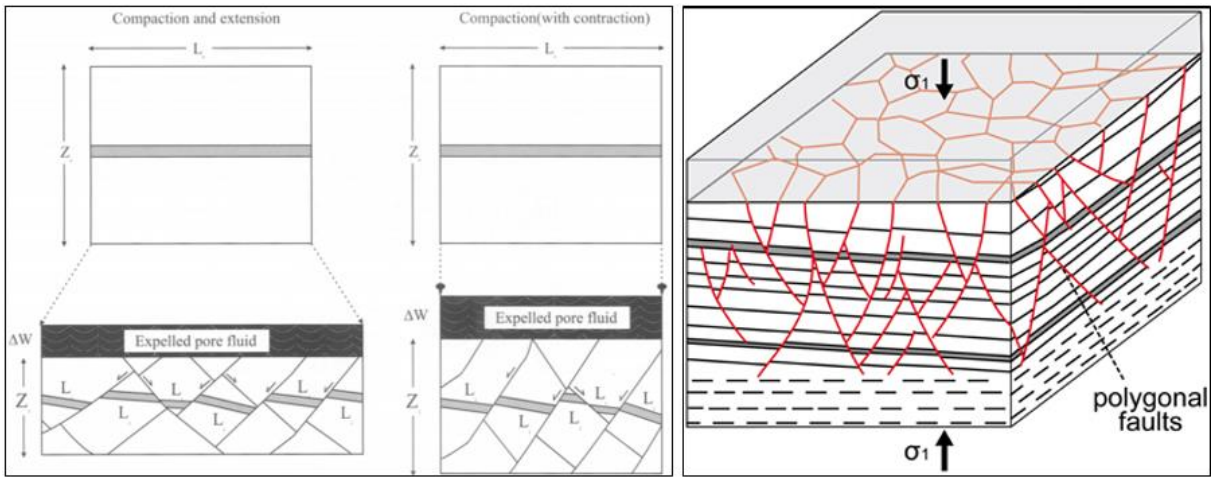

Figure 1.6 *Left figure after Cartwright et al. (2003) shows how polygonal faults may develop under different stress conditions. Figure to the right from Petracchini et al. (2015) describes in a schematic way the 3D seismic expression of polygonal faults in a sedimentary basin, and the direction of* σ_1.

1.3 Flow in porous media

Subsurface fluids occupy pores and fractures of the sediments and rocks. They may exist either in a gaseous phase or liquid phase, or in a solution of one in the other (Guzzetta and Cinquegrana, 1987). For supporting the subsurface fluid flow, the matrix (sediments or rocks) has to meet the conditions of permeability, which require connected pore spaces. Thus, the mass flow of fluids through a porous media depends on rock properties (Berndt, 2005). The behaviour and movement of fluids when flowing through a porous media is govern by Darcy's law (equation 1.3). The flow is pressure related and is driven by the pressure gradient from areas with high pressure to areas with lower pressure. The permeability is a function of the material type, and it therefor varies with stress and temperature. The fluid viscosity controls how the fluid responds to the change in pressure, and is different for different kinds of fluids. However, Darcy's equation is only valid if the pore spaces are filled with one fluid phase, and there are no chemical reactions between the grains and the fluid (Berndt, 2005).

$$Q = -\frac{kA(P_b - P_a)}{\mu L} \qquad (Equation\ 1.3)$$

Q = Total discharge (m^3/s) k = permeability (m^2) A = cross sectional area (m^2)
$P_b - P_a$ = pressure difference (Pa) μ = Viscosity of the medium (Pa*s)

Fluids in the subsurface are often a mixture of many compounds, and therefore respond differently to temperature and pressure. The flow of fluids is not only constrained by Darcy's law but also by the fluids ability to overcome the capillary entry pressure (equation 1.4).

$$Capillary\ pressure = \frac{2i\ cos\theta}{r} \qquad (Equation\ 1.4)$$

The origin of the pressure gradient in the subsurface is related to the compaction history of the sediments. In general, sediments become more compacted over time as new sediments accumulate on top of them, increasing the load of the overburden. If the grain configuration changes, the density of the medium increases, and the permeability and porosity will decrease correspondingly (Berndt, 2005). How the sediments respond to the compaction depends on the lithological type, and varies with increasing temperatures. Thus, diagenesis largely constrains sediment permeability. The pore pressure within the sediments will equal the hydrostatic pressure (equation 1.5) if the fluids are able to percolate as the porosity decreases. Under the influence if gravity, phases tend to separate, so the less dense phase overlies the denser phase (Guzzetta and Cinquegrana, 1987). The hydrostatic pressure (equation 1.3) is the pressure experienced by any fluids at rest in a continuous fluid-column. Should the pressure surpass the hydrostatic pressure, the fluids are said to be over-pressured. Overpressures are common in the subsurface where fluids have been trapped in the pore spaces of sediments during burial.

$$P = pgh + P_a \qquad (Equation\ 1.5)$$

P = pore pressure (Bar) p = density of the pore water (kg/m^3) g = gravitational constant ($9.81 m/s^2$) h = height of fluid column (m) P_a = atmospheric pressure, atm (1 Bar).

1.4 Methane in the subsurface

Burial of organic-rich sediments may provoke extensive methane generation and give rise to large accumulations. Methane gas is buoyant and therefore tends to migrate upwards (Judd and Hovland, 2007). The migration often results in seafloor seepage, but if specific geological conditions are right, large accumulations may form below the seabed. If the water depth is sufficient (300-500m), and requirements for low temperature are met, the formation of gas hydrates is favoured (Judd and Hovland, 2007). Under temperature and pressure conditions of

hydrate stability, they act as major sink for methane and other hydrocarbon gases. On the other hand, dissociation hydrates may be a source of extensive gas release when depressurization or warming occurs.

In marine sediments, methane is one of the most common gases and of great importance when it comes to fluid flow on the seabed. Methane from natural gas seeps has a potential to reach the atmosphere and contribute to a progressively rising pool of greenhouse gases. It also plays an important role supporting chemosynthetic biological communities. The origin of subsurface methane can be either biogenic or abiogenic. The migration and accumulation processes in the subsurface applies to any kind of gas, regardless of its origin. When the dissolved gas rises through a sediment section, the pressure conditions decrease, which may cause transformation of some amount of dissolved gas to a free gas. The subsurface depth of free gas release largely depends on dissolved gas concentrations and its solubility limits.

Even at 3-4 km below the seabed, the gas has a high buoyance, and the overpressures often found at these depths helps to drive the migration process. Even though natural seepage of methane occurs, most of the gas is trapped on its way to the surface, and this is the origin for shallow gas accumulation (Judd and Hovland, 2007). Accumulations often form at several levels beneath the seabed, suggesting that many of them are somewhat ephemeral and not permanent features (Judd and Hovland, 2007). Shallow gas accumulations often have a thermogenic origin, where they accumulate as a result of seepage from deeper-lying hydrocarbon reservoirs (Chand et al., 2009).

1.4.1 Acoustic response of gas in sediments

Gas trapped in the sediments affects the acoustic response, as it tends to scatter the sonic energy (equation 1.6). When the sonic energy hits the gas bubbles, the speed of the sound propagation changes drastically, and the sound attenuation increases (Hovland, 2007). At the same time, the tensile strength of the sediments is heavily reduced. The size of the gas bubbles affects the amount of attenuation, and is relative to the acoustic wavelength (Judd and Hovland, 2007).

$$\lambda = \frac{V_p}{f} \qquad (Equation\ 1.6)$$

Where λ = wavelength (m), f = frequency (Hz) and V_p = P-wave velocity (m/s)

The seismic reflection is a result of acoustic impedance (AI) (Equation 1.7), which is the product of density and the p-wave velocity as the energy hits any interface in the subsurface.

$$Aucustic\ Impedance\ (Z) = \rho * V_p \qquad (Equation\ 1.7)$$

Where Z = acoustic impedance, ρ = density (kg/m^2) and V_p = P-wave velocity (m/s)

1.4.2 Gas brightening

In high resolution seismic, minor accumulations of gas may appear as coherent reflections with a significantly higher amplitude (Fig. 1.7) over a longer interval. The gas causes a "negative" impedance contrast. It results in phase reversed reflections and large amplitudes, somewhat similar to the deeper equivalents known as bright spots (Judd and Hovland, 2007).

1.4.3 Acoustic turbidity and gas chimneys

Acoustic turbidity (sometimes referred to as seismic masking) is one of the most common evidence for presence of free gas in shallow marine sediments. The turbidity is a result of the attenuation and scattering of the energy as it hits the gas bubbles and this causes a chaotic reflection pattern. This may cause problems interpreting any original depositional feature and sometimes obscuring the reflections from deeper sediments (Judd and Hovland, 2007). In 2D and 3D- seismic data sets, vertical features with obscured reflections shows the presence of gas migration in the subsurface. The disturbed reflections may be a result of ongoing or previous gas migration.

1.4.4 Bright spot

Bright spots occur on seismic profiles where there is a strong acoustic impedance contrast (Fig. 1.7). The strong AI contrast often appears where un-lithified sediments overlie a much denser rock. The bright spot appears on the profiles as discontinuous reflections caused by high-amplitude negative phase reflections (Judd and Hovland, 2007).

1.4.5 Flat spots

In the subsurface, the interface between water and gas will give a strong AI contrast (Fig. 1.7). As this is interface most often horizontal, so will the coherent reflection at this interface be. Most often, it is a result of the contrast in AI between water-filled sediments and gas-filled

sediments (Hovland et al., 2002). It could also show the oil-gas contact, as the oil have similar P-wave velocity as water.

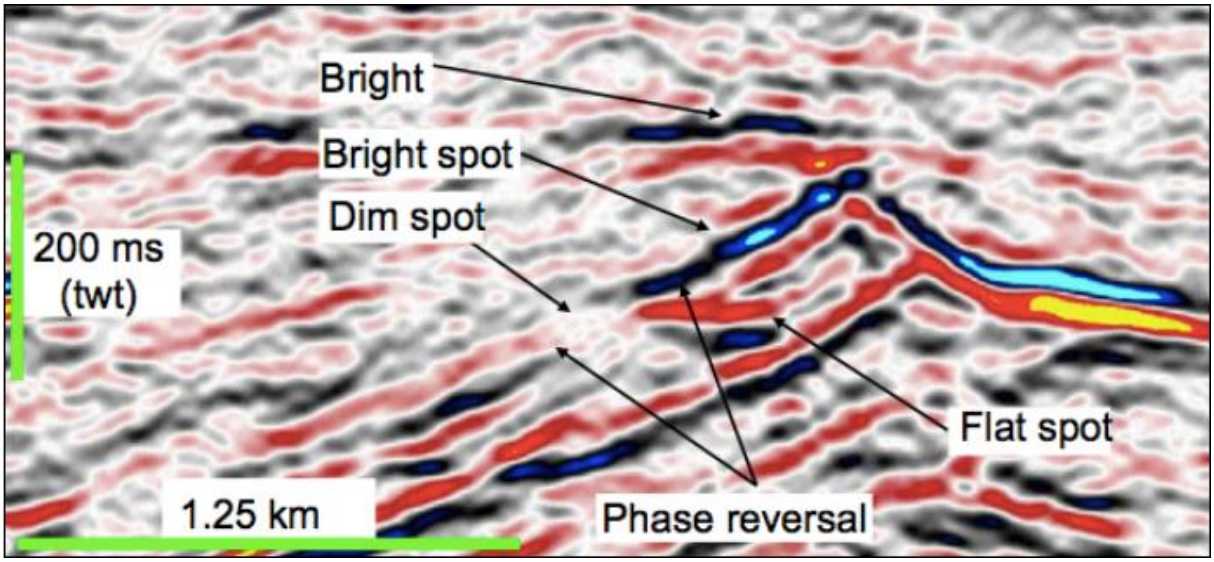

Figure 1.7 *Seismic expressions of fluid flow and fluid accumulations (Løseth et al. (2009)).*

1.4.6 Gas hydrates and shallow gas accumulations

Gas hydrates are ice-like structures containing methane or other hydrocarbon gases trapped in a cage-like framework of hydrogen bonded water molecules (Sloan, 1998; Sloan and Koh, 1998; Judd and Hovland, 2007). The formation of gas hydrates requires a combination of low temperature and high pressure. Intervals where these requirements are met are called the Gas Hydrate Stability Zone (GHSZ). The GHSZ is often found below the permafrost in the arctic regions or in deep water on the continental margins (Sloan, 1998). Moreover, composition of gas, salinity of pore-waters and availability of pore space largely controls nucleation of natural gas hydrates in marine sediments (Sloan, 1998; Liu and Flemings, 2006). Thus, temperature and pressure conditions are required; however, not sufficient to form actual gas hydrates. It implies that the GHSZ does not always bear hydrates. The most common compound in hydrates is methane, but compounds such as hydrogen sulphide and carbon dioxide as well as heavier hydrocarbons have also been recorded (Kvenvolden, 1998; Chand and Minshull, 2003).

The base of the GHSZ is sometimes visible on seismic as anomalous reflections mimicking the seabed. These reflectors are known as bottom simulation reflectors (BSRs) and is the most robust and commonly used indication of gas hydrates (Bünz et al., 2003). On seismic lines, the BSR's are recognized by their high amplitude, and reversed polarity from the seabed reflector. The BSR occurs as a response to the abrupt change in the AI on the interface between the

hydrate bearing sediments and the underlying sediments containing free gas (Sloan Jr and Koh, 2007; Judd and Hovland, 2007; Vadakkepuliyambatta et al., 2013). The GHSZ will normally not extend to the seafloor due to generally low concentrations of gas in subsurface sediments, which is below the solubility limits and not enough to form hydrates (Chand and Minshull, 2003).

Gas hydrates may block or substantially reduce flux of gas migrating from deeper subsurface towards the seafloor. Gas trapped beneath the GHSZ is often referred to as shallow gas accumulations (Judd and Hovland, 2007). Change in the stability parameters of the GHSZ (warming or depressurization), may trigger gas hydrate to dissociation. This leads to release of free gas, which migrates towards the surface. Active venting of methane, often leads to formation of circular to sub-circular depressions on the seafloor known as pockmarks.

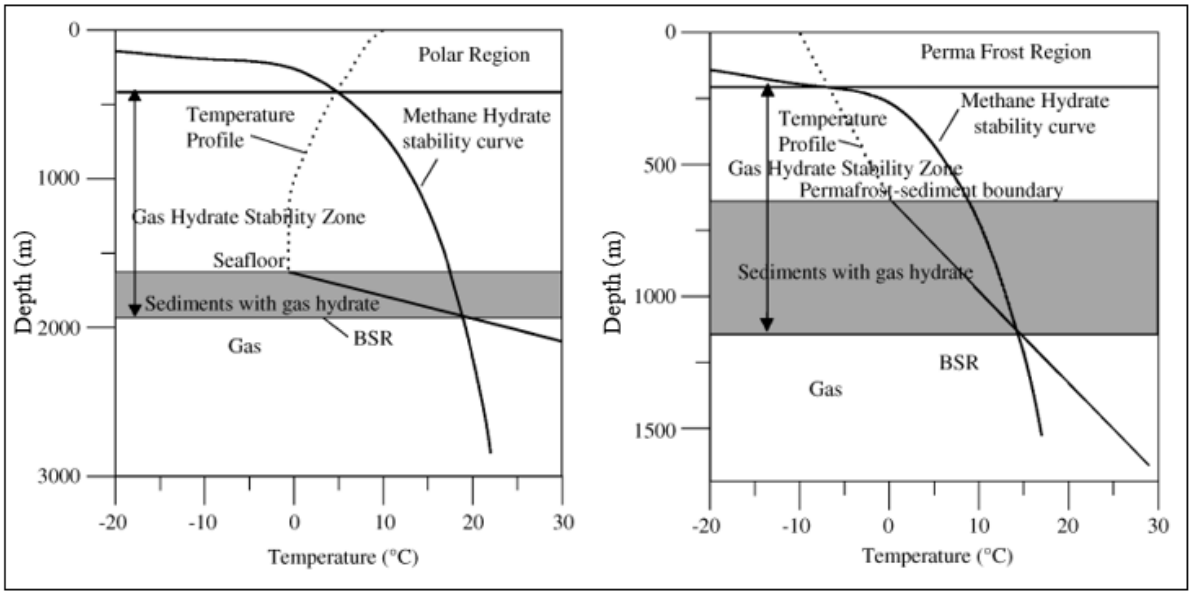

Figure 1.8 *phase diagrams showing the stability field of gas hydrate with different geothermal gradients. The methane hydrate stability curve is calculated from hydrostatic pressures. Diagram to the left shows polar conditions, where the geothermal gradient is 50°C km^{-1}. Diagram to the right shows a geothermal gradient of 40°C km^{-1} in a permafrost region. Figure is modified from Chand and Minshull (2003).*

1.4.7 Surface expressions of fluid flow release

On continental margins worldwide, circular to sub-circular and elongated depressions can be found either as single features or in clusters (Hovland, 1981) of up to over a hundred per square kilometre, covering large areas of the seabed (Fig. 1.7). These depressions are often inferred to be related to fluid flow, and are named pockmarks (King and MacLEAN, 1970). Pockmarks vary in size from a few metres in diameter to over 400 m, with depths ranging from 2 m and up

to over 15 m (Chand et al., 2009). They are often associated with a dynamic fluid flow system, however the nature of fluids involved may vary broadly. In areas bearing permafrost, pockmarks can form as a result of it's thawing that initiates fresh water expulsion (King, 1980). Alternatively, dissociating gas hydrates may release free gases that, when reaching the seafloor, form a pockmark (Mienert et al., 1998). In areas of rapid sedimentation, pockmarks may form due to discharge of water originated as a result of sediment compaction. Pockmarks are mostly related to fine-grained soft sediments (silty or clayey muds). Such a correlation is not accidental. The pockmark formation requires disturbance of sedimentary matrix by ascending fluids and removal of mobilized material by activity of bottom currents. Fine-grained material is more susceptible for disturbances and removal by currents, than coarser sediments, such as sand. Thus, for creating a pockmark in sandy sediments, a very highly energetic environment would be required, which rarely occurs at natural seep sites. Additionally it is often observed that smaller pockmarks tend to form in the older and bigger ones (Judd and Hovland, 2007; Løseth et al., 2009).

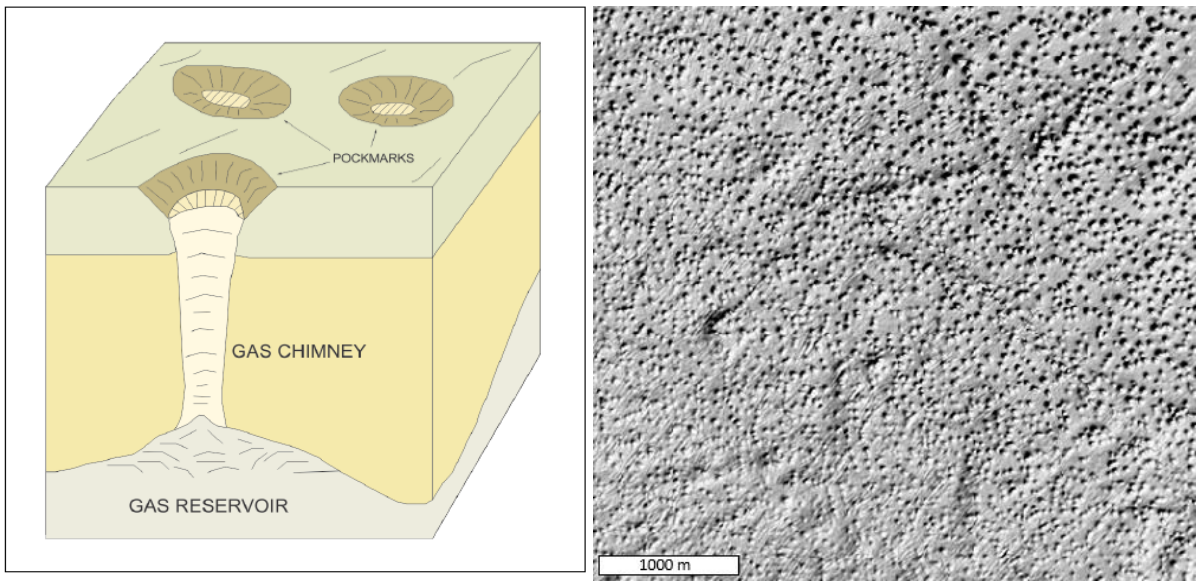

Figure 1.9 ***Left:*** *conceptual block diagram showing how pockmarks form and how they are often related to gas chimneys and deeper-seated gas reservoirs. Figure after Cathles et al. (2010).* ***Right:*** *shadow relief bathymetric map obtained from the Mareano database showing the surface expressions of pockmarks from the Goliat area in the SW Barents Sea*

2 Study area

Barents Sea is a shallow (average water depths is 230m), epicontinental sea occupying and area of 1,3 km^2 off shore Norway and Russia. It extends from the Norwegian Sea in the west to the Svalbard and the Novaya Zemlya, Franz Josef Land in the north.

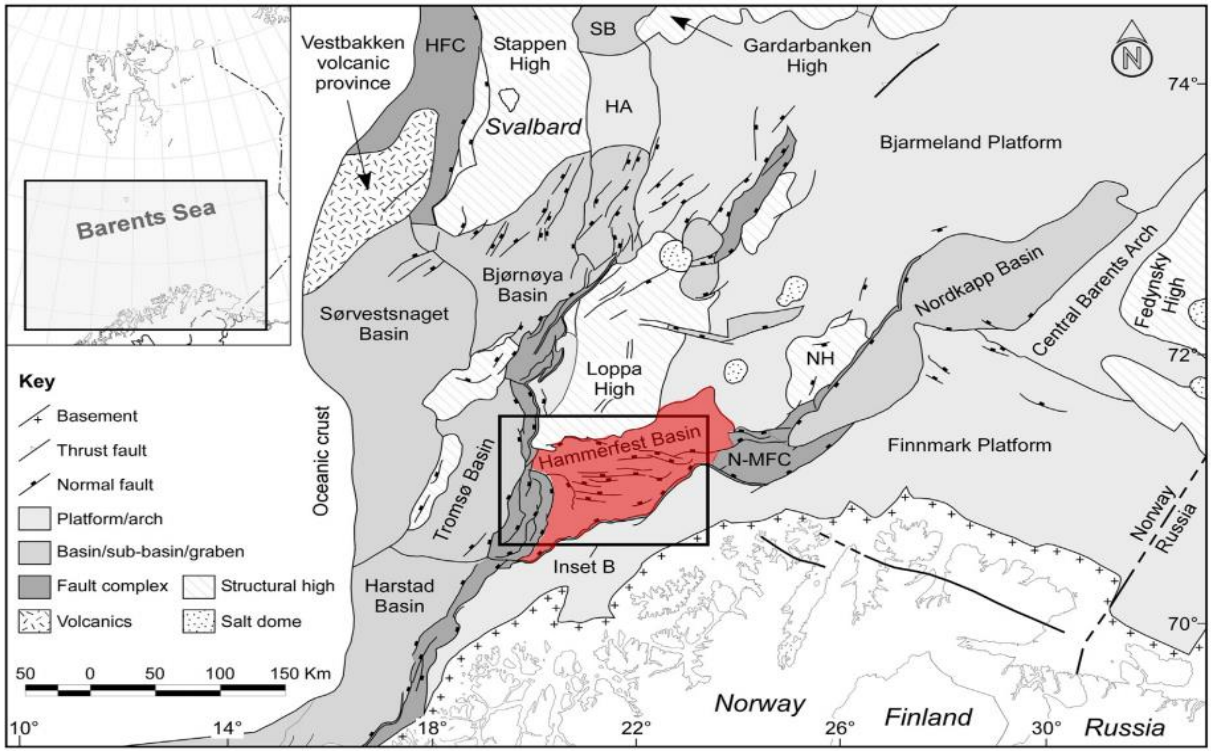

Figure 2.1 *overview of the structural elements in large parts of the Barents Sea and the location of the study area, coloured in red. The figure is modified after Murillo et al. (2016)*

Being one of the least explored areas offshore Norway, the focus towards possible new prospects in The Barents Sea had caught the attention of the petroleum industry. In the 1970's the first geophysical investigations were carried out, and the first well was drilled by the early 1980's after they discovered that the Barents Sea had a complex network of deep and shallow sedimentary basins, as well as sedimentary succession of interests (Doré, 1995).

The large-scale structures of the Barents Shelf can roughly be divided into two geological provinces; East and West. The eastern parts are influenced by a complex, and still debated tectonic history of the Novaya Zemlya and the Timan-Pechora basin, and by the Uralian Orogeny. The western parts have mostly been controlled by the post-Caledonian rifting phases, as well as later rifting episodes (Faleide et al., 1993).

2.1 Geological history of the Barents Sea

2.1.1 Paleozoic (541 – 254Ma)

The Barents Sea has undergone two major continental collisions, and subsequently sundered by continental separation. These events have laid the foundation for the structural framework of the present Barents Sea (Doré, 1995). Much of the Barents Sea history corresponds to that of the Scandinavian Caledonides (Smelror et al., 2009). The Caledonian orogeny, a response to the closing of the Iapetus Ocean culminated approximately 400 million years ago. It resulted in a consolidation of the Baltican and Laurantian plate into the Laurasia plate. Subsequently, the inherited structures from this orogeny affected the structural evolution of the SW Barents Sea. and the Caledonian influences is observed in the N-S structural grain of the western Barents Sea margin, and the SW-NE grains of the SW Barents Sea (Smelror et al., 2009). After the Caledonian Orogeny, the region underwent extensive erosion in Devonian and Carboniferous when the area was subject to exhumation, leading to accumulation of Old Red Sandstones in the western parts. The SW Barents Sea was gradually peneplaned (Doré, 1995; Smelror et al., 2009).

Major parts of the Barents Sea became subject to extensional tectonics during the late Paleozoic. The Late Devonian and Carboniferous regional extension is characterized by a westward migration, with the following formation of well-defined rift- and pull-apart basins in the south west, and with the development of strike slip faults in the north (Faleide et al., 1993). Many of the basins followed the inherited Caledonian structural features. As the rifting ceased in late Carboniferous, the area underwent regional subsidence in the western Barents Sea.

Due to the northward migration of the Pangea continent, the climatic conditions changed in Carboniferous. A more temperate climate led to the formation of enormous carbonate platforms, where thick successions of evaporates were locally deposited in graben structures that had developed in the southwest (e.g. Tromsø basin and Nordkapp Basin) (Faleide et al., 2008; Worsley, 2008; Smelror et al., 2009).

Early Permian deposits are characterized by high frequency and high-amplitude eustatic sea level changes. These dramatic changes in the sea level were a response to the glaciations on the southern hemisphere. From the late Permian, a change in the sedimentary system occurred. By the end of the Permian, a marine link remained open to the west until the opening of the early Atlantic rift system (Faleide et al., 1984; Worsley, 2008; Smelror et al., 2009). During the

crustal breakup, the SW Barents Sea was the locus of two structural mega-lineaments: the North Atlantic rift zone between the present Charlie Gibbs and Senja Fracture Zones, and a shear zone, the De Geer Line (Harland, 1969) between Svalbard and Greenland (Faleide et al., 1993).

2.1.2 Mesozoic (252 – 72Ma)

In early Triassic, the Uralian highlands along with the uplifted Novaya Zemlya Archipelago and Fennoscandian shield became a major sediment source for basins and platform areas. The Uralian orogeny eventually led to the closure of the marine connection from the SE to the Barents Sea. The western parts of the Barents Shelf experienced a tectonically inactive period, with passive regional subsidence (Worsley, 2008; Smelror et al., 2009). Tectonic activity exclusively occurred along the western margin where the Loppa High was uplifted and eroded (Smelror et al., 2009). A basement-involved regional extension led to salt-diapirism in the Nordkapp Basin in early Triassic (Nilsen et al., 1995).

By the middle Triassic, the Barents Sea comprised a central marine shelf bordered by land areas. Open marine connections may have existed in the SW part. At the same time, a regional regression reaches its maximum, leaving restricted basin where mudstones with a total organic content (TOC) up to 9% were deposited in strictly anoxic conditions (Smelror et al., 2009).

Large areas of the Barents shelf were subject to uplift and erosion in late Triassic – early Jurassic. The new supply of sediment led to a westward progradation of the coast, and the development of large tidal inlets, estuaries and lagoons in the western areas of the Barents shelf (Smelror et al., 2009). Much of the Barents Sea was tectonically inactive in the Jurassic, but in the Middle – Late Jurassic, the Barents Sea was subject to regional extension and adjustments along old lineaments (Faleide et al., 1993). The Late Jurassic transgression reaches its maximum, causing much of the Barents region to transfer to an open marine system. The Hammerfest basin and Bjørnøya basin experienced a period of rifting in Middle – Late Jurassic, where the rifting followed the pre-existing tectonic grain (Faleide et al., 1984; Faleide et al., 1993).

At least three different tectonic phases can be recognized from Early Cretaceous. Two phases, Berriasian/Valingian and Hauterivian/Barremian are related to the propagation of the Atlantic rifting, both affected the Hammerfest Basin. However, Tromsø and Bjørnøya basins experienced even more severe. The final rifting event in Early Cretaceous led to a rapid

subsidence and sedimentary infill of the Bjørnøya, Harstad and Tromsø basins. The extension, oriented in a west and west-northwest direction, induced sinsistral transtensional strike-slip movements along the Bjørnøyrenna Fault Complex (Faleide et al., 1993). By Late Cretaceous the basins in southwestern Barents Sea continued to subside. The subsidence is partly related to halokinesis in the Tromsø and southern Sørvestnag Basin (Faleide et al., 1993; Knutsen and Larsen, 1997). The continued breakup of the North Atlantic commenced. Continental breakup in Late Cretaceous led to the build-up of a dextral stress-field along the Senja fracture zone and the Hornsund Fracture Zone lineaments. This mega-fracture acts as a relay zone for the spreading activated in Paleocene (Smelror et al., 2009). The rifting in Late Cretaceous is linked by the De Geer Zone megashear system to the Arctic Eurasia Basin, and along this zone, the Western Barents Sea-Svalbard margin developed (Faleide et al., 2008).

2.1.3 Cenozoic (66Ma – present)

At the transition of Paleocene – Eocene seafloor spreading began south of the Greenland – Senja Fracture Zone in the Norwegian – Greenland Sea. The spreading axis propagated northward to the Hornsund Fault Zone. As a result of the early seafloor spreading, the Western Barents Sea margin developed as a shear margin within the De Geer Zone (Faleide et al., 1991; Faleide et al., 1993). Two individual sheared segments, the Hornsund Fault Zone and the Senja Fault Zone, separated this margin by a central rift segment (Faleide et al., 2008). The Senja Fracture Zone consists of several rift basins, which forms a series of pull-apart basins east of the continent-ocean transition. The fault zone developed as a shear zone in Eocene, but changes in the relative plate motion in Oligocene transformed the shear zone into a series of NNW-trending normal faults (Myhre and Eldholm, 1988). The Hornsund Fracture Zone developed as a response to Greenland sliding past Svalbard in Eocene (Myhre and Eldholm, 1988; Faleide et al., 1991; Faleide et al., 2008). Ongoing subsidence since late Mesozoic led to continuous infilling of the Harstad basin, Tromsø basin, Sørvestnag basin and Vestbakken Volcanic Province with sediments eroded from the uplifted areas (Smelror et al., 2009). The Eocene dextral shear margin propagated eastward and the formation of pull-apart basins was a response to the releasing bend (Faleide et al., 2008). The seafloor spreading between the Labrador Sea and Baffin Bay seized in early Oligocene. A change of the relative plate movement direction in the Norwegian – Greenland Sea to a North – West initiates seafloor spreading in the northern Greenland Sea (Eldholm et al., 1987; Myhre and Eldholm, 1988).

In Pliocene, the climate changed, leading to large ice sheets covering much of the Northern Hemisphere. The climatic fluctuations give rise to several alternating phases of glaciations and deglaciations. The uplifted Barents Sea shelf was subject to numerous extensive glacial erosion episodes. Repeated periods of erosion led to regional hiatus in the stratigraphic records. This hiatus is known as the Upper Regional Unconformity (URU) and is present over most of the Barents shelf. Svalbard is thought to have experienced the most extensive erosion, with an estimated removal of 2 – 3 km of overlying beds, while areas further south (Hammerfest basin and Loppa high) most likely experienced less impact, (1 – 1,5 km of eroded material) (Vorren et al., 1991; Smelror et al., 2009). The enormous amounts of sediments were transported by glaciers towards the western margin. It led to sediment accumulations of up to 4km in Bjørnøya and Storfjorden fan (Faleide et al., 2008; Smelror et al., 2009).

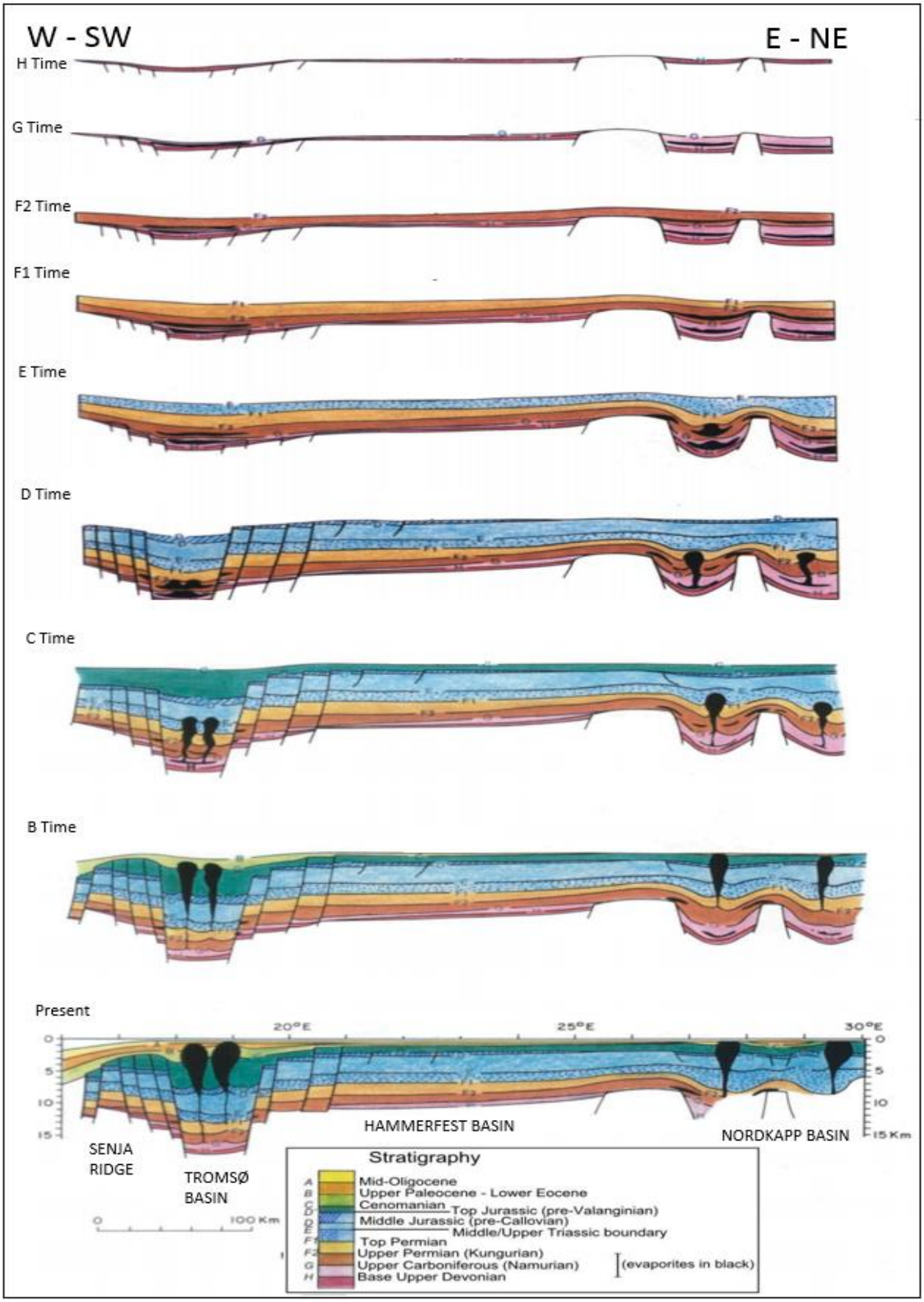

Figure 2.2 *Structural evolution of the southwestern Barents Sea, from Devonian to present. Figure is modified after Faleide et al. (1984).*

2.2 The Hammerfest Basin

The Hammerfest basin is a relatively shallow basin, which boarders the Finnmark platform in the south, and Loppa High and Bjarmeland Platform to the north. The Ringvassøy-Loppa Fault Complex separates it from the Tromsø basin in the west and to the east it is constrained by the Nysleppen-Måsøy fault complexes. The basin is fault controlled, and stretches in an east-west direction. It was likely established in late Carboniferous (Gabrielsen et al., 1990). Although, the main rift events with following subsidence occurred during the Triassic and early Cretaceous (Faleide et al., 1984; Gudlaugsson et al., 1998). The basin development culminated in mid-Cretaceous (Faleide et al., 1993). Geophysical surveys have found no evidence of Late Paleozoic evaporate deposits, even though they are present in the neighbouring Tromsø and Nordkapp basins. A central dome located at basin axis characterizes the internal structure of the basin, and there is a complex pattern of dominating W and WNW trending faults. The internal fault system consists of ENE-WSW and WSW-ENE trending faults. These faults are deep and high angled along the margin. In the Permian sequence detached, listric normal faults appear (NPD Bulletin). The basin experiences extension and influence from the Trollfjord-Komagelv fault trend, and it is thus possible to subdivide the basin into two separate sub-basins. One in the east and one in the west (Gabrielsen and Færseth, 1989). The western sub-basin dips gently towards the Tromsø basin, and in the eastern sub-basin it flexures towards the Bjarmeland Platform. The eastern sub-basin is less affected by faulting, and is thus considered a sag-basin. Many wells have been drilled in the basin, but only two of them have penetrated the upper Paleozoic succession.

The Hammerfest basin has been affected by the two tectonic phases; Berriasian/Valanginian and Hauterivian/Barremian, however this is not apparent on the seismic data (Faleide et al., 1993). Active rifting ended in the Hammerfest Basin during Barremian time based on the termination of doming in the basin (Faleide et al., 1993).

2.3 Stratigraphy and paleoenvironment of the southwestern Barents Sea

2.3.1 Paleozoic

From Late Devonian the SW Barents shelf were situated at the central parts of the northern Pangean margin, and was moving north from the equatorial latitudes. Coal bearing deposits with plant fossils show that the climate was humid and the depositional environment non-marine. The Billefjorden group was deposited as a rift-infill sequence consisting of different types of clastics. Marine-related deposits from this time occur at the Finnmark Platform, indicating a seaway through the Nordkapp Basin (Worsley, 2008). From mid-Carboniferous to mid-Permian, the humid climate changed to more arid and warm conditions. Sabkha evaporates deposited at low stand and shallow marine carbonates with local silicastic admixtures dominate at the platform areas in the Gipsdalen group. (Worsley, 2008; Duran et al., 2013). Due to Gondwanan glaciation and deglaciation significant and frequent sea level oscillations took place. Episodic exposure of the shelf led to widespread dolomitization and karstification (Worsley, 2008). A major flooding event is consistent with the Bjarmeland Group, with a following change to more temperate conditions marks the end of the high-frequency sea-level fluctuations seen in the Gipsdalen group. Termination of the Gondwanan ice cap is marked by this transgression.

By the end of Permian, a colder climate led to deposition of cold- and deep-water shales bearing inclusions of sandstone and limestone associated with local highs and platform margins (Worsley, 2008).

2.3.2 Mesozoic

Major hiatus marks the transition from Permian to Triassic. However, it's nature is yet to be unravelled (Worsley, 2008). The Early – Middle Triassic was dominated by the deposition of non-siliceous, fine clastics (Sassendalen Group), and is often referred to as the "Early Triassic Silica Gap). At the same time, restricted basins favoured the deposition of organic rich shales of the Kobbe and Snadd subgroups, both having a high potential to yield hydrocarbons (Worsley, 2008; Smelror et al., 2009). By early Triassic, the South Western Barents Sea had become isolated from the Central European. The closing of the seaway was a response to the uplift the mid-Norwegian and Greenland shelves (Doré, 1991). A large north-westerly propagating coastline covers most of the South Western shelf, with sand provenance from the

Baltic shield with increasing input from the Urals (Worsley, 2008). Over most of the Hammerfest Bain and Bjarmeland Platform, a NNE-trending clinoform system can be traced, and it is thought that this area might have been situated close to the paleocoast, as a possible sandy deltaic and shoreface environment.

In early Norian, a regional transgression, also known as the "Rhaetian transgression", flooded much of the area, which provoked a marine connections between the Tethyan and Boreal oceans. These connections followed the Proto-Atlantic seaway. At the same time, much of the subsidence in the Barents shelf ceased or decreased drastically, along with the sedimentation rates. The establishment of new shallow marine and coastal marine environments in Middle to Lower Jurassic, followed by deposition of well-sorted and mature sandstones provided excellent reservoir units like the Tubåen, Nordmela and Stø formations of the Realgrunnen Subgroup (Kapp Toscana) (Worsley, 2008).

A regional transgression in Bathonian led to deposition of anoxic black shales (Hekkingen Formation) and marine calcareous mudstones (Fuglen Formation) in Late Jurassic. Black shales of the Upper Jurassic show a TOC up to 20% and are widely considered to have an excellent hydrocarbon potential (Faleide et al., 1993; Worsley, 2008).

The transition from Jurassic to Cretaceous is marked by a change in the depositional environment. The deposition of anoxic shales ceased as the bottom circulation eventually enhanced with the development of an open marine environment. The continuous sedimentation in the Hammerfest basin led to the deposition of thick units of claystone with strings of limestone and dolomite (Knurr and Kolje Formations), unlike the highs and platform areas, which were starved and more carbonate dominated (Worsley, 2008; Smelror et al., 2009). By Albian times, the uplifted northern parts of the shelf worked as provenance for sediments being redeposited into the rapidly subsiding marginal basins in the west. (Smelror et al., 2009). The Kolmule Formation was deposited as a result of a transgression at the Aptian-Albian times. The formation consists of marine shales and marine organic rich shales, but it is not considered as a significant source rock (Smelror et al., 2009). The top of Kolume is marked by an unconformity, as a result of reactivation of faults and uplift in the Upper Cretaceous (Worsley, 2008; Ostanin et al., 2012; Duran et al., 2013).

In upper Cretaceous, the Northern Platform of the Labrador Sea coincided with the opening of the Northern Atlantic. By Campanian time, the subsidence of the Western basins led to development of a deep marine environment with shallow shelf areas. To two formations the Nygrunnen group were deposited: Kveite and Kviting. The Kveite Formation, traced throughout Ringvassøya-Loppa Fault Complex and the Tromsø Basin is dominated by marine claystones with minor sand inputs. The Kviting formation consists mostly of limestone and is restricted to the eastern and central parts of the Hammerfest Basin (Worsley, 2008; Ostanin et al., 2012).

2.3.3 Cenozoic

During Paleogene, the Barents Shelf was subject to transtention, transpression and opening of the Norwegian-Greenland Sea. There was continuing tectonic activity along the western margin. The Torsk formation within the Sotbakken group was deposited restrictively in the western basins and the outer shelf margins, and is characterized by its high content of claystone, with minor inputs of tuff at its base (Faleide et al., 1993; Ostanin et al., 2012).

The Pliocene – Pleistocene marks the onset of several glaciations in the northern hemisphere. The late Neogene – Quaternary Nordland Group consists of a mix between sandstones and claystones in a rather chaotic manner, and lies unconformable on top of the Torsk formation. Fiedler and Faleide (1996) divides the late Cenozoic succession into three mega sequences (GI-GIII) based on seismic interpretation, with seven regional seismic reflectors recognized (R7-R1). They interpreted the deepest reflector, R7 to mark the onset of the glaciation. The mega sequences all show a chaotic seismic reflectivity pattern, however the deepest sequence, GI, demonstrates dipping reflections and a higher continuity of the seismic reflectors. This is thus likely to correspond to a glaciomarine environment with sandur- and deltaic conditions prevailing in front of the ice cap. The GII and GIII are less interpretable and is more likely to represent the mass movement of deposits either in front of or under the glaciers (Andreassen et al., 2004; Andreassen et al., 2007b). The mass movement by the ice cap led to the expansion of the Barents Sea continental margin, by up to 30 – 40 km in the western margin (Andreassen et al., 2007b).

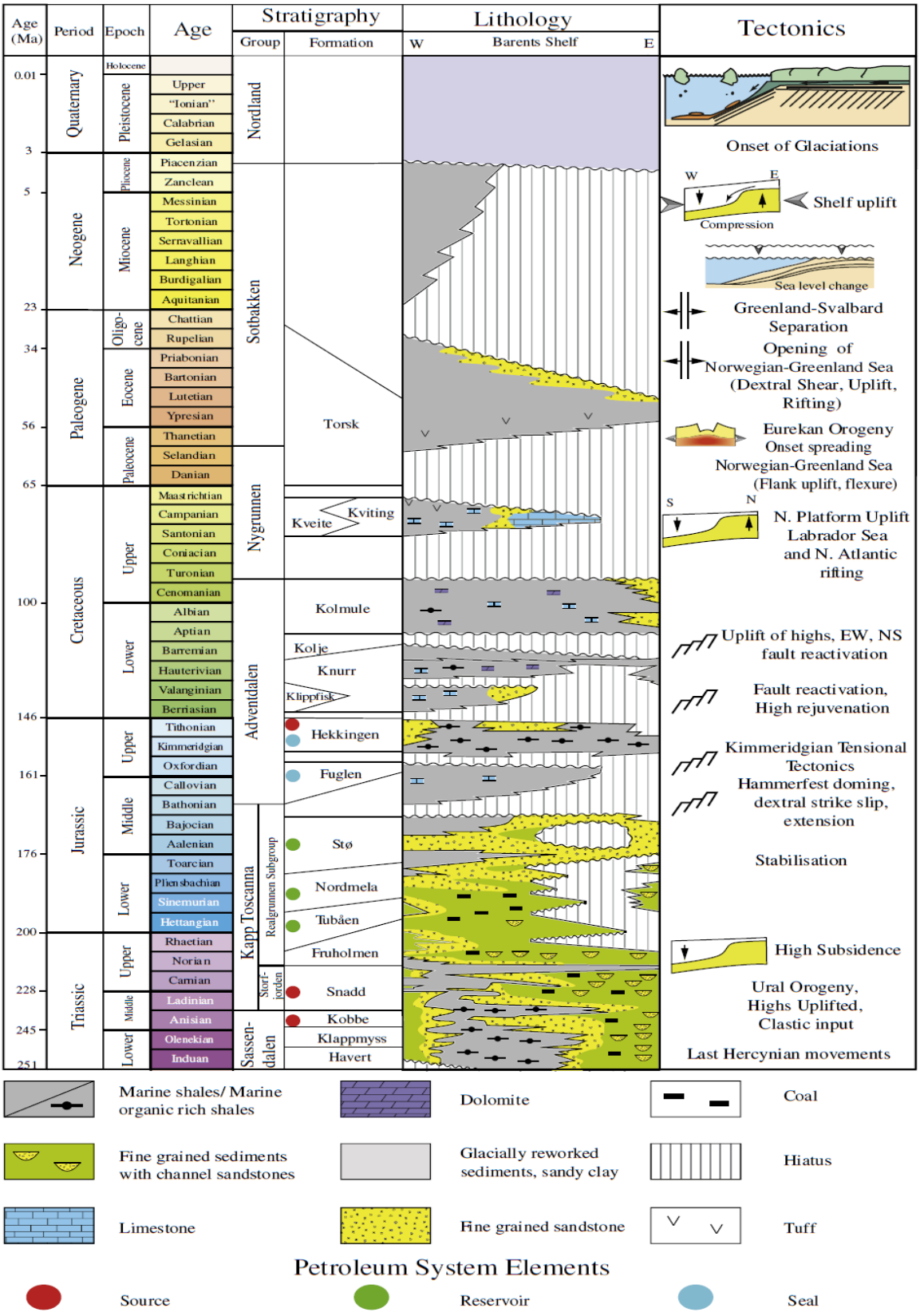

Figure 2.3 *Litostratigraphic chart showing both the major tectonics event and the following depositional environment. The different source, reservoir and cap rocks in the Hammerfest basin is indicated in their respective formation. Figure is modified after Ostanin et al. (2012).*

2.4 Source Rock

A source rock is a rock, rich in organic matter capable of generating and expelling hydrocarbons. In general, source rocks have total organic carbon content of more than 0.5%. In some cases, high quality source rocks may have a TOC as high as 10%. Depositional environment of the sediments can largely determine whether a source rock is oil or gas prone. Sediments deposited in marine or lacustrine environments tends to be oil-prone while source rocks deposited in a terrestrial settings, are more gas-prone (North, 1985).

Early geological surveys on the Spitsbergen Archipelago found active oil seeps in the exposed sedimentary layers. Since Spitsbergen represents an uplifted part of the Barents Sea, exploration companies started considering its submerged counterpart in hope of finding hydrocarbon accumulations equivalent those of the North Sea. Geophysical surveys found the Tromsø Basin and Hammerfest Basin to be the most promising areas for possible prospect (Doré, 1995). The most prominent source rocks in the Southwestern Barents Sea consist of organic rich shales of Upper Jurassic age (Doré, 1995). The formation is known as the Hekkingen Formation and is present in large areas of the southwestern Barents Sea (Ohm et al., 2008). Oil and gas generates at different temperatures, where the former is generated at temperatures from 60 – 120°C the latter is "cracked" to gas at 100 - 200°C depending on the composition of buried organic matter (Whiticar, 1994). It is therefore important to constrain a burial history of a sedimentary basin in order to find areas with possible hydrocarbon generation (Doré, 1995; Ohm et al., 2008; Selley and Sonnenberg, 2014).

Several source rocks have been proven in the Barents Sea at different stratigraphic levels. They range in age from Silurian to Cretaceous (Leith et al., 1992; Linjordet and Olsen, 1992; Doré, 1995; Ohm et al., 2008). Exploration drilling in the 1980's suggested that the Barents Sea was only gas-prone. This proved to be wrong when the large Goliat (Fig 3.8) and Nucula oil discoveries were made in 2000 and 2007 respectively (Ohm et al., 2008). Due to the complex tectonic history of the Barents Sea, maturity levels of the source rock significantly. Studies have shown that the maturity/depth trends deviate from other regions (Ohm et al., 2008; Henriksen et al., 2011). Repeated events of uplift and erosion is regarded as the reason behind this deviating trend (Doré and Jensen, 1996; Faleide et al., 1996; Cavanagh et al., 2006; Ohm et al., 2008). The uplifted parts of the Barents Sea may have cooled down enough for the generation

to come to a halt, while the deeper buried or areas who have experience no or very little uplift, the source rocks may be overmature and only expel gas.

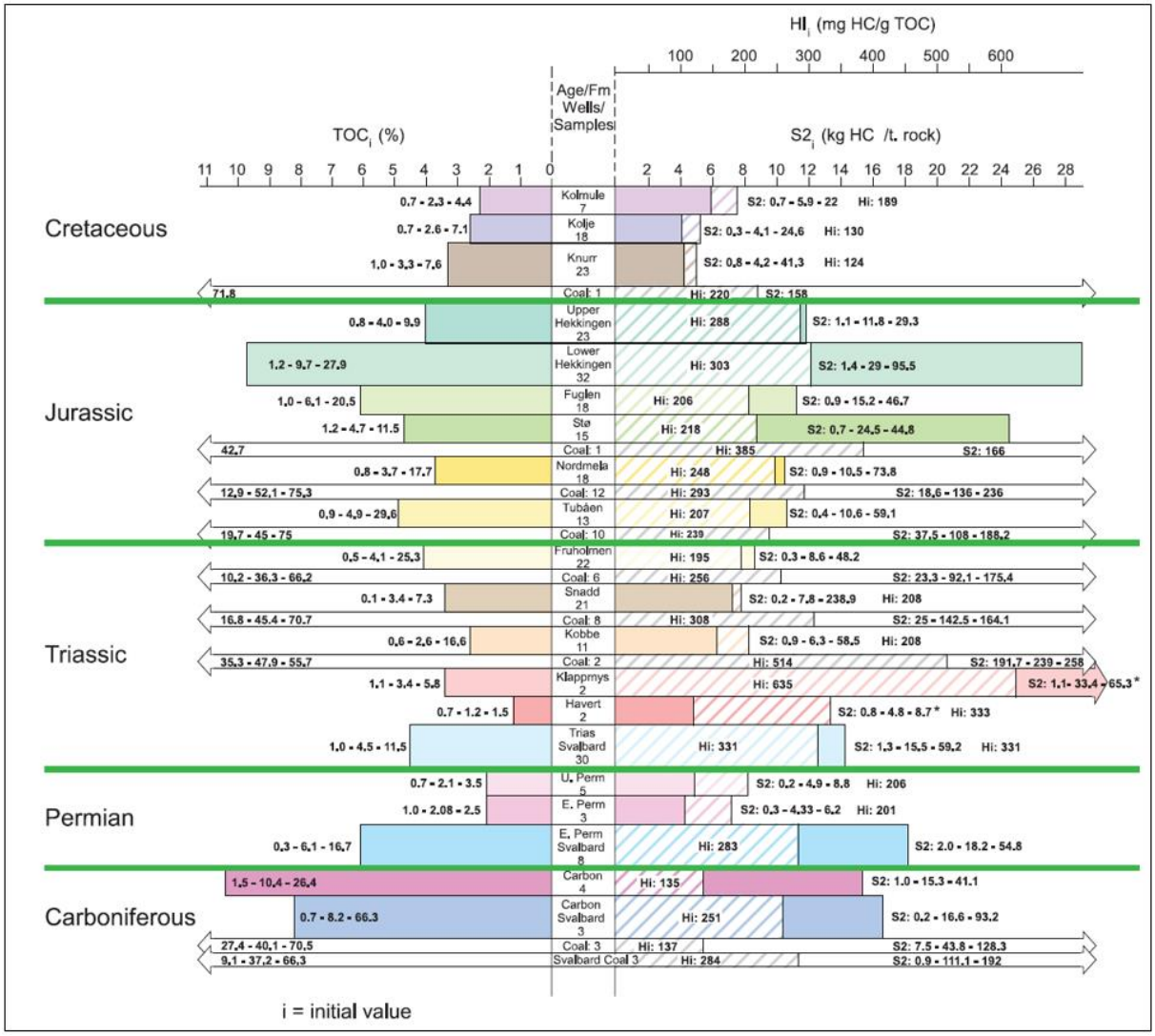

Figure 2.4 *Overview of the source rock characteristics and their original TOC. The source rocks are listed from Carboniferous to Cretaceous, and also includes the S2 (amount of HC generated) and the hydrogen index (HI). The most prolific source rock are found in the Hekkingen Formation, where 32 wells have provided data. The Hekkingen Formation is the most widespread source rock in the Barents sea, that is expelling hydrocarbons. Little information is obtained on the pre-Triassic intervals as few wells have penetrated this stratigraphy. Figure from Ohm et al. (2008).*

There are intervals from Middle and Lower Jurassic with potential of expelling oil along with the underlying Triassic shales (Fig. 2.3), which is also present in large areas of the southwestern Barents (Ohm et al., 2008). As the Triassic shales are buried deeper than the Jurassic shales, they mature earlier, and are found to be in the gas window where the Hekkingen Formation is oil-prone, and overmature in areas where the Hekkingen Formation is gas-prone (Ohm et al., 2008). It seems that the Triassic source rocks find themselves in the oil-window in the

Hammerfest Basin, while towards the Tromsø Basin they progressively increase in maturation level until they are overmature (Ohm et al., 2008). Because there are few wells drilled down into the pre-Triassic strata, little information is available on these source rock intervals.

3 Data & methods

This study is based on a 3D seismic dataset called EN0702 provided by Eni Norge from the PL229 area on the southern margin of the Hammerfest Basin in the Southwestern Barents Sea. (Fig. 3.1). Available offset wells is used to correlate some of the seismic units and to determine the upper and lower boundary of these units.

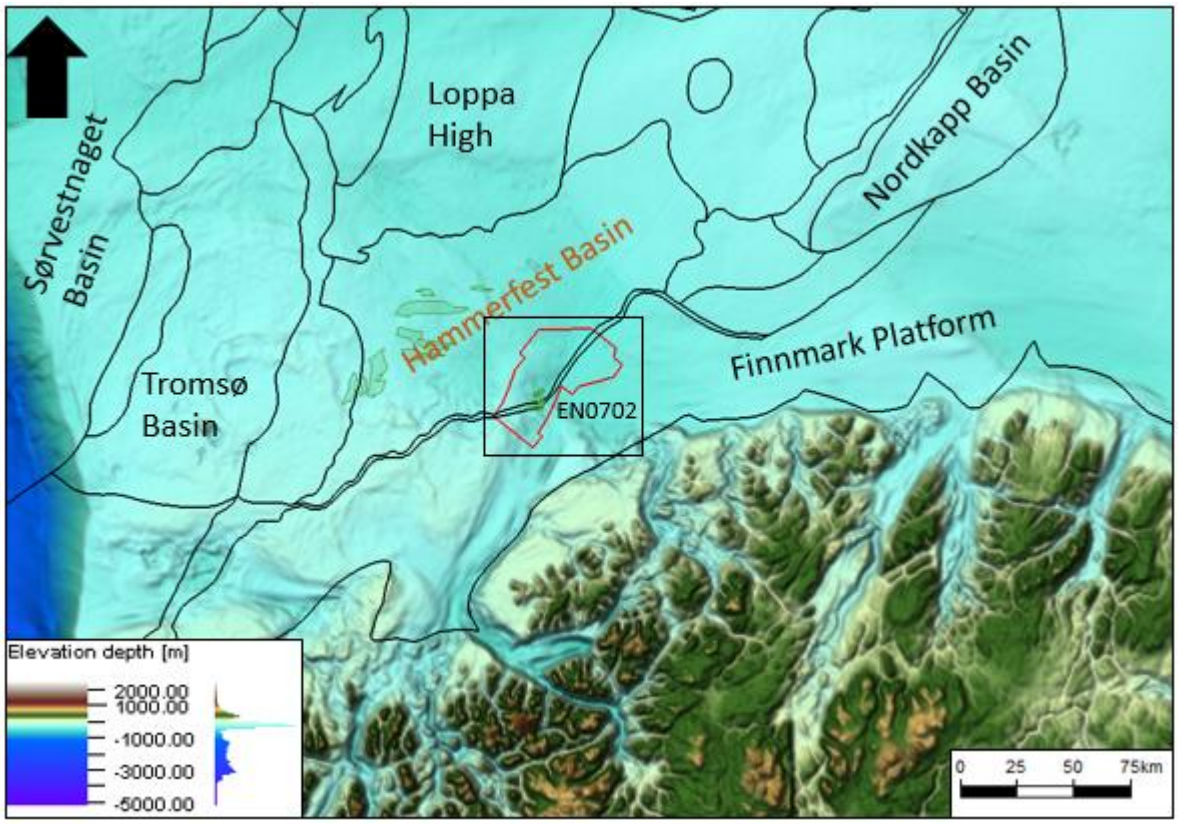

Figure 3.1 *Overview of the geography and structural elements of the study area. Survey area is outlined by red polygon marked EN0702*

3.1 Dataset

The 3D seismic survey EN0702, acquired by WesternGeco in 2007, covers approximately 650 km2. They used two sources and eight streamers, when collecting the data. Each of the eight streamers had active lengths of 4000m, recording four and a half seconds of data. The source would discharge a shot every 12.5m, which would yield an individual shot every 25m.

The dataset is processed to zero-phase, meaning that the reflectors have a normal European polarity (SEG reverse). This implies that a peak, having a positive reflection coefficient will

correspond to a decrease in the AI (Sheriff, 2012). The survey is acquired in NW – SE direction (inline-direction). The objectives of the survey, were to enhance the vertical and spatial resolution, with a goal of maintaining the relative amplitude for later AVO analysis.

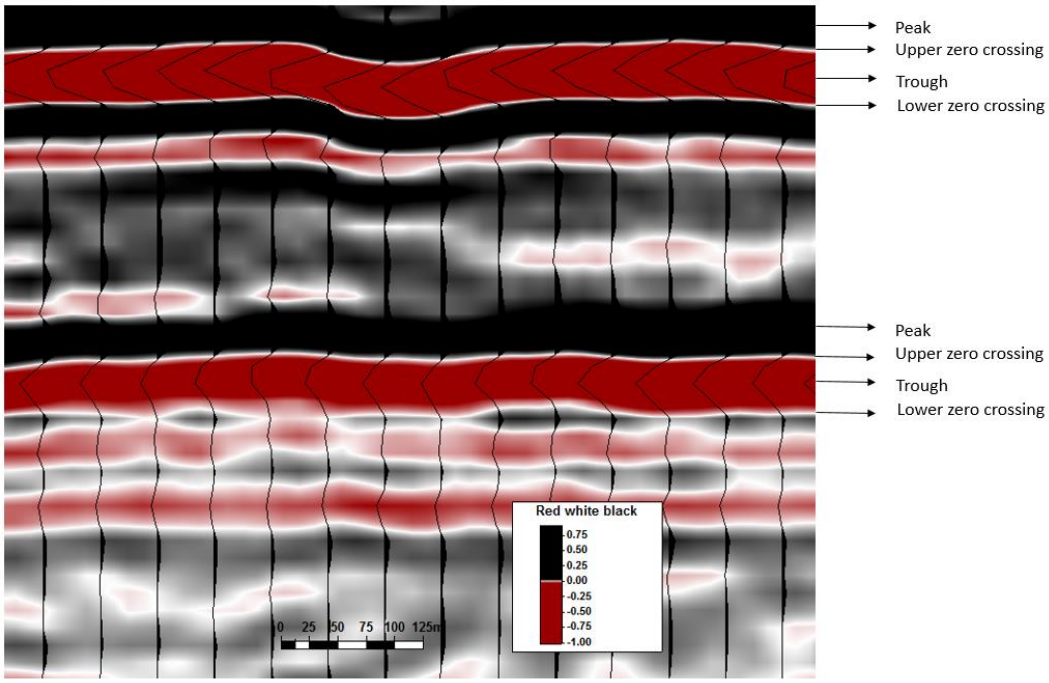

Figure 3.2: *A seismic section from the EN0702 survey, showing that the wavelet is processed to a zero-phase reverse signal (SEG standard polarity).*

3.1.1 Artefacts in the dataset

Typical, coherent noise in finished seismically processed data sets are artefacts parallel to the survey direction. These "footprints" also exists in EN0702 (Fig. 3.3), and it is important to be cautious not to interpret these as actual features. The artefacts correlate with the surveys acquisition geometry (same direction as the survey direction, or inlines) (Bulat, 2005).

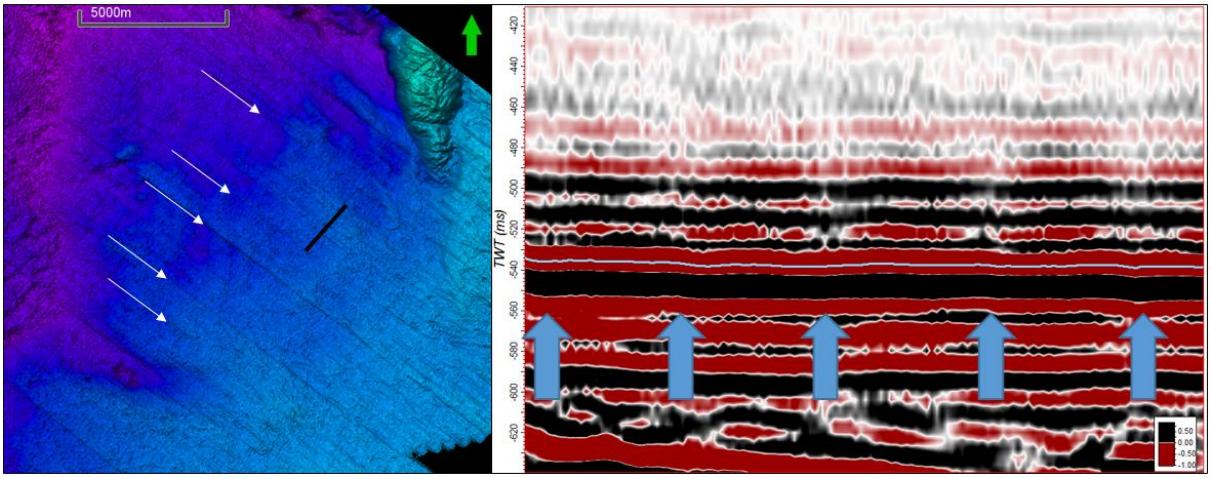

Figure 3.3 *Survey footprints, a result of coherent noise (black arrows in left picture), show up as artefacts on the interpreted horizons in the EN0702 dataset. The artefacts are particularly visible in sections perpendicular to the SW – NE inlines, and could be mistaken for representing actual features. Location of seismic section is marked as black line in picture to the left.*

3.1.2 Reflection and refraction seismic.

Seismic waves travel through the earth as body and surface waves. In seismic surveys, it is the elastic body waves transmitted through water and medium that is of interest. These waves travel as pressure- and shear waves, where only the former have the ability to travel through water, as water has no shear strength.

Acoustic Energy therefore travels through the water as elastic P-waves (pressure waves). When the energy hits a surface or an interface, e.g. the seafloor or a stratigraphic horizon in the subsurface, it will be scattered and transmitted. When an incident ray hits a horizontal plane (z = 0) at normal incidence, the incident energy will immediately be partitioned into refracted and reflected waves. Snell's law describes the geometry of the refracted and reflected wave, as they travel through different media, which transmits the waves at different velocities (Sheriff, 1992).

$$\frac{Sin\theta_1}{sin\theta_2} = \frac{v_1}{v_2} = \frac{n_1}{n_2} \qquad (Equation\ 1.8)$$

Snell's formula (Equation 1.8) shows that when a wave passing from medium with density 1 to medium with density 2, both the sines of the angles of incidence and refraction (θ_1 and θ_2) will have a constant number. The constant number will in addition be equal to the ratio of the velocities in the mediums (v_1 and v_2), as well as the inverse ratio of the exponent of refraction of the two mediums (n_1 and n_2). The incident P-wave will generate reflected P- and S-waves.

Additionally, when hitting an interface or a lithological boundary, the incident P-wave will generate a refracted P- and S-wave (Fig. 3.4)

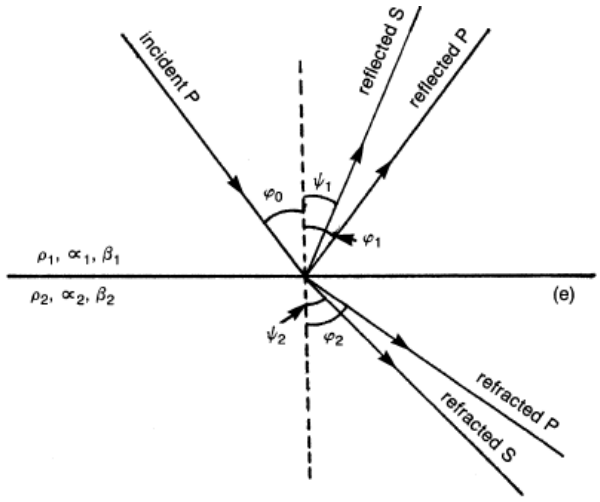

Figure 3.4 *The incident P-wave generates reflected P- and S-waves along with refracted P- and S-waves. The refracted and reflected waves follow Snell's law.*

3.1.3 Reflection coefficient:

The reflection coefficient is a way of showing how much energy that is reflected back from an interface as the acoustic wave propagates through different media. When the energy hits a surface or an interface, it will be reflected if the medium has a higher or lower acoustic impedance (Equation 1.9). The change in acoustic impedance is caused by differences in lithology and/or the presence of fluids. The reflection coefficient may range from -1 to 1, where -1 and 1 means that 100% of the energy is reflected, and no energy is transmitted (Schlumberger, 2017). In general, positive reflection coefficients appear at soft-hard material transitions and negative at hard-soft transitions. For example, interface from water to air, will give a reflection coefficient close to -1. Shale tend to be "softer" than sand, positive reflection coefficient therefore occurs at transitions from shale to sand.

$$R = \frac{Z_2 - Z_1}{Z_2 + Z_1} \qquad (Equation\ 1.9)$$

3.1.4 Wavelet Processing

As a part of the seismic processing, it is necessary to make the effective wavelet shape the same for all traces (Sheriff, 1980). A zero-phase wavelet will often replace the effective wavelet. An

international standard, called the SEG convention is a way of displaying the positive peak as a positive coefficient of reflection, and the negative peak as a negative coefficient. In the SEG standard, this is known as normal or positive polarity. In some cases, it may be convenient to reverse the display convention; i.e. reverse the polarity of the data, which can be done at any time. The type of polarity differs from dataset to dataset due to differences in wavelet of the source and it may be desirable to fit the polarity to the well data, before continuing to work on the seismic data. A minimum-phase wavelet will have most of its energy concentrated in front of the wavelet (Sheriff, 1980). When interpreting seismic it is however more desirable to use a zero-phase wavelet, which are symmetrical with the peak at the central point (Sheriff, 1980). The zero-phase's symmetrical shape gives it the highest peak amplitude of any other signal within the same amplitude spectrum, it also has the shortest duration compared to minimum-phase and mixed-phase signals. This makes it the most desirable signals when it comes to its resolution capability.

3.1.5 Vertical resolution

The vertical resolution in seismic data determines the smallest size an object or a feature can have before it is too small to be observed in the data set. It can be derived from the length of the acoustic wave. Vertical resolution is normally ¼ of the wavelength, giving the equation 1.11 for vertical resolution (Sheriff, 1980).

Wavelength: $$\lambda = \frac{v}{f} \qquad (Equation\ 1.10)$$

Vertical resolution: $$\frac{\lambda}{4} \qquad (Equation\ 1.11)$$

λ = Wavelength, f = seismic frequency, v = Seismic velocity.

This implies that if the thickness of a layer or a feature is less than ¼ of the wavelet, the top and base of the layer may merge into one waveform. This is known as the interference or tuning effect (Fig. 3.5), and is a result of destructive interference (Widess, 1973; Bulat, 2005). If the limit of visibility again is reached, the interference will no longer be destructive, and the top and base may again be distinguished.

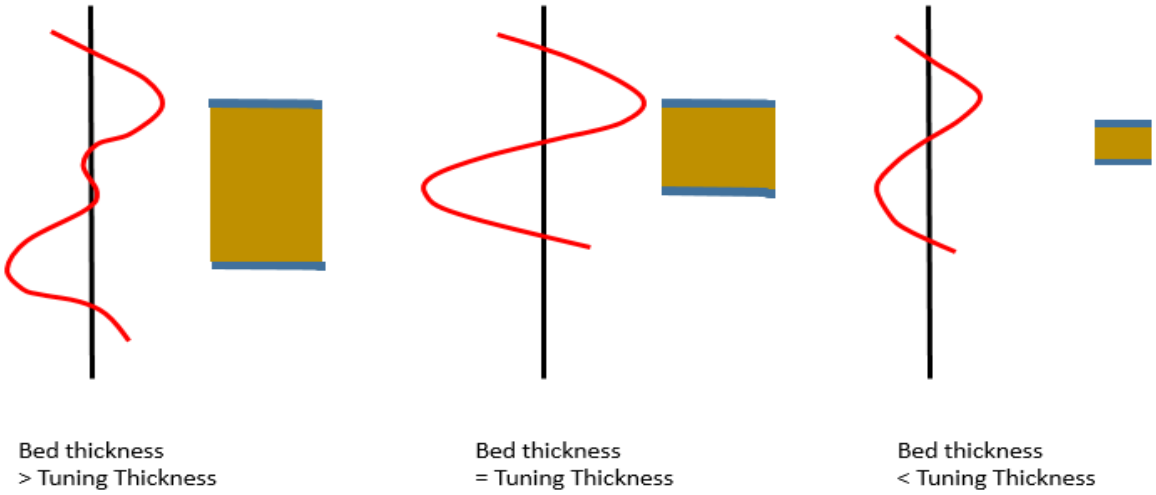

Figure 3.5 *The vertical resolution of seismic waves controls the separability of different layers in the stratigraphy. If the bed thickness is more than the tuning thickness, both the top and the base of the layer will have distinct reflections. If the bed thickness equals the tuning thickness, one reflector will be interpretable, and if the bed thickness is less than the tuning thickness, no distinct reflector will be interpretable. Figure modified after Brown (2004).*

3.1.6 Lateral resolution

Seismic waves are range- and frequency dependent and the energy emitted from a source will target an area not a single point. Most of the energy reflected from this area will return, and the arrival times will differ with less than half a period from the first break (Schlumberger, 2017). This area is known as the Fresnel zone (Fig. 3.6). It is the wavelength of the acoustic signal that determines the radius of the area. As distance from source to depth increases, the wavefront widens (geometrical spreading) with increasing depth. The seismic data's lateral resolution depends on the TWT to the top of the reflector of interest, the interval velocities and the frequency or bandwidth content of the pulse (Veeken, 2013). Higher frequencies will increase the lateral resolution, but the penetration rate for high frequency seismic waves are less than for lower frequencies and the resolution will become less with increasing depth. The Fresnel zone's radius in unmigrated seismic data is given by equation 1.12 (Sheriff, 1985; Chaouch and Mari, 2006).

$$rf = \frac{v}{2}\sqrt{\frac{t}{f}} \qquad (Equation\ 1.12)$$

rf = Radius of the Fresnel Zone (m) , v = Velocity (m/s) , t_0 = TWT (s) , f_{dom} = Dominant frequency (Hz).

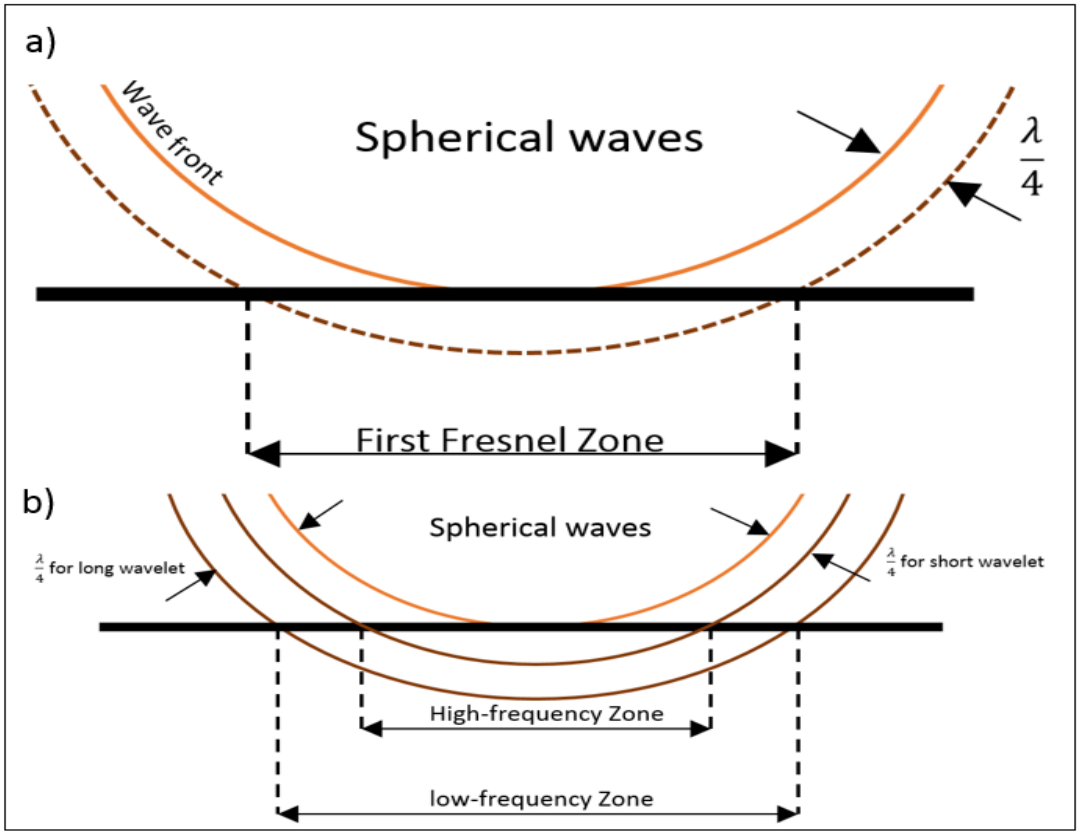

Figure 3.6 a) *The Fresnel Zone defines the area where the wavefront is tangent to the reflector. It is limited by the wavefront circle, which hits the interface 1/4 of the wavelength later.* ***b)*** *Higher frequencies gives higher resolution, as it shrinks the Fresnel Zone. Modified after Sheriff (1980).*

Migration of the seismic data will increase the lateral resolution by shrinking of the Fresnel zone. Migration of seismic data works for both 2D- and 3D seismic data but the effect is greatest with the latter. In 3D seismic data, the Fresnel circle is shrunk down to a small circle, where the energy is better focused, and hence the resolution increases (Sheriff, 1985; Brown, 2004). The lateral resolution for migrated seismic data is somewhat simpler and only depends on the wavelength, equation 1.13.

$$Hr = \frac{\lambda}{4} \qquad (Equation\ 1.13)$$

Hr = Horizontal resolution (m), λ = Wavelength (m)

3.1.7 Well data

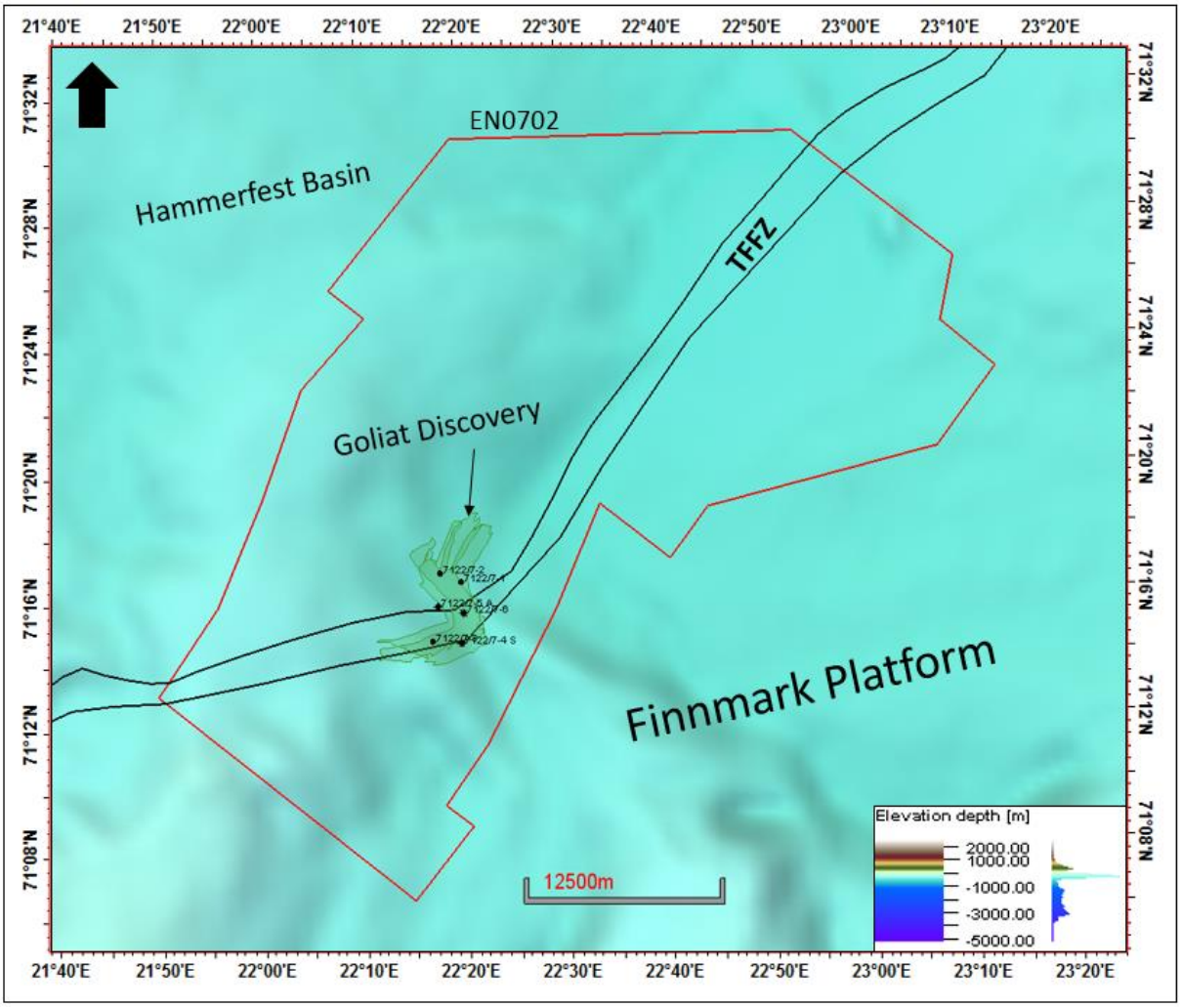

Figure 3.7 *Close-up of area indicated by the black box in Fig. 3.1 with location of wells and outline of the Goliat Discovery*

The offset well data provided by Eni Norge have been used to correlate and establish the seismic stratigraphy over the different lithiostratigraphic units within the study area. The available wells

Data from offset wells 7122/7-1, 7122/7-2, 7122/7-3, 7122/7-4S, 7122/7-5A, and 7122/7-6 where provided. The discovery was made by offset well 7122/7-1, which was drilled as a wildcat well. The offset wells, 7122/7-2, 7122/7-5A and 7122/7-6 are all appraisal wells while the rest are wildcats. All the mentioned offset wells proved to contain either oil or oil and gas columns.

The velocities and thicknesses of the different stratigraphic units and features above the URU where obtained from Andreassen et al. (2008) and (Chand et al., 2008) with 1500 m/s for the water column and 1700 m/s for the glacigenic sediments respectively.

The velocities for the pre-glacial units where obtained from Storvoll et al. (2005) and his paper on the velocity-depth trends in Mesozoic and Cenozoic sediments. Additionally, data from the offset wells have been used to correlate the different stratigraphic units, and the top depth in TWT and TVD are all average measurements (table 3-1). The velocities for the Torsk and Kolmule/Kviting Formations is obtained from the paper by Storvoll et al. (2005) and the velocity profiles he presents. The Top Depth (TVD) is the average depth of the different intervals in the study area.

Table 3-1 *A short summary of the velocities used for calculating the depth of certain geological features including fault throws interpreted in the study area.*

Stratigraphic interval	Top Depth TWT (ms)	Top Depth TVD (m)	P-wave velocity (m/s)
Water column	-	-	1500
Nordland GP	454	386	1700
Torsk FM	526	526	2000
Kolmule/Kviting FM	875	658	2500

Fig. 3.8 shows an idealized sketch of the Goliat rollover structure and the relative position of the different reservoirs, and the stratigraphic units as correlated from well-data and available information from Eni Norge.

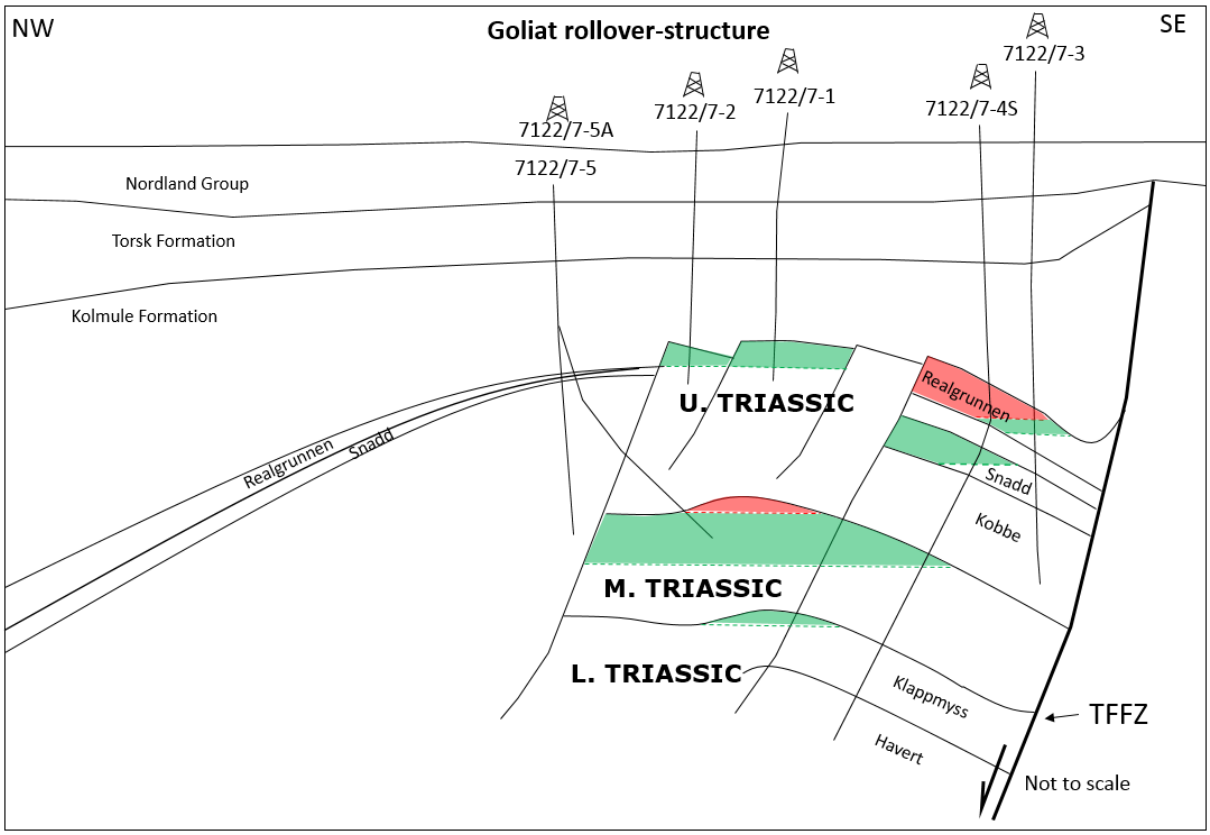

Figure 3.8 *Generalized cross section of the Goliat structure and the relative position of the offset wells and encountered reservoirs. Figure is modified from "Eni Norge – internal figure"*

3.1.8 Seismic interpretation

A frequency spectrum analysis extracted from the seismic, shows that the bandwidth filtering lies between 10-15Hz as a lower boundary and an upper boundary at approx. 80 Hz. The dominant frequency peaks at 50-55 Hz (Fig. 3.9**a)**). The frequency analysis is taken from a representative seismic line crossing the survey area in a NW – SE direction covering the seismic interval of interest. (Fig. 3.9 **b)**).

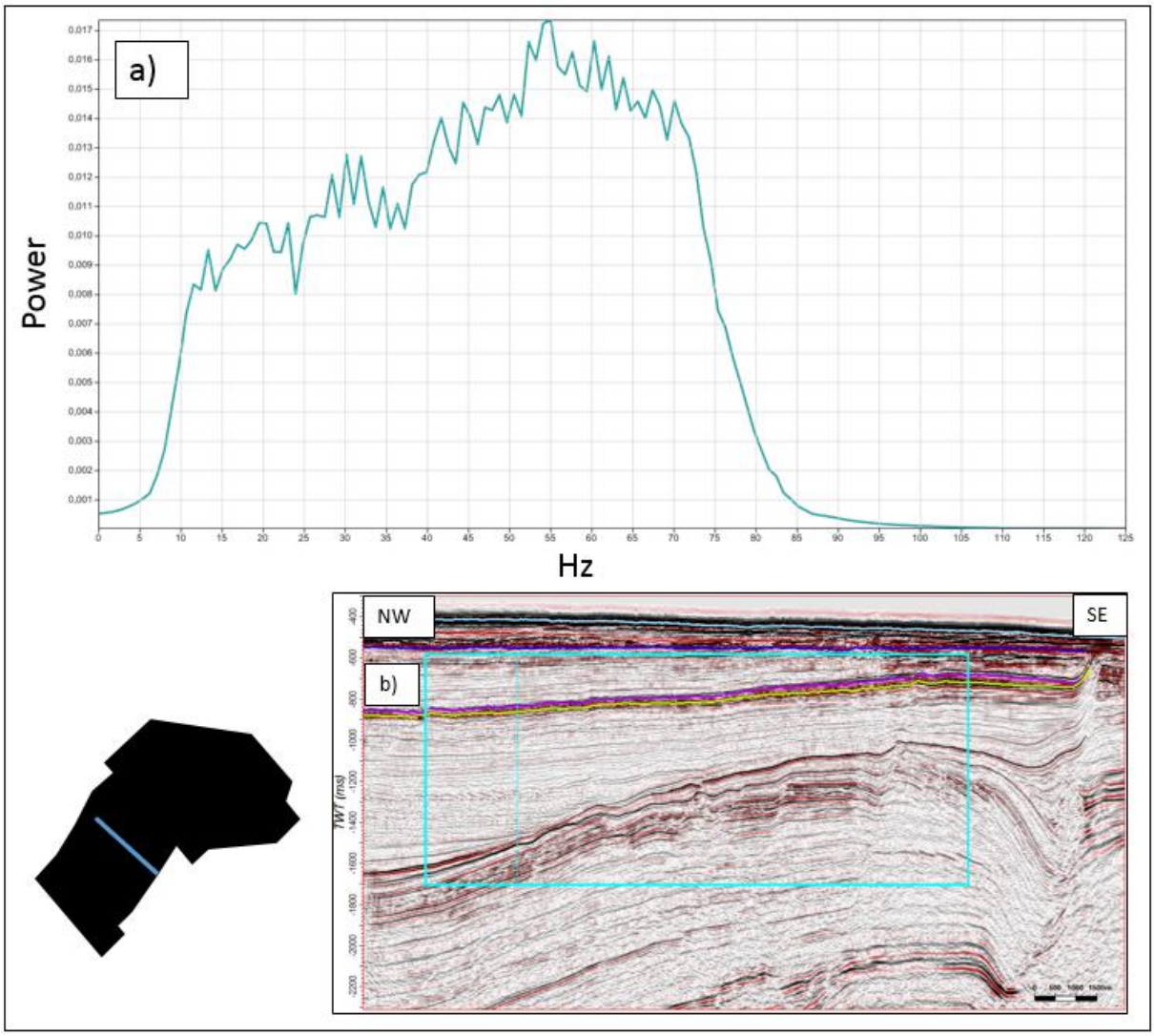

Figure 3.9 a) *Frequency spectrum analysis showing the bandwidth of the seismic data with lower boundary at 10 Hz and upper boundary at approx. 80Hz.* ***b)*** *Seismic section showing where the frequency spectrum were extracted from (blue square)*

All the interpretations in this thesis have been carried out by using the Petrel E&P software version 2012 and 2015. The software is owned and developed by Schlumberger with the intention of using it as a multidisciplinary software for the exploration and petroleum industry. The software allows users to interpret 2D and 3D seismic data, building reservoir models and correlate well data to the seismic data. The software makes it possible to visualize seismic volumes. From the imported data, a number of attributes and calculations can be extracted, along with well path planning. It is important to mention that the Petrel software uses negative Two-way Time (TWT) as annotation for the Y-axis, so that many of the seismic sections and figures will show a negative TWT value, while in the text the TWT value will be positive. The EN0702 dataset is a Time-migrated dataset, which means that all the interpreted horizons

and structures are interpreted in the time-domain. Most of the interpretations of the horizons is carried out by use of 2D auto tracker. For reflectors who are less continuous, the guided auto tracker and manual auto tracker is used. Interpretation of faults is carried out, by placing fault sticks in the seismic profiles, often helped by Variance maps, min. curvature maps and dip/Azimuth maps.

After realizing the data, volumetric attributes like a variance cube were generated and surface attributes were extracted.

3.1.8.1 Variance (Edge method)

The variance attribute (the opposite of coherency) is calculated in three dimensions and represents the trace-to-trace variability, over a particular sample interval, it therefore produces interpretable lateral changes in acoustic impedance. This tool is particularly useful in seismic facies analysis, i.e. making an interpretation of the depositional environment from the seismic. The three dimensional cube allows you to move up and down in time or depth, and to see lateral changes (Fig. 3.10**d)**). Variance attribute is a refined algorithm after the coherence cube (Bahorich and Farmer, 1995).

3.1.8.2 Min Curvature

Curvature is a measure of how deformed a surface is at a particular point (Fig. 3.10 **c)**). This makes the curvature attribute a good tool for interpreting faults

3.1.8.3 RMS amplitude

RMS (Root Mean Square) amplitude is a post-stack attribute that calculates the square root of the sum of the squared amplitudes divided by the number of samples within the specified window used (Fig. 3.10**a)**) (Schlumberger, 2010). The AI contrast between water and hydrocarbons cause reflection events, thus RMS amplitude maps can be used as hydrocarbon indicators. In addition, along with variance maps it is possibly the best tool to do facies analysis from surfaces.

3.1.8.4 Dip angle/Dip azimuth

Dip angle surfaces shows the local dip (gradient) along the surface, whereas dip azimuth shows both angle and direction of the slope measured in degrees, clockwise from north (not to be confused with the geological concept of azimuth) (Fig. 3.10**b)**).

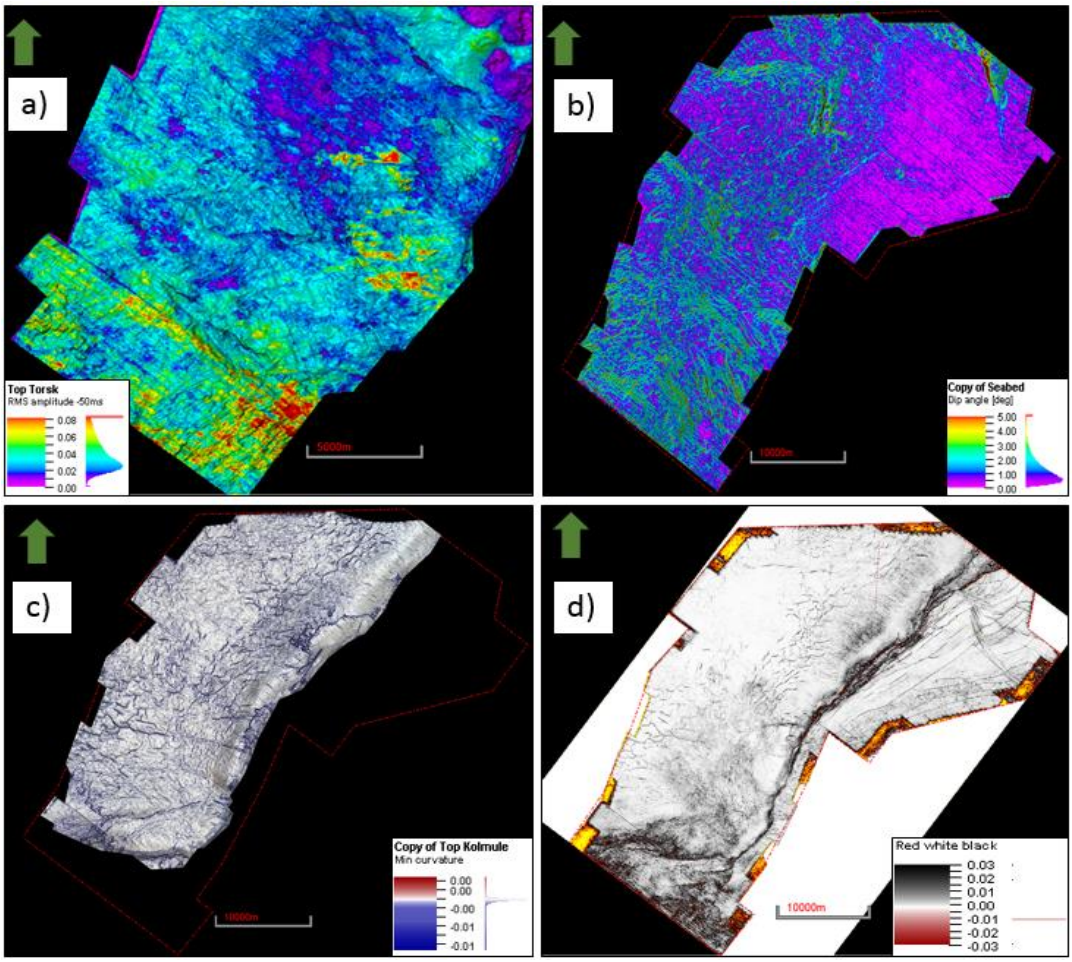

Figure 3.10 *Overview of some of the different attribute maps generated.* ***a)*** *RMS amplitude map,* ***b)*** *Dip angle/Azimuth map,* ***c)*** *min curvature map and* ***d)*** *a TWT slice from the variance attribute.*

4 Results and findings

In this chapter, all the interpretations and observations from the seismic dataset EN0702 will be presented. The main goal has been to establish areas of shallow gas accumulation, fluid flow structures and gas hydrates within the vicinity of the Goliat field (Fig. 2.1) in the South Western Barents Sea. The linkage of these gas accumulations to deeper-seated reservoirs is poorly understood, and it is therefore of interest to increase the understanding of how focused fluid flow and migration of fluids along fault planes contribute to these shallow gas accumulations. It has not been necessary to use any velocity model for converting the interpretations from the time domain. Some of the morphological features, faults, amplitude anomalies and the structural setting have previously been interpreted and described in other published works (e.g. Chand et al. (2009), Indreværet al. (2017)).

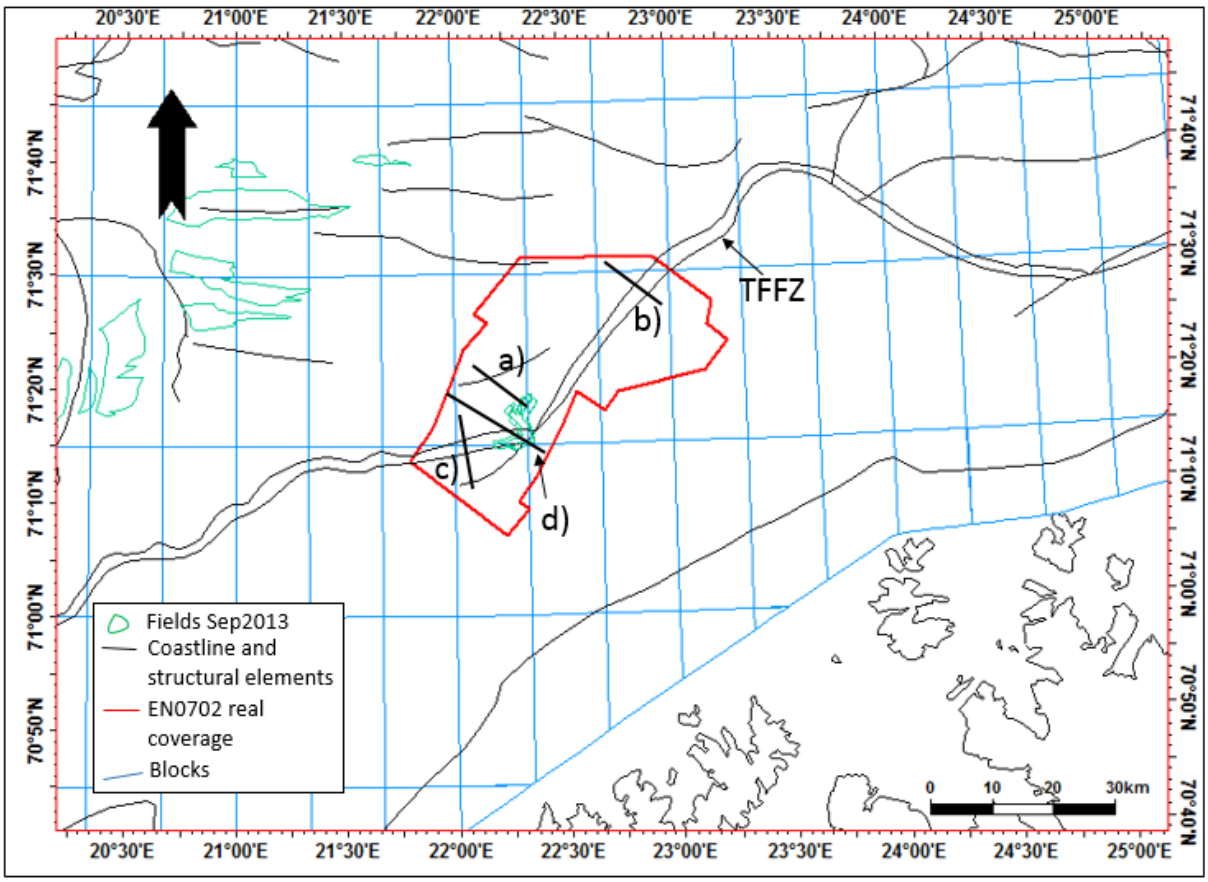

Figure 4.1 *Overview of the EN0702 survey. Red polygon indicate the survey area, while the black lines are seismic profile lines.*

4.1 Seismic Stratigraphy

The seismic stratigraphy for the study area is determined and interpreted from a number of offset wells located within the survey (Fig. 3.7 and 3.8). As mentioned, this thesis focuses on the stratigraphy above the Base Cretaceous Unconformity (Fig 4.2), which also coincides with the Top Knurr Horizon in this dataset. The stratigraphic units identified in the EN0702 dataset include Torsk/URU (Upper Regional Unconformity), Base Tertiary Unconformity and Kolmule/Kviting. The latter units are hard to distinguish in the seismic data due to tuning effects is therefore interpreted as one horizon. The Kolje unit is not included as the transparency of the seismic makes it difficult to follow any reflector laterally and continuously.

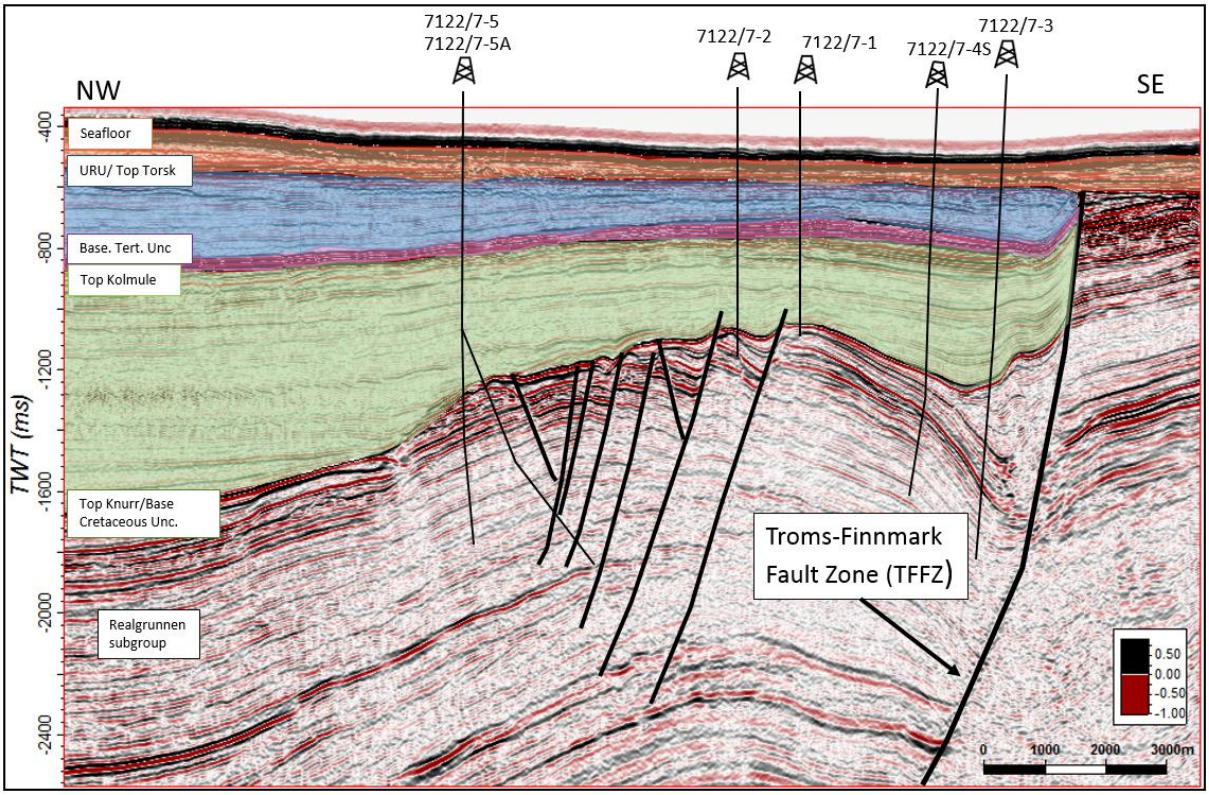

Figure 4.2 *General overview of the seismic stratigraphy and the approximate Well positions. The colours represents the stratigraphic units relevant for this study. The dome shape represents the Goliat structure. The location of the profile is indicated on Fig 4.1 as* ***a)****.*

The Base Cretaceous Unconformity and Lower Cretaceous Knurr Formation lie unconformable on top of the Realgrunnen subgroup (Fig 4.2). It is partly interpreted along a prominent continuous positive reflection coefficient, but as it is an angular unconformity where layers underneath truncate, it is hard to interpret the unconformity along a continuous positive reflector, even though it in most places looks like that. The depth of the reflector varies and is shallower across the rollover structure, where the top reflector appears at 1.2 s (TWT).

Northwest in the study area, the reflector deepens progressively down to around 1.7 s (TWT). The Knurr Formation underneath is heavily affected by the deep-seated faults located between the BCU and some places extending down as or below the seismic penetration (through the Permian section).

The Kolmule Formation belonging to the Adventdalen Group and, here interpreted together with the Kviting Formation from the Nygrunnen Group, exists within the whole Hammerfest Basin. Data from offset well 7122/7-4S suggests a depth of the top Kviting Formation at 592 m (TVD) while Top Kolmule occurs at 603 m (TVD). In offset well 7122/7-5, Top Kolmule lies just lower at 630 m (TVD). On the offset well logs, the basal stratigraphic unit of the Kolmule Formation is defined by a sharp increase in interval transit time and neutron porosity readings. It also shows a slight decrease in the gamma log response. The basal stratigraphic unit of the Kvitingen Formation is marked by a sharp fall in gamma response and interval transit time, including increasing density. In seismic profiles, an interval of high amplitude and strong reflectors identify both units. The vertical resolution in this seismic data set is not sufficient to interpret the two units separately; they are therefore interpreted as one.

In the Study area, the thickness of the Kolmule/Kviting Formation is greatest in the northwest and it is narrower and at shallower depth over the rollover structure. Further north the unit evens out and the lateral thickness varies less. In the northern parts of the survey, the unit occurs between 0.9 s and 1.6 s (TWT) over the rollover, and to the NW of the rollover it thickens to an interval between 0.9 s to 1.8 s (TWT). In the southern area of the survey, the unit is less laterally consistent and occurs between 0.8 s to 1.0 s (TWT) over the rollover, and to the NW it occurs between 0.9 s and 1.6 s (TWT). The unit pinches out towards the TFFZ. The Kolmule unit is heavily influenced by faults of extensional character, some reaching far enough up to penetrate the Torsk Formation, and possibly penetrating the URU. The unit shows a general trend in dip towards NW in the survey area, away from the TFFZ. The unit is clearly dragged upwards by reactivation of the TFFZ and the drag cause formation of a small depo-centre in front of the TFFZ (Fig 4.2).

The Base Tertiary Unconformity (BTU) is identified in the well logs by a sharp increase in the Sonic Compressional log. The layer below the BTU surface is thin compared to the other units, and lay almost parallel with the Kolmule/Kviting Formation. The lateral thickness appears to be almost constant in the whole study area, with a thickness generally around 40 ms (TWT).

The unit is near horizontal in the northern parts of the study area where it occurs between 0.87 s and 0.9 s (TWT). In the southern parts of the area, the layer follows the Kolmule trend and is shallower over the rollover structure where it occurs between 0.72 s and 0.76 s (TWT), while NW of the structure it occurs between 0.87 s and 0.9 s (TWT). The unit pinches out towards the TFFZ.

The Torsk Formation belonging to the Sotbakken group overlies the Nygrunnen group and is traceable throughout the whole study area. In the northern parts of the survey, it occurs between 0.6 s and 0.9 s (TWT) and is lateral continuous. Further south, the unit shows a more uneven thickness, with less thickness over the rollover structure. Here it occurs between 0.6 and 0.8 s (TWT). The irregular thickness increases even more to the south where it thins out to an interval between 0.5 s and 0.7 (TWT) over the rollover, and to the NW it thickens and occurs between 0.5 s and 0.9 s (TWT). In the north, sediments have been eroded all the way down to the upper boundary of the Torsk Formation, and in some areas, only a thin layer of the glacigenic Nordland Group separates it from the seabed. The reflectivity within the Torsk Formation varies from continuous reflectors to more transparent, low amplitude reflectors with less continuity. Clinoforms dipping in a south- and southwestern direction are traceable in the whole study area, where they also pinch out towards the TFFZ (Fig. 4.2). The clinoform shows high continuity except in areas where the seismic is more chaotic or seismic discontinuities obscure the reflectors. The seismic amplitudes are higher towards the top of the formation and lower at the base towards the Base Tertiary Unconformity.

4.1.1 Upper regional unconformity

The Upper Regional Unconformity (URU) represents the boundary between the underlying Paleogene – Neogene sediments and the overlying glacigenic Pleistocene deposits.

The Fennoscandian shield including the Barents Sea has undergone several glaciations since the Pliocene (Vorren et al., 1991; Svendsen et al., 2004; Andreassen et al., 2007b). On seismic profiles, the URU is easily recognised by a strong positive reflector. In the EN0702 dataset, the Top Torsk horizon represents the URU, that is traceable throughout the whole study area, but some places are hard to interpret. In the northern parts of the study area, it occurs up to 30 ms (TWT) below the seafloor and some places coincide with the seafloor, while further south it lies deeper, up to 137 ms (TWT) below the seafloor.

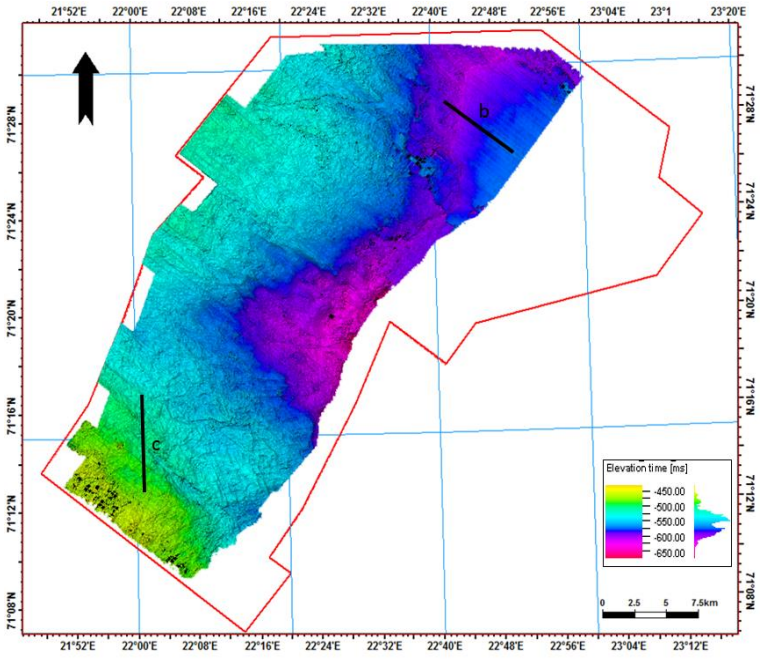

Figure 4.3 *Map view of the URU. The poor quality of the seismic imaging and the low lateral continuity of the horizon makes the interpretation of the URU particularly difficult. (Fig 4.4).*

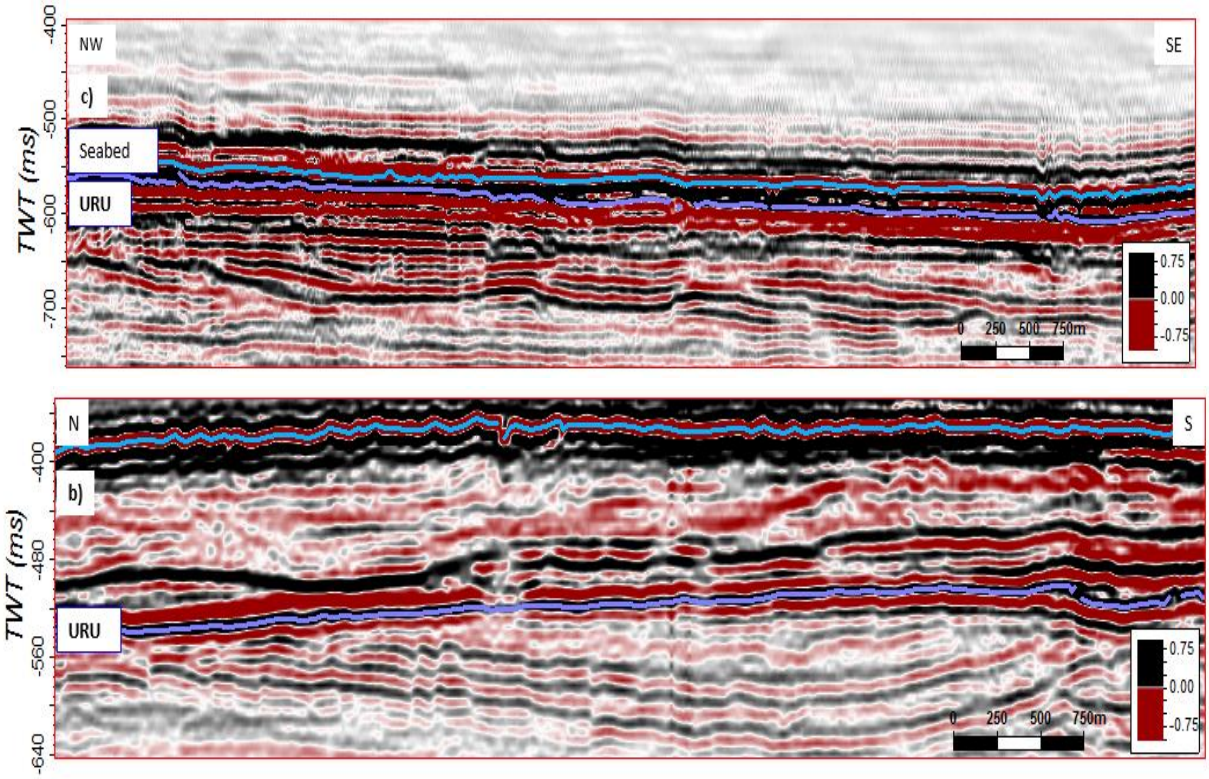

Figure 4.4 *Seismic profile lines showing the difference between the southern and northern parts of the survey in thickness of the Torsk formation, and the depth from seabed to the URU.* ***b)*** *In the northern parts the sediment cover (Nordland Group) are thicker and the depth down to the URU is greater.* ***c)*** *In the southern parts, the URU parallels the Seabed and at some points coincides with the seabed with only a thin layer of sediment cover. Profile lines are also shown on Fig. 4.1 as* ***b)*** *and* ***c)***

4.1.2 Seafloor

The seafloor in the study area is highly affected by glacial erosion. Elongated, curved and linear features and seabed depressions characterizes it (Fig 4.5 and 4.6). The furrows and lineations are interpreted to be plough marks and scouring sculpted by icebergs, fragments broken off the terminus of the large ice shields covering the Fennoscandia during the Late Weichselian, and driven by wind and the ocean currents (Andreassen et al., 2007b; Andreassen et al., 2008; Winsborrow et al., 2010). The furrows, and plough marks show two dominant directions: SW – NE and NW – SE, apart from this, many of the smaller plough marks are oriented in all directions, some even crossing each other's paths, indicating that there were more than one period of icebergs breaking of the ice shield. Some of the elongations in the southeast of the study area are parallel, over 7 km long, furrows interpreted as scours, made by rocks trapped under the glacial base. Some of them have rounded bases while others have sharper, more V-shaped bottoms, with depths from 20 ms (TWT) to less than 10 ms (TWT) corresponding to depths 15 and 7.7 m (Vp = 1500). The likely explanation for this is scouring at the base of the glaciers by rocks trapped under the ice along the seabed. The plough marks and glacial features are mostly confined to the shallow Tromsøflaket area to the west and southwest of the study area, and a prominent change in the seabed morphology is visible when looking at the deeper area of Ingøydjupet to the East and northeast of the survey area. Here the laterally flat, deeper seafloor is covered in thousands of smaller circular to sub-circular depressions. The depressions are interpreted as pockmarks (Chand et al., 2009), and have a density of up to more than 165 pockmarks/km^2 in the study area.

The strong seabed reflection and high spatial resolution in the seismic survey, gives a good insight to the morphological features on the seafloor (Fig. 4.6). The water depth in the study area varies from 360 – 420 meters, with the shallowest area to the south west of the survey and the deepest parts in the northeast area. The deepest water depths are found in Ingøydjupet, which occur as a laterally flat platform area with less prominent morphological features, compared to the shallower Tromsøflaket in the southwest and western parts of the study area (Fig. 4.6). The shallower area is situated on the eastern boarder of the shallow Tromsøflaket (Winsborrow et al., 2010). The water depths gradually increase towards east, now entering the Ingøydjupet, a deep glacial trough. This is the area where the highest density of pockmarks occurs. The shallower areas show a lower distribution of the circular depressions, however, these depressions are of much greater size.

The large parallel lineations in the SE corner (Fig. 4.5 and Fig. 4.6**a**), of the survey area are interpreted to be glacial lineations (not to be confused with mega scale glacial lineations). Several of the smaller plough marks are crossing the glacial lineations, indicating that they are of a younger age, most likely from the time when the ice shield retreated and the front of the glacier became unstable leading to the break-off of multiple smaller icebergs.

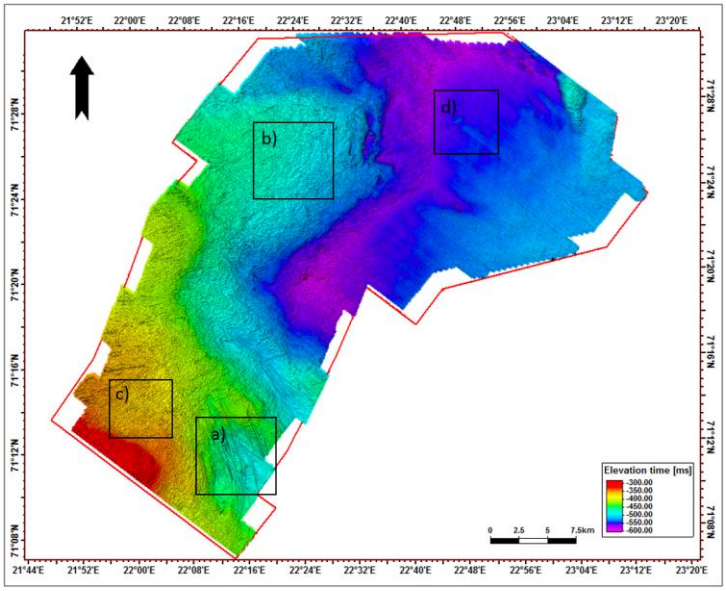

Figure 4.5 *Map view of the seabed based on the seismic interpretation of the seabed reflector. The legend shows the TWT in ms. The black squares indicates the areas shown in Fig. 4.6.*

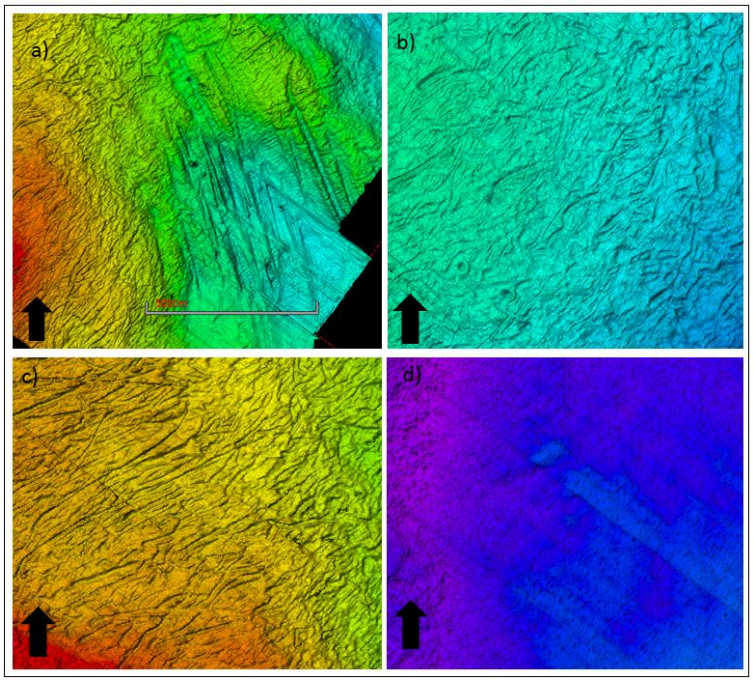

Figure 4.6 *Overview of some of the different morphological shapes and features observed on the seabed within the study area.* ***a)***, ***b)*** *and* ***c)*** *shows the different plough-marks and glacial features.* ***d)*** *Area with high density of pockmarks. Locations of the different areas can be seen in Fig. 4.5*

4.2 Faults

In the dataset there are several stratigraphic units containing faults with different character. As this thesis focuses on the shallow horizons, the attention is towards the units above the Base Cretaceous Unconformity, but it also discusses a possible relationship between the deeper-seated faults, and the shallower structures. Deeper-seated faults are defined in this study as any faults that terminate below or any fault that bisects the Base Cretaceous Unconformity. Shallower faults are mainly confined to the intra Kolmule/Kviting and Kolje units, and terminate in the Base Tertiary Unconformity or within the Torsk formation.

4.2.1 Deep-seated faults

Deep-seated faults are in this study defined as any fault that affects the strata below the Kolmule Formation. They are not considered in detail in this study, as the focus of this study is the shallow stratigraphy above the Base Cretaceous Unconformity. Some of the deeper-seated faults penetrate the Torsk Formation, and possibly also the URU. In areas where they show a relationship to the shallower structures, they will however be mentioned and described in more detail if necessary. For a complete overview of all the different faults described in this chapter, Fig. 4.14 shows a seismic section cutting the rollover structure in a NW – SE direction with all fault-types and intervals they affect marked on the figure.

4.2.2 Faults within the Kolmule/Kviting Formation

Faults appear as discontinuities in the more lateral reflectors, and reveal a complex and chaotic pattern. The combination of time variance and minimum curvature maps show that the fault's extend throughout the whole study area, with an especially high intensity over the rollover structure. Some of these faults are hard to interpret on the seismic profiles, but they appear on the curvature and time slices from the variance cube. The dominant strike orientation are NE – SW, E – W and N - S, and the interpreted faults are all thought to be extensional, polygonal faults. Interpreted from time slice 800 ms to 900 ms (TWT) (Fig. 4.7) it can be seen that the faults are tilted in opposite directions, with a dominant dip in NW-SE and WNW-ESE directions. Faults with infinitesimal throw may not show in the seismic as the vertical and horizontal resolution is not sufficient to distinguish the throw of these faults. The faults are interpreted to be polygonal faults due to their seismic character and closely spacing (Fig. 4.7).

Faults NW of the rollover structure show a general strike trend towards WNW-ESE direction, with closely spaced segments varying in length from 964 m to segments who have merged and now have a total length of 7276 m. In map view, the segments appear to be 200 m to 854 m apart, and they are dipping in NE-SW direction. There is a prominent change in the nature of the WNW-ESE trending faults further north in the area, and especially over the rollover structure the nature of the segments trend dominantly in the WSW-NEN direction. The Faults generally terminate in the URU or Torsk Formation, but only a few of them are traceable in the Torsk formation due to poor image quality and seismic transparency. The majority of the faults have vertical displacement in the range of 12 - 20 ms (TWT) which corresponds to 15 – 25m (TVD) (Vp = 2500m/s) and the displacement seems to be more or less constant down the fault planes.

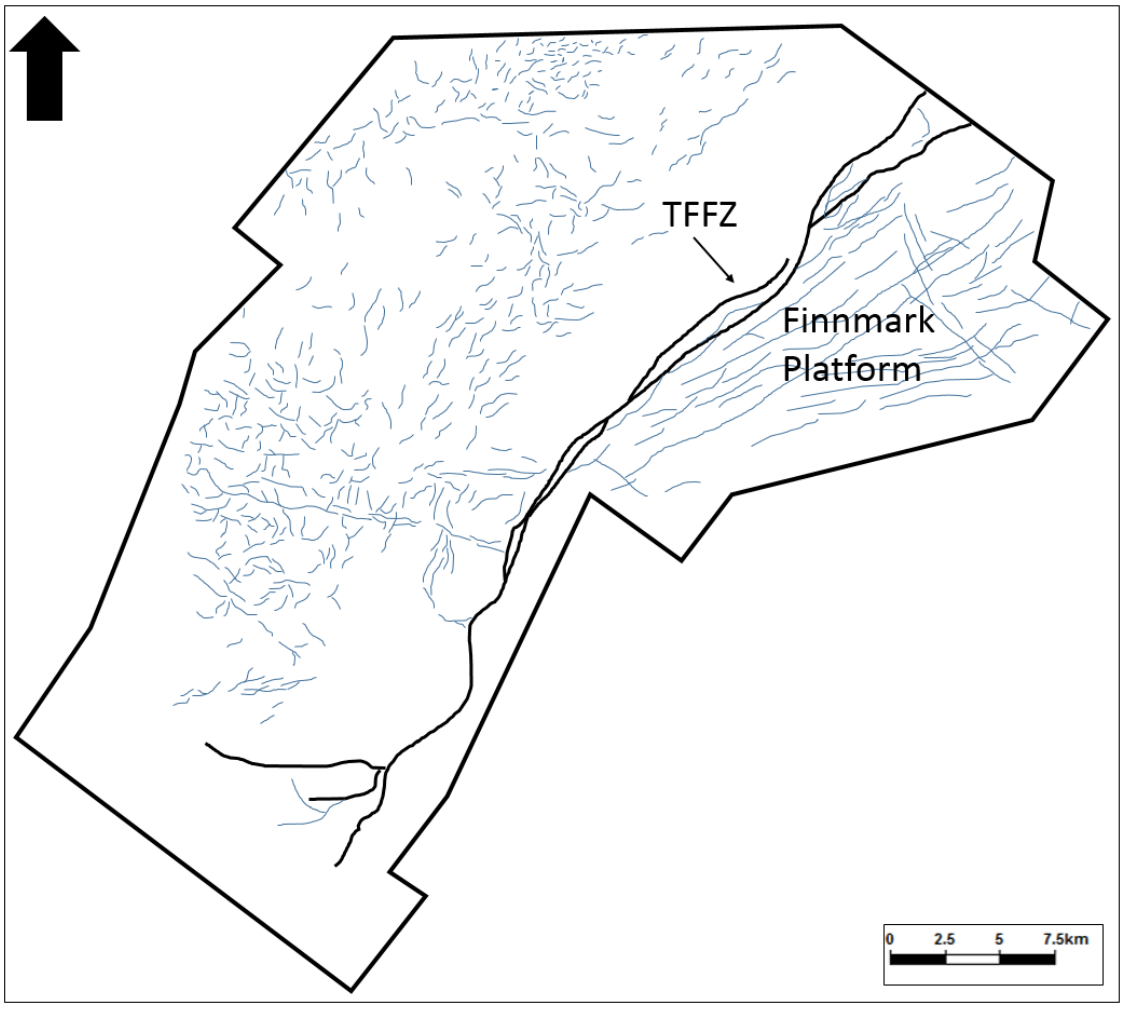

Figure 4.7 *Schematic overview of the polygonal faults in the Kolmule/Kviting formation, based on time slices from variance maps. Some of these may terminate in the Torsk formation (Fig 4.8 and 4.9). The black outline represents the TFFZ. The blue lines east of the TFFZ are not considered in this study. The blue lines west of the TFFZ are the polygonal faults interpreted in the Kolmule/Kviting formation.*

4.2.3 Faults Terminating in Torsk

In the northern parts of the survey area, coherent noise (Fig. 4.8) is disrupting the seismic imaging so much that interpretation of faults, especially the faults terminating in the Torsk Formation, is nearly impossible from the variance attribute time slices. Figure 4.8 shows a variance time slice at 788 ms (TWT), indicating that the faults seen on the seismic section are not interpretable in plain view. The noise and disruption in the seismic image makes it difficult to pinpoint the termination of many of the faults in the Torsk Formation. Additionally, the fault throw may be below the seismic resolution. Especially in the northern parts of the study area, the seismic transparency hides the fault signatures both from the variance time slices and from the minimum curvature attribute. Where the Torsk Formation is thicker and deeper in the south, the faults are more recognizable in the seismic sections, as well as from the variance time slices (Fig. 4.8 and 4.9).

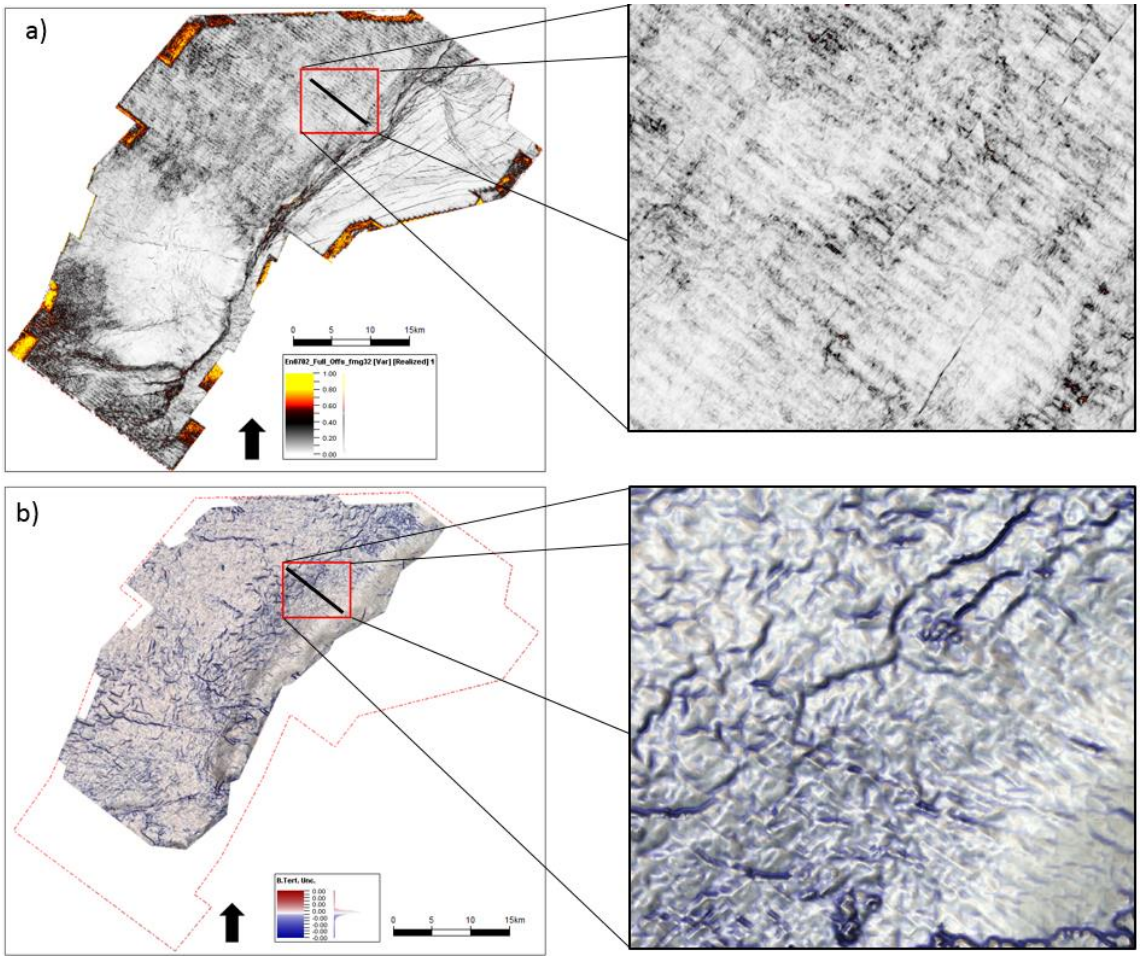

Figure 4.8 a) *A variance time slice at 782 ms (TWT) from the lower Torsk Formation compared to a min. curvature extraction* ***b)*** *of the Top Kolmule/Kviting horizon. It is clear that many of the faults terminate within the Torsk Formation, although they are not interpretable from the seismic sections. In the close-up of* ***a)*** *the NW – SE parallel lines are most likely the expression of coherent noise as mentioned in 3.1.1*

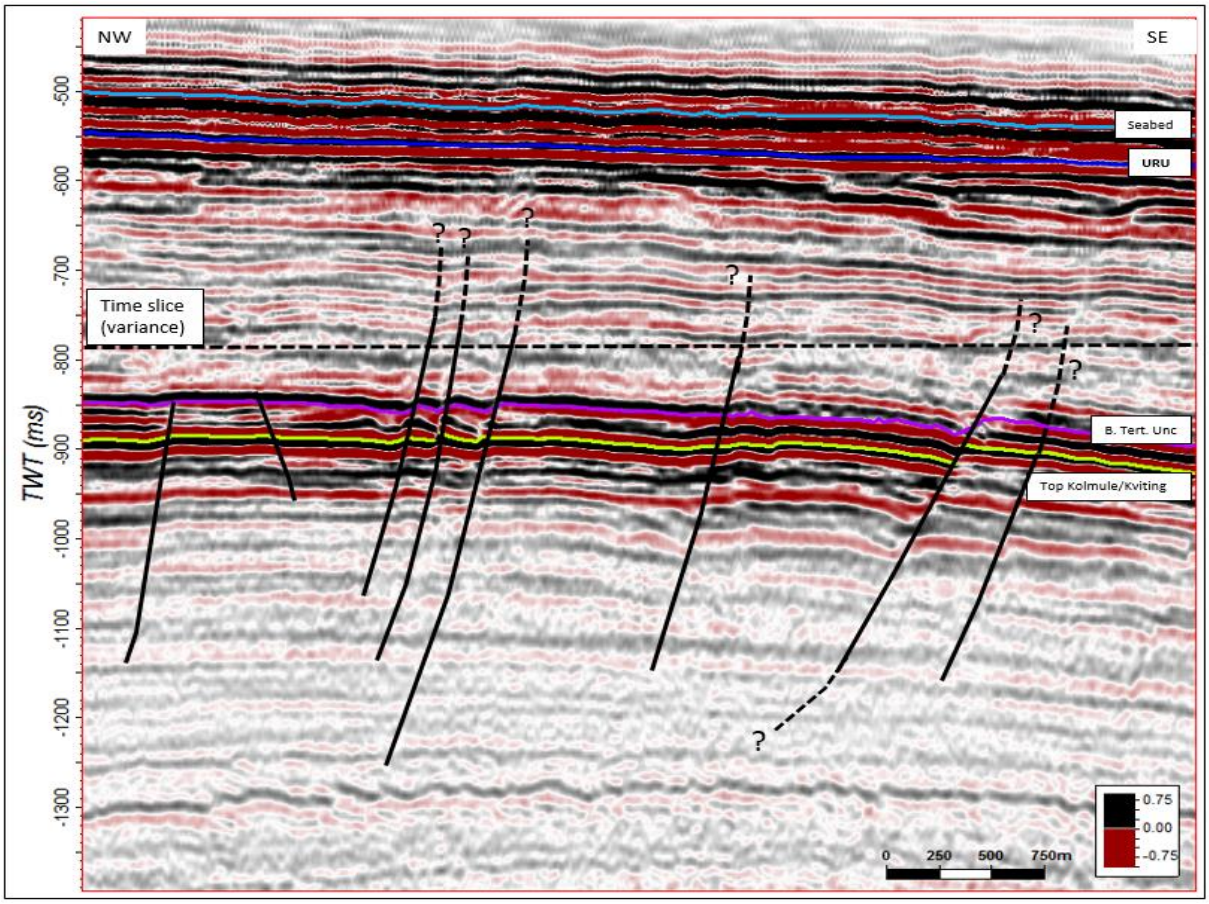

Figure 4.9 *Seismic section (location of profile indicated in Fig. 4.8) of faults terminating in the Torsk Formation. It is difficult to pinpoint their upper and lower termination, most likely because the throw is below the seismic resolution.*

To deal with this problem, the continuous attribute and, minimum curvature was calculated for the BTU surface. The curvature map reveals a similar pattern and complexity of fault segments compared to the southern area in the survey. The distortion of the seismic is most prominent right above the BTU, but by comparing a variance time slice from 870 ms (TWT) with a minimum curvature map from the BTU (Fig 4.10), it becomes clear that the faults extend into much shallower strata than what is interpretable from the variance map. The curvature map shows the maximum deformation of the reflectors, while the variance map shows the trace-to-trace variability, over a particular sample interval, and therefore produces interpretable lateral changes in acoustic impedance. The 870 ms (TWT) time slice also reveals a rectangular pattern (seen on the variance map in Fig 4.10) of small fault segments varying in lengths of 100 – 300 m. They are closely spaced from 140 to 203 m with displacements between 10 ms (TWT) and 18 ms (TWT) which corresponds to 10 – 18 m within the Torsk Formation (TVD) (Vp = 2000m/s). On the seismic profiles, these faults reach down to approximately 1,4 s (TWT), almost traceable down to the BCU, and the length of the fault planes vary from 447 ms (TWT)

to 560 ms (TWT). The location of the area is indicated in Fig. 4.1 and 4.6. The faults terminating in the Torsk Formation show a general trend similar to the intra Kolmule formation (Fig. 4.7). Fig 4.10, which shows a variance time slice along with the curvature map, revealing that the rectangular pattern of faults is only found close to the TFFZ, an indication that the stress field here was much larger, causing more closely spaced faulting.

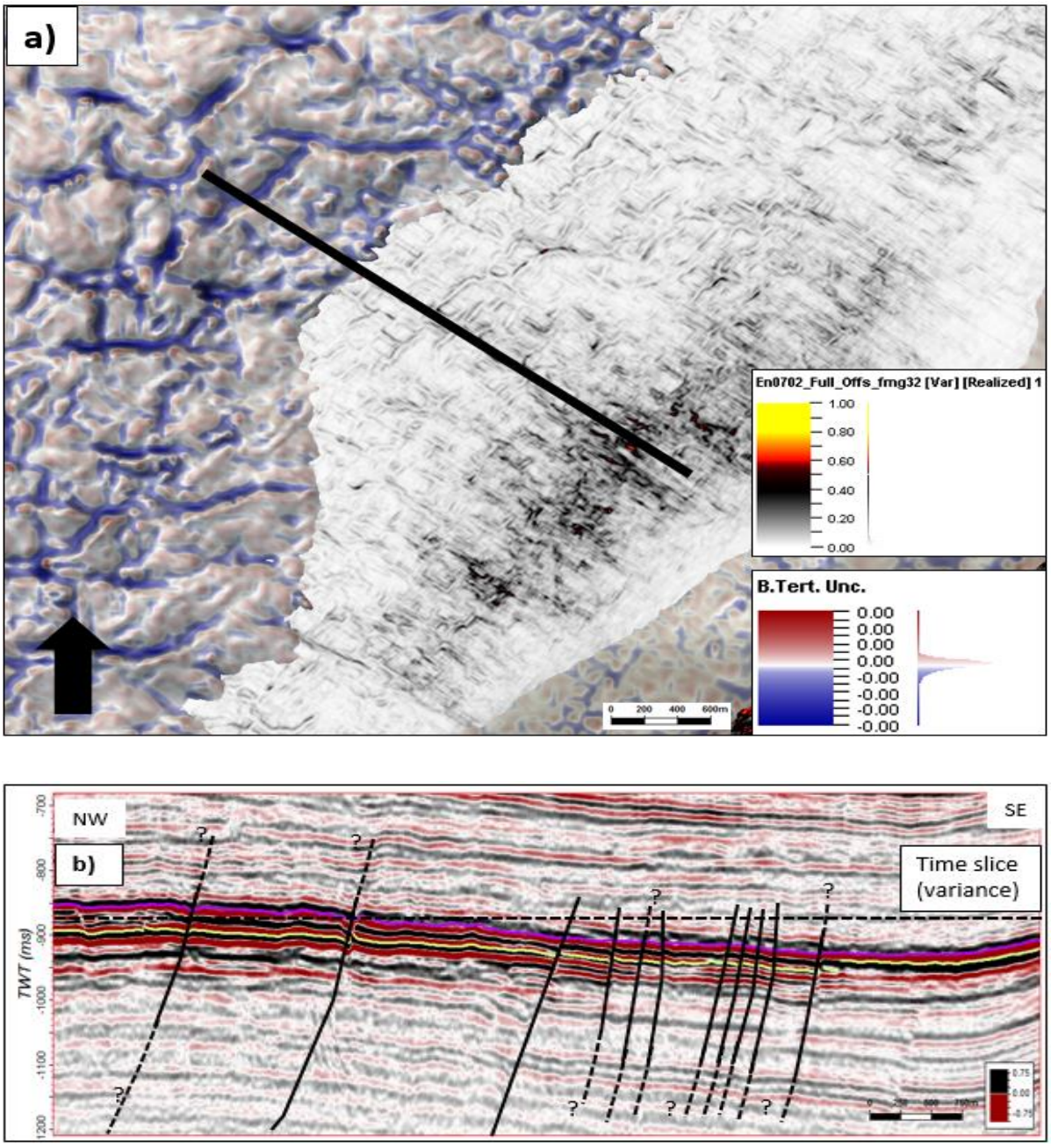

Figure 4.10 a) *A composite image with a min. curvature map overlapping a time variance slice at 880 ms (TWT). The fault structure changes from more widely spaced faults to very narrow and closely spaced faults near the rollover structure, and can be observed as a square-pattern on the variance time slice. Location of area is marked by a red square in Fig 4.8* ***b)*** *Seismic section as indicated in* ***a)****, showing that the faults are much more closely spaced towards the east.*

4.2.4 Polygonal faults in the lower Kolmule Formation

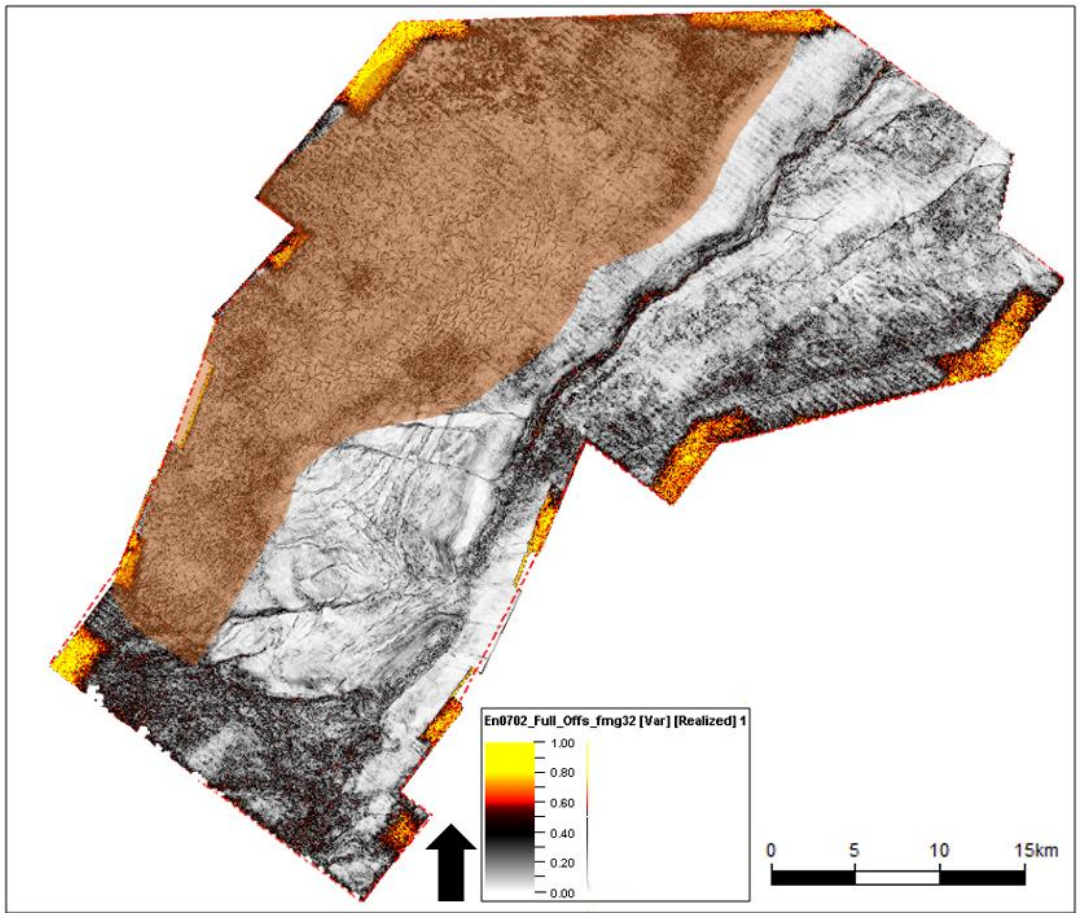

Figure 4.11 *Overview of the area where the polygonal faults occur. They are confined to the area west of the TFFZ, and west of the Goliat Structure. Further north they also appear over the rollover as the thickness of the overburden increases. They occur in a time window between 1.2 s and 1.5 s (TWT) within the lower Kolmule Formation.*

Time slices from the variance attribute reveal a polygonal pattern in the western parts of the study area that stretches over 41 km in the SW – NE direction and up to 15 km in the NW – SE direction. These are interpreted to be a tier of polygonal faults, and they occur in the lower parts of the Kolmule unit. They are confined to approximately 1.2 s (TWT) and 1.5 s (TWT) (Fig. 4.13), so they belong to the Lower Cretaceous strata. The closely spaced faults cover a total area of close to 350 km^2 in the study area. The length of the segments vary from 120 m to 560 m and they are closely spaced with around 100 meters between some of the segments (Fig. 4.10 a and b), and possibly less than that. They have a linear to curved shape with some overlapping segments in plain view. The distribution of the polygonal faults increases northwards in the study area, but common for all of them is the low vertical displacement of 10 to 20 ms (TWT)

which corresponds to 12,5 – 25 m (TVD) (Vp = 2500 m/s) respectively. The segments dominantly show three different strikes in NE – SW, NNW-SSE and E - W directions. In profile view, they share similar characteristics to extensional faults with dip in opposite directions. The interpretable depth of the faults are between 150 ms and 210 ms on the seismic profiles. Other studies from the Hammerfest basin (Ostanin et al., 2012) found the polygonal fault's base to terminate in the Top Kolje horizon, but from the seismic in the EN0702 dataset, this cannot be confirmed. Albeit, the polygonal faults lower base do terminate in a surface with stronger positive amplitude, which may represent the Kolje Formation reflector.

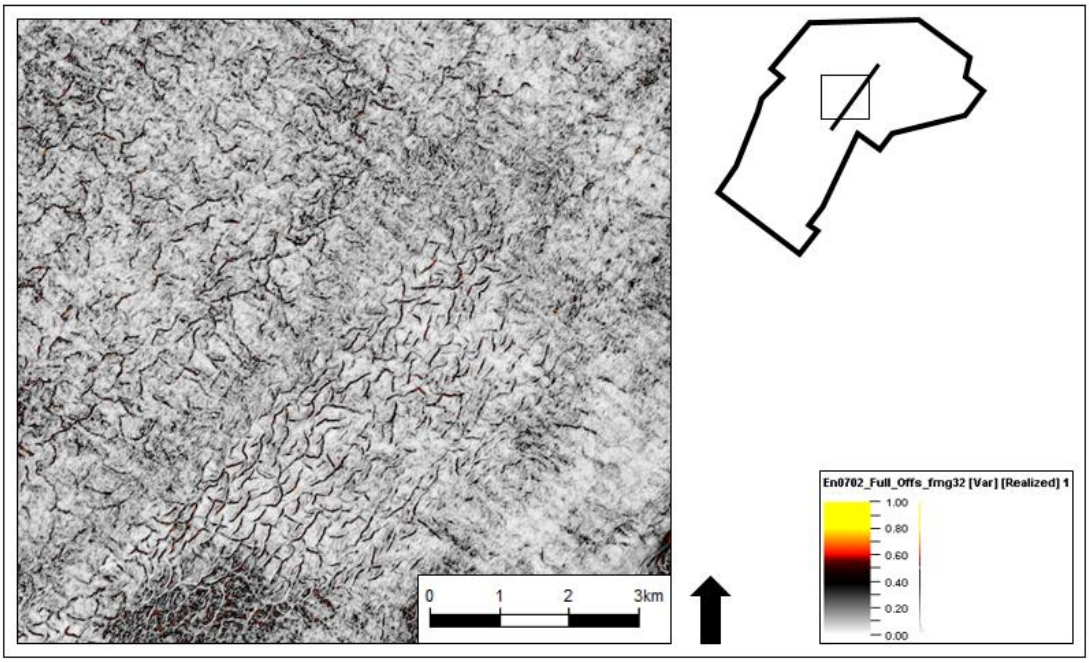

Figure 4.12 *Close-up of the lower Kolmule Formation polygonal fault tier's extent. Location of a) is shown in black polygon to the right.*

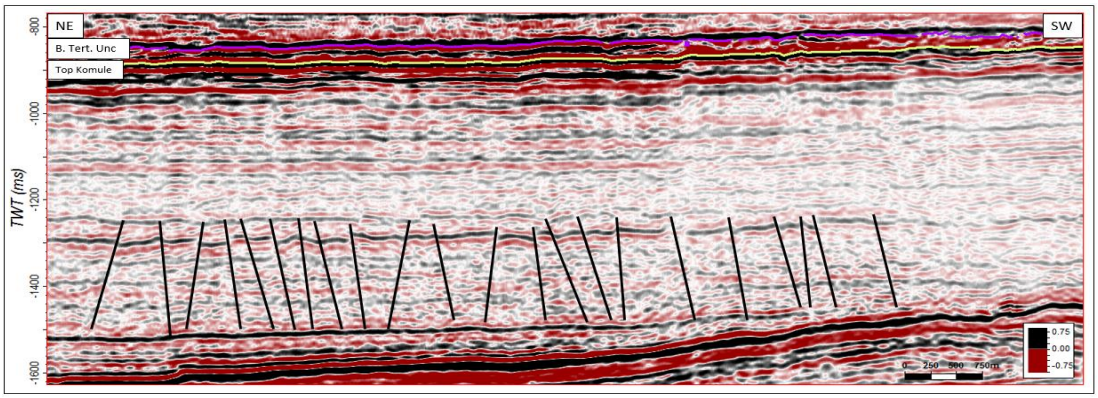

Figure 4.13 *Seismic profile (see polygon in Fig. 4.12 for location) showing the polygonal fault tier. They are confined to between 1200 ms (TWT) and 1500 ms (TWT) in the Lower Kolmule Formation.*

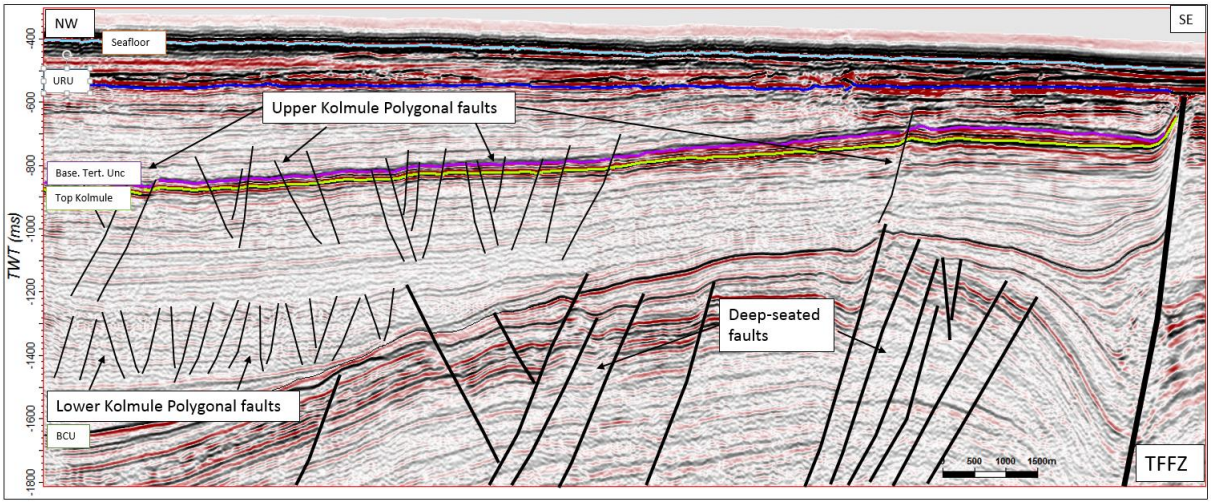

Figure 4.14 *Overview of the different faults described in the previous sub chapters, from a seismic line crossing the survey area in a NW - SE direction. Location of seismic line is marked in Fig. 4.1 as* ***d)****.*

4.3 Indications of focused fluid flow

In areas where fluids are present in the subsurface, faults may act as conducts for fluids, giving the fluids a passage to the shallower strata, where it may accumulate or continue towards the surface. The source of the fluids in the Goliat area is most likely the deeper-seated reservoirs expelling hydrocarbons along non-sealing faults. Possible fluid flow along fault planes can be observed on several locations in the study area, where some of them, also coincide with shallow amplitude anomalies. In other areas, the fluid flow structures are associated with pockmarks and mega scale depressions.

4.3.1 Fluid flow anomalies associated with fault planes.

Fig 4.36 is a seismic profile from the northern parts of the study area. The shallow fault penetrating through the Kolmule formation and up into the Torsk Formation is a SW – NE striking fault, sharing the same characteristics as the mentioned shallow faults in chapter 4.2.1 and 4.2.2. The deeper-seated fault beneath, penetrates down in the Jurassic strata, and possibly even down into the Permian strata. The deep-seated fault is a WNW – SES striking fault with a throw of roughly 30 ms (TWT). The shallow fault is traceable for about 600 ms (TWT) from the top termination to the base, but the transparency of the seismic makes it difficult to be exact. In front of the shallow fault, at 45 ms (TWT) below the Top Kolmule horizon, an area with higher amplitudes is visible. This could indicate that fluids are trapped here. Where the fault penetrates the BTU, there is acoustic masking and pushdown, possibly due to the presence of

gas. The Fluid flow structure coincide with the area where the glacial deposits have been completely removed, and the URU reaches the seabed.

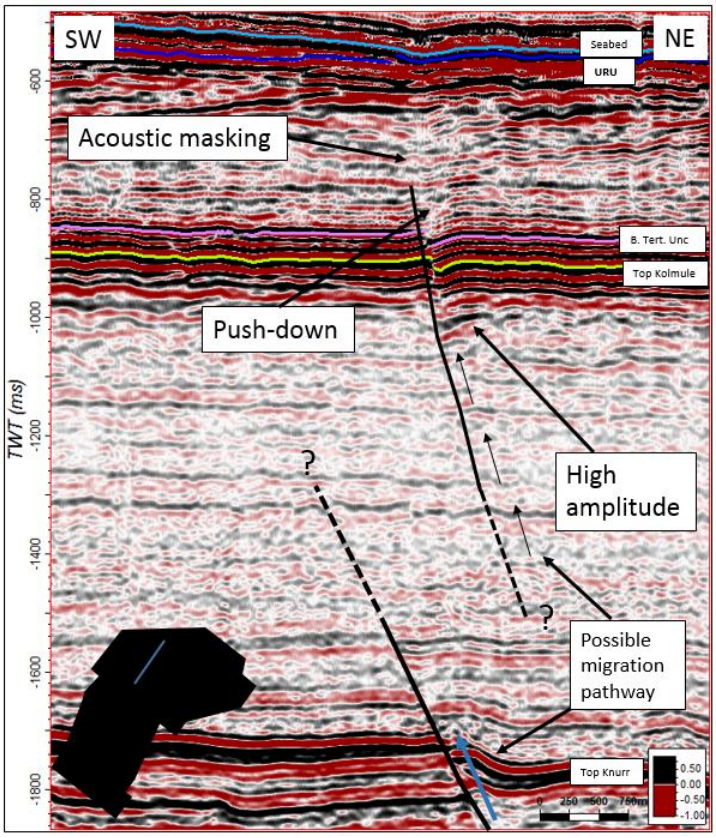

Figure 4.15 *Indications of fluid flow along a fault bisecting the Top Kolmule/Kviting and BTU reflectors. The high amplitude area in front (to the right in the figure) of the fault indicates that gas is accumulation in this area. The acoustic masking and pushdown of reflectors where the fault bisects the BTU reflector indicates fluid flow into the Torsk Formation. Location of profile line is indicated in the black EN0702 survey polygon.*

Further south in the study area (Fig 4.16 and Fig. 4.17), two vertical columnar structures are visible within the Torsk formation. Both of the vertical columnar structures have higher amplitudes than the surrounding reflectors, and there are pushdowns in both of them. They coincide with two shallow faults penetrating through the Kolmule formation with an upper termination within the Torsk Formation. In the structure furthest to the SW, the URU reflector is highly disturbed right above the columnar structure. Both of the shallow faults have a WNW – ESE strike, and lie on top of two deeper-seated faults, penetrating through the Jurassic strata, possibly the Permian strata and up in the Knurr formation. They have the same WNW – SES strike as the shallow faults. The vertical columnar structure is approximately 180 ms (TWT) with a lateral distribution of 120 m. The upper termination of the shallow faults is difficult to interpret, but the vertical columnar structures are visible from the area the faults penetrate the BTU indicating that the sediments in the Torsk Formation have higher percolation rates through

the sediments compared to the Kolmule formation. The throw of the deeper-seated faults in Fig. 4.14 is up to 100 ms (TWT) compared to the 14 ms (TWT) throw of the shallow faults. The high throw of the deeper faults displaces thicker packages of strata, which increases the risk of leaking along the fault plane (as impermeable layers might be displaced towards permeable layers). The vertical columnar structures can be a result of fluid flow, in what previous articles (e.g. (Løseth et al., 2009)) are referring to as pipe structures. They are therefore denoted as pipe structures as from now in this work.

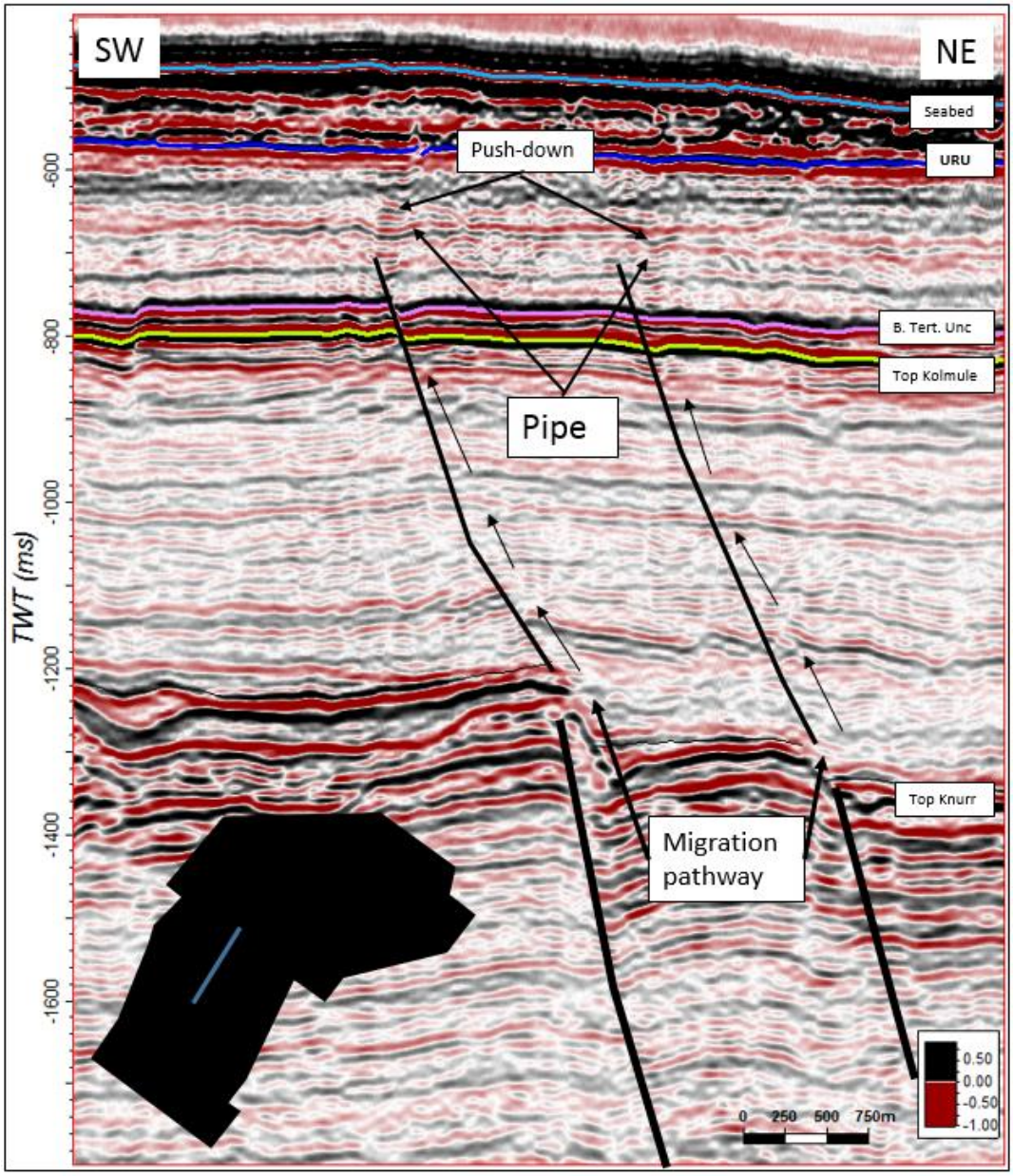

Figure 4.16 *Two faults bisecting the Top Kolmule/Kviting and BTU reflectors have two underlying deep-seated faults. At the upper fault termination 'of the Kolmule - Torsk faults, pushdowns and pipe-structures indicates fluid flow. Possible migration pathways are indicated with black arrows. Location of profile line is indicated in the black EN0702 survey polygon.*

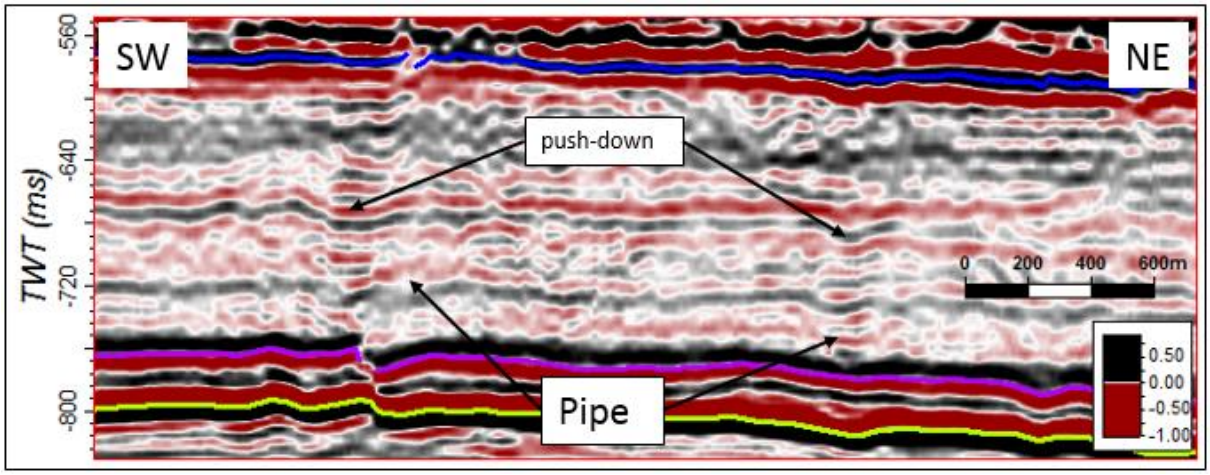

Figure 4.17 *Close-up of pipe structures indicated in Fig. 2.26, showing pushdown and increased amplitudes in the pipe structures above the upper fault tips.*

Further south in the survey area, over the Goliat rollover, another pipe structure is visible in the seismic profile (Fig 4.18), coinciding the AA10 mentioned in chapter 4.4 and 4.4.10. The pipe structures mark the NW boundary of the AA10, and could possibly be the source of the anomaly. The pipe structures originate from a shallow fault penetrating through the Kolmule formation and up into the Torsk formation, terminating some 75 ms (TWT) below the URU. The shallow faults have a SW – NE strike, which coincides with the SW – NE striking deeper-seated faults which are located 70 ms (TWT) below the shallow fault. Studying the location of the deeper lying hydrocarbon reservoirs, it appears that there might be a relationship between the AA10 in this area, the pipe structure, and both the shallow and deeper-seated fault. Fig 4.19 shows a variance map at 740 ms (TWT) and 1170 ms (TWT), showing the strike and orientation of both faults along with the location of the hydrocarbon reservoirs. Both the deeper-seated fault and the shallow fault share the same strike and orientation, in map view, and the northwest trend of the reservoir follows the strike of the faults laterally.

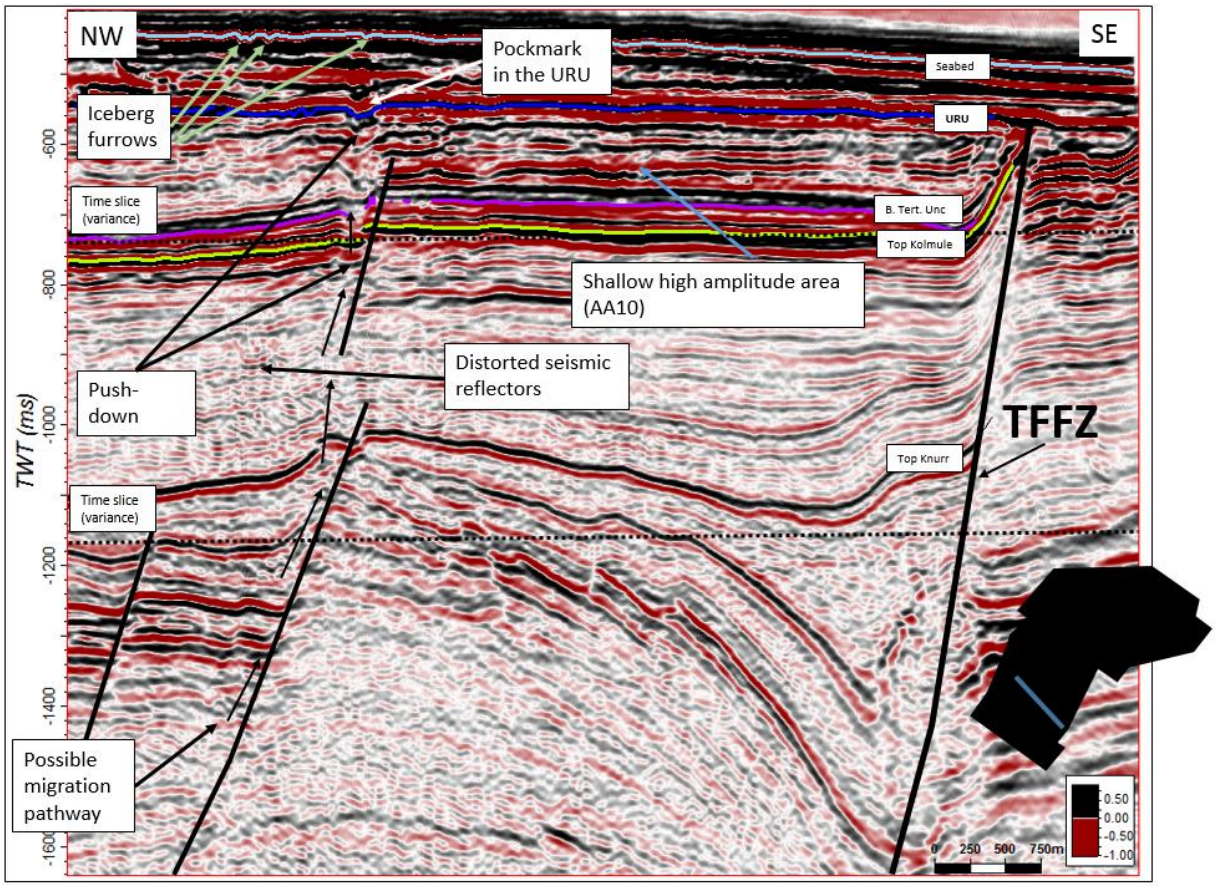

Figure 4.18 *Possible fluid flow along a deeper-seated Jurassic – Permian fault connected to a fault bisecting the Top Kolmule/Kviting and BTU reflectors. Pushdown of the reflectors in front of the fault plane indicates leakage to shallower stratigraphy. A paleo-pockmark in the URU increases the likeliness of a fluid flow system. The shallow high amplitude area indicated is the AA10. Possible migration pathways are indicated with black arrows. Location of profile line is indicated in the black EN0702 survey polygon.*

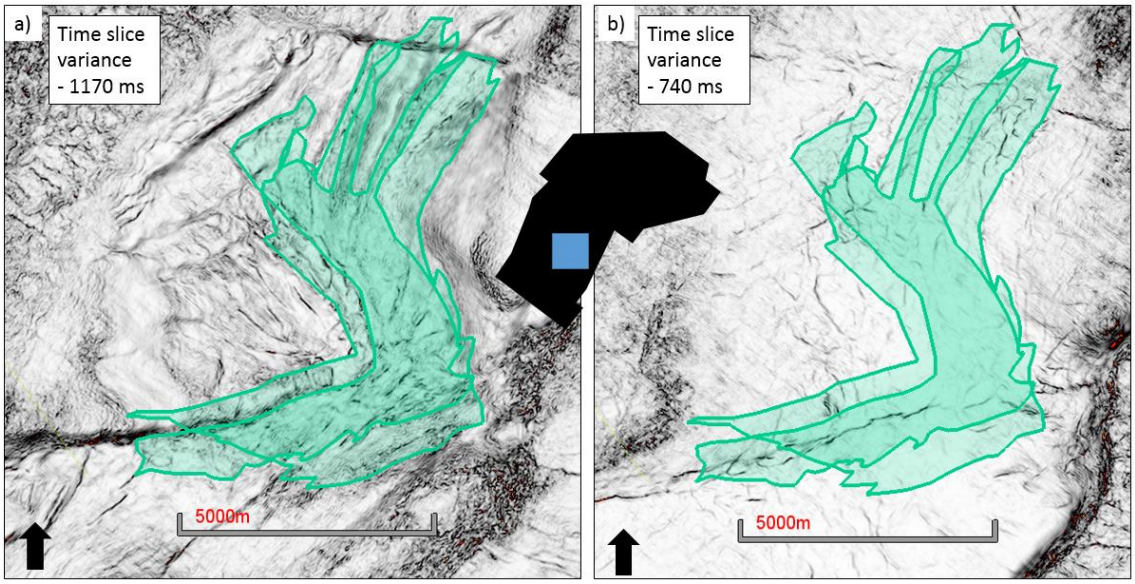

Figure 4.19 *The green polygons indicates the geometry and location of the deep-seated hydrocarbon reservoirs in the Goliat structure. The different variance time slice maps indicates the relationship between the strike of the deeper seated faults and the shallow faults, and how their strike coincides with the lower axis of the reservoir. Location of area is indicated in the black EN0702 survey polygon.*

In the dataset, the method of processing the seismic with focus on deeper lying stratigraphy has made it difficult to extract information from attribute maps focusing on shallow stratigraphy. Especially the northern parts of the survey show areas with particularly high amplitudes, which from interpretation is unrelated to any gas accumulations or specific gas-related features. Because of this, some features are only seen on the seismic profiles, and not on the attribute maps. Additionally the coherent noise from the seismic survey becomes particularly prominent on the RMS maps.

The fluid pipe structure in Fig 4.20 is an example of a fluid flow structure unrelated to amplitude anomalies or faults. The structure is located approximately 6050 meter NW of AA1, and has a vertical length of 525 ms (TWT), and is thus traceable from the seabed, through the Torsk Formation, BTU and down into the Kolmule formation. The structure is not visible on the RMS or Max amplitude maps, but from the min curvature map, a single N – S oriented fault situated in the upper Kolmule and Torsk formation is visible. Pushdown and acoustic turbidity is found along the pipe structure in both the Torsk Formation and in the Nordland Group.

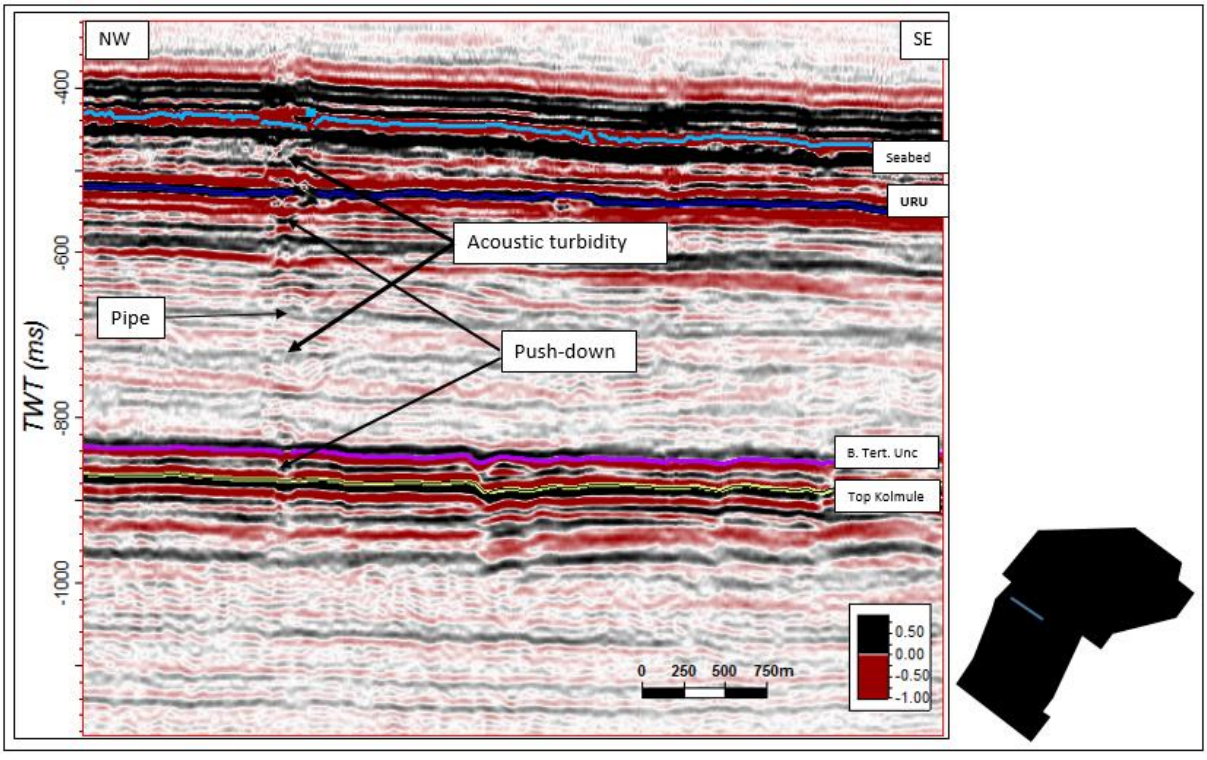

Figure 4.20 *Seismic profile line showing a pipe structure unrelated to fluid flow features seen on the attribute maps*

4.4 Shallow gas accumulations and fluid migration

The presence of gas in shallow sediments from the Pliocene – Pleistocene may be a result of leakage from deeper-seated prospective reservoirs (Andreassen et al., 2007a). The free gas lowers the sediments coherency and shear strength, which in turn represents a potential threat and hazard for the exploration industry in the search for hydrocarbons. In the EN0702 dataset, the shallow amplitude anomalies seemed to be confined mainly to the Torsk Formation, and earlier studies (e.g. Chand et al. (2009)) have interpreted these anomalies to represent shallow gas accumulations and hydrocarbon anomalies.

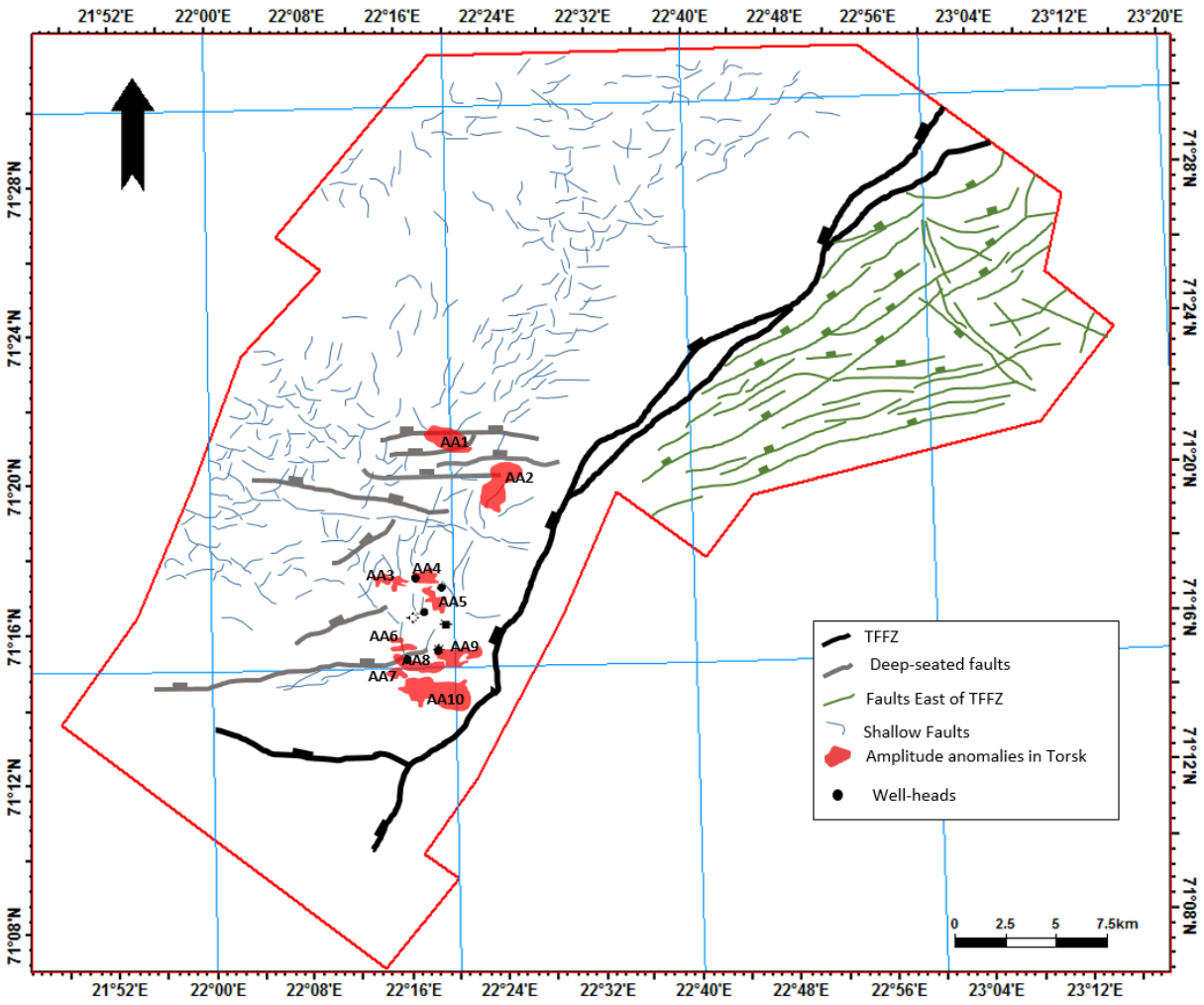

Figure 4.21 *Schematic overview of some of the structural elements and the amplitude anomalies presented in the following chapters. The green faults to the east of the TFFZ are not considered in this study.*

4.5 Amplitude Anomalies within the Torsk Formation

Amplitude anomalies are common throughout the Hammerfest Basin, and within the study area, the focus is towards any anomaly above the BCU. Deeper anomalies are omitted completely from this study. The amplitude anomalies in the EN0702 survey area show the highest concentration over the Goliat structure, above the deeper-seated hydrocarbon reservoirs. In this study, a selection of the different anomalies are presented and described based on data from the seismic profiles and attribute maps.

In this chapter, I will go into detail and describe all of the mapped amplitude anomalies. The descriptions will focus on size, distribution and the time window they affect. If there are any faults in the near vicinity or in relation to the anomaly, these will also be described, and if there is any relation to deeper-seated faults. At the end of the chapter, I will present a short summary off all the observations, and tables to give a better overview of each of the amplitude anomalies.

4.5.1 Amplitude anomaly 1

The amplitude anomaly 1 (AA1) is located in the central parts of the EN0702 Survey, in the central areas of the EN0702 survey. (Fig. 4.21 and fig. 4.22). On seismic profiles, the top of the anomaly is located 27 ms (TWT), approximately 27m (TVD) (Vp = 2000 m/s) below the URU/Top Torsk surface. The amplitude anomaly occurs in a 137 ms (TWT) window, traceable only in the Torsk Formation. In plain view the anomaly covers an area of roughly 4,8 km^2 with an elongated shape oriented in a NW - SE direction. The longest axis measures 3070 meters and the short axis 1577 meters respectively. On the seismic profiles, the anomaly is recognized by two strong reflectors in the upper section with distorted reflectors beneath where acoustic masking and transparency of the seismic occur. The top of the anomaly is laterally horizontal and follows the URU and not the dipping clinoforms within the Torsk Formation. The base of the anomaly shows an abrupt transition downwards to the Top Kolmule horizon, where the reflectors appear undisturbed. AA1 lies above an array of polygonal faults in the Lower Kolmule Formation. Below the polygonal faults, at least two deep-seated faults, penetrating the Jurassic have upper fault tips coinciding with the BCU/Top Knurr horizon. It is possible that the faults bisect the BCU, but this is inconclusive from the seismic profile.

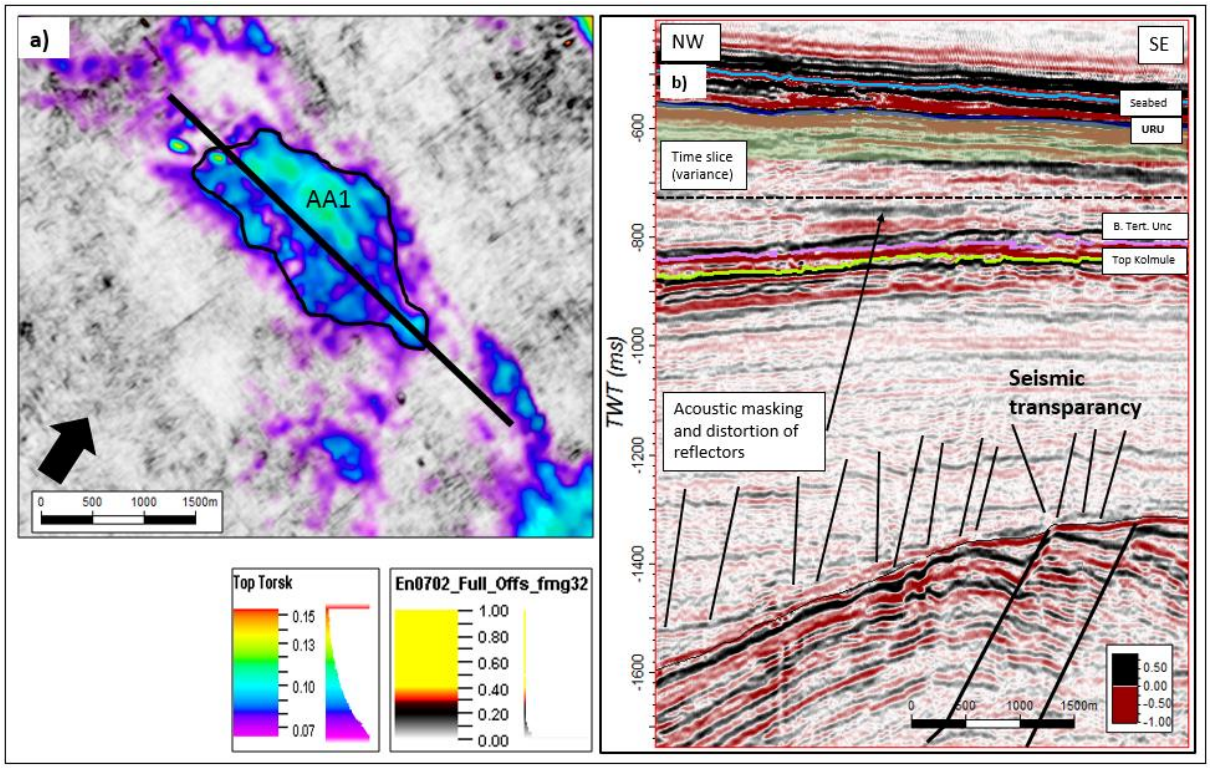

Figure 4.22 a) *overview of amplitude anomaly one (AA1) from a RMS map over a Variance time slice map (720 ms (TWT). The RMS amplitude is extracted from the Top Torsk horizon in a 70 ms (TWT) window below the horizon as indicated (green transparent zone in **b**). Position of AA1 is marked in Fig. 4.21 **b)** Seismic section through AA1. Profile line is indicated in **a)**. The anomaly is recognized as a laterally long and strong reflection with acoustic masking and distorted reflectors underneath.*

4.5.2 Amplitude anomaly 2

Amplitude Anomaly 2 (AA2) is located 2 km Southeast of AA1 (Fig 4.21 and Fig 4.23). It occurs within a 130 ms (TWT) window from the URU, visible only within the Torsk Formation, but as the URU coincides with the seabed reflector. The AA2 is located in an area where the stratigraphic units are shallowing upwards in a Northeast direction. AA2 covers an area of approximately 4 km^2 and the top of the anomaly is 16 ms (TWT) below the URU/Top Torsk surface. The Anomaly coincides with an area where the seabed has been eroded down to the URU. Three shallow faults affecting the Kolmule Formation and the Torsk Formation lie over two NW – SE deeper-seated faults, which penetrate the Jurassic strata and up through the BCU in to the Kolmule Formation. The top of the anomaly can be seen on the seismic profiles from 587 ms (TWT), and the base of the anomaly occurs at 717 ms (TWT). It is possible that the anomaly lies deeper than what is seen on the variance attribute maps and the seismic profiles, as the reflectors are particularly transparent in this area of the survey. Beneath the anomaly,

two shallow faults with E – W strike seems to channelize the acoustic masking, with possible "pull-up" of the reflectors just below the Top Kolmule/Kviting horizon.

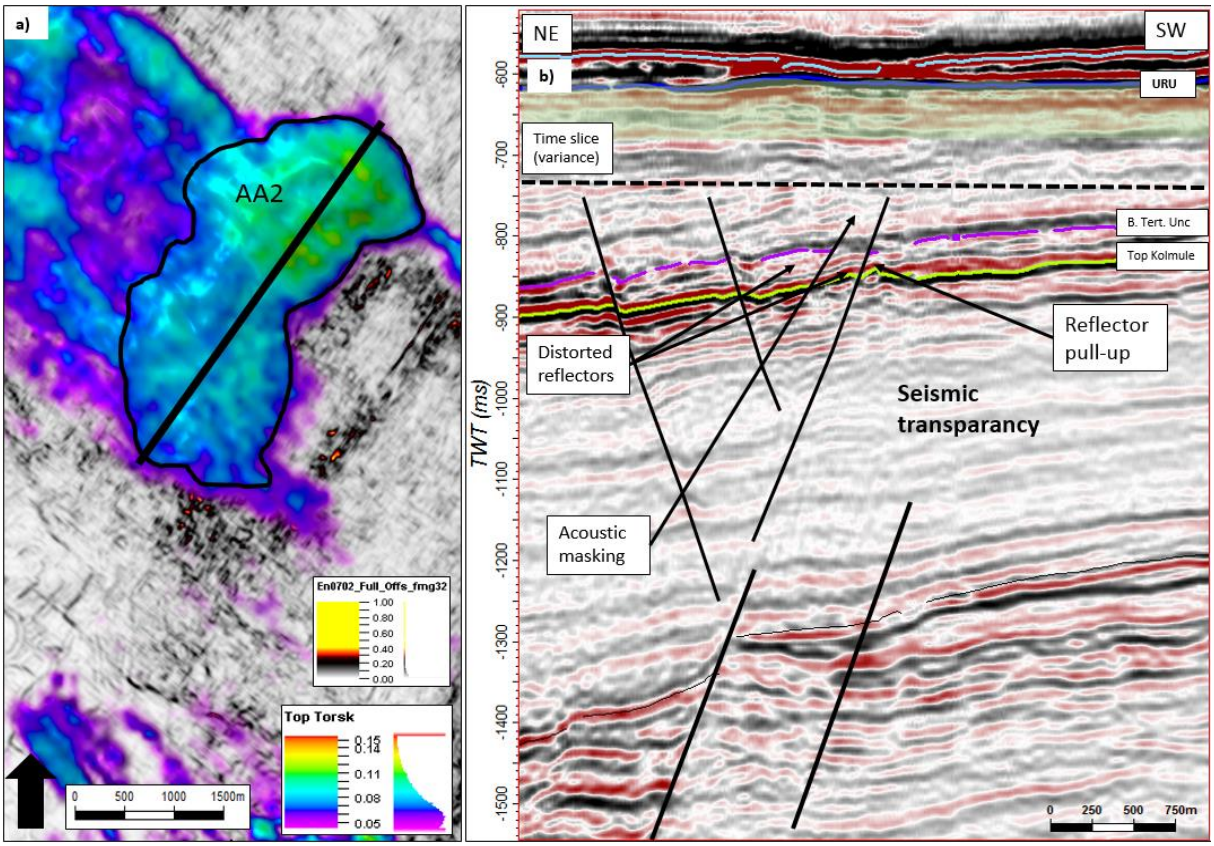

Figure 4.23 a) *Overview of the amplitude anomaly 2, AA2. RMS map extracted from a 70 ms (TWT) window (green transparent colour in b), over a variance time slice at 720 ms (TWT). The location of AA2 is indicated on Fig. 4.21* ***b)*** *seismic section through AA22. The position of the profile line is indicated in* ***a****). Two deep seated NW- SE striking faults is situated under two shallow E – W striking faults.*

4.5.3 Amplitude anomaly 3

Amplitude anomaly 3 (AA3) is located approximately 6 km south – southwest of AA2 (Fig 4.21 and Fig. 4.24). The anomaly is traceable to the Nordland group below the seafloor and occurs in a 118 ms (TWT) window from the seafloor and downwards. It does not appear to affect the reflectors below the BTU. Time slices from the variance attribute reveals three deep-seated faults and a system of shallower faults in the Kolmule and Torsk Formations. The deep-seated fault to the SE has a NW – SE strike while the two faults to the NW have a NE – SW strike. The shallow faults in the Kolmule formation have an N – S and NW – SE strike. The highest amplitude occurs between the two faults tilting in opposite direction of each other. The long axis of the AA3 stretches 1527 m in the NW – SE direction and the short axis extends approx. 595 m in a SW – NE direction. The anomaly covers an area of roughly 0,9 km^2, with

the top anomaly visible on the seismic profiles from less than 10 ms (TWT) below the Seafloor, and under the anomaly the seismic reflectors are particularly transparent.

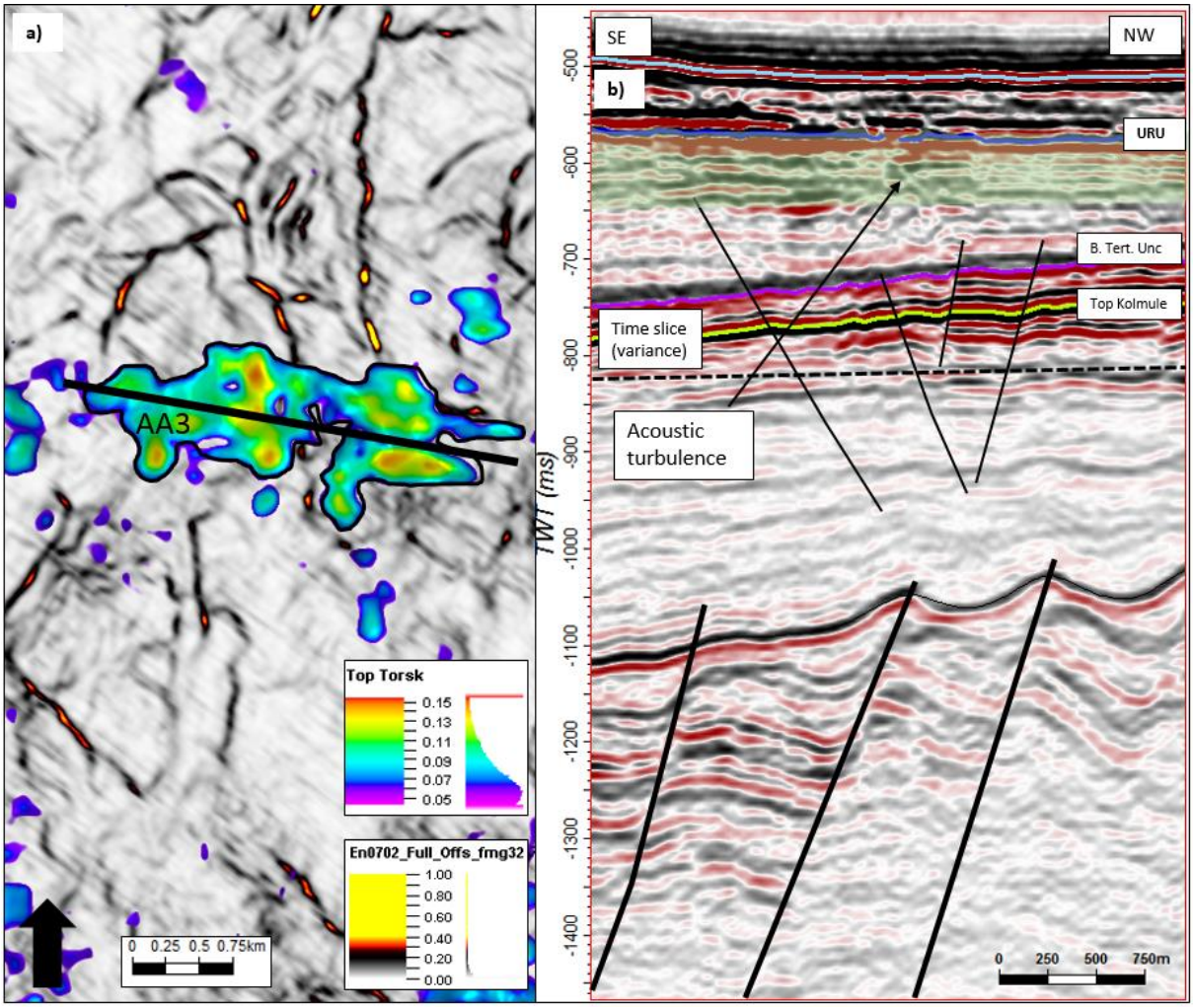

Figure 4.24 a) *Overview of the amplitude anomaly 3, AA3 . The RMS amplitude is extracted from a 70 ms window from the Top Torsk horizon (green transparent zone in b), over a variance time slice at 820 ms (TWT). The location of AA3 is indicated on Fig 4.21* ***b)*** *Seismic section through AA3. The position of the profile line is indicated in* ***a****). Three deep-seated faults with NW – SE and NE – SW strikes respectively lie underneath an array of shallow faults with NE – SW strike.*

4.5.4 Amplitude Anomaly 4

Amplitude anomaly 4 (AA4) is located 500 meters east of AA3 (Fig. 4.21 and Fig. 4.25). The amplitude anomaly occurs within a 37 ms (TWT) window, with the top of the anomaly at 626 ms (TWT), 50 ms (TWT) below the URU, and the base of the anomaly lies just above the BTU, at 663 ms (TWT). The AA4 covers an area of approximately 0,7 km^2. An array of N – S to NE – SW striking faults in the Kolmule and Torsk formations are seen close to the anomaly, and two deeper-seated faults, also with strikes in a NE - SW direction lies beneath the fault array. These faults penetrate the Jurassic strata, and show signs of local inversion directly at the upper

fault tips. They share the same NE – SW strike. The high amplitude reflectors are semi-horizontal and are located directly on top of a shallow fault that might be connected to the deep-seated fault located vertically directly underneath the anomaly. The anomaly is traceable only within the Torsk Formation.

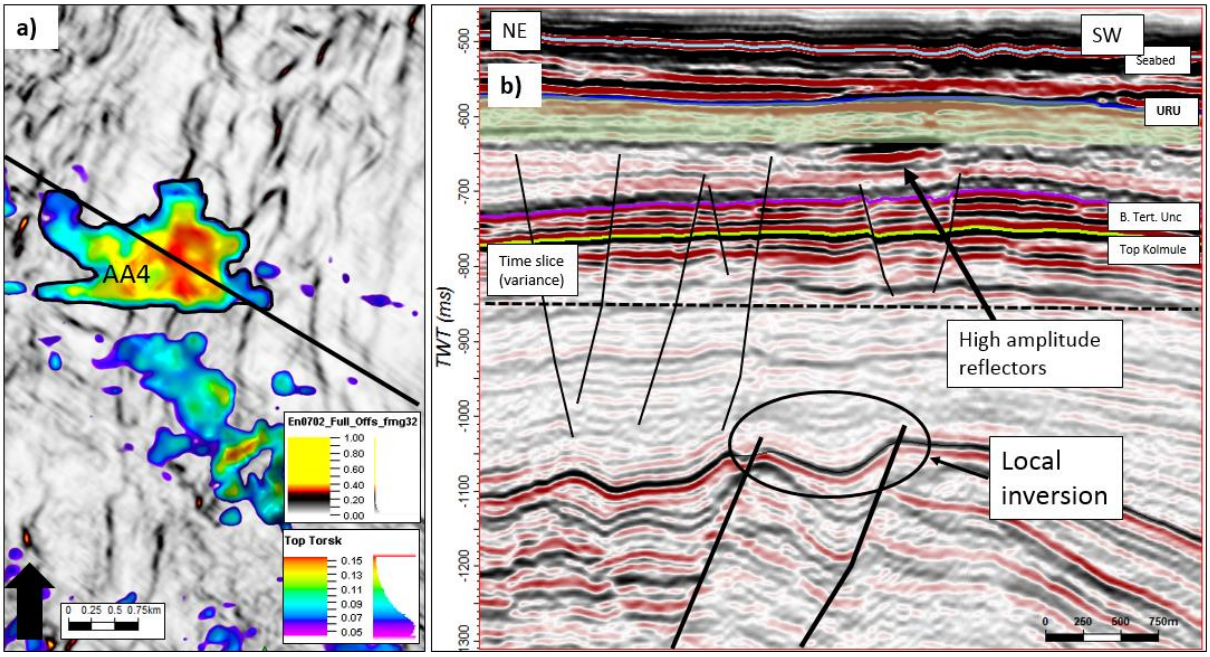

***Figure 4.25 a**) Overview of the amplitude anomaly 4, AA4. The RMS amplitude is extracted from a 50ms (TWT) window below the Top Torsk horizon (green transparent zone in **b**), over a variance time slice at 840 ms (TWT). The location of AA4 is indicated on Fig. 4.21 **b)** Seismic section through AA4. The profile line is indicated in **a)**. Two deep-seated faults with NE – SW strike lies under an array of shallow faults with similar strike in the Kolmule formation. Possibly local inversion is located on the fault tips of the deep-seated faults*

4.5.5 Amplitude anomaly 5

Amplitude Anomaly 5 (AA5) is located 200 meters south of AA4 (Fig. 4.21 and Fig 4.26), and appears as an elongated shape with the longest axis in the NE – SW direction. The top of the anomaly coincides with the URU at 536 ms (TWT) and is traceable down to 687 ms (TWT) where it coincides with the BTU, covering a window of approximately 150 ms (TWT). The reflectors show a high grade of distortion with acoustic turbidity, and it affects both the Torsk Formation and the overlying Nordland Group. The AA5 covers an area of roughly 0,4 km^2. An array of four shallow faults affecting the Kolmule formation and the Torsk formation boarders the anomaly in the East and West direction. It is not observed any acoustic masking under the enhanced reflectors. The Upper Kolmule faults have an N – S strike, same as the underlying Jurassic – Permian faults.

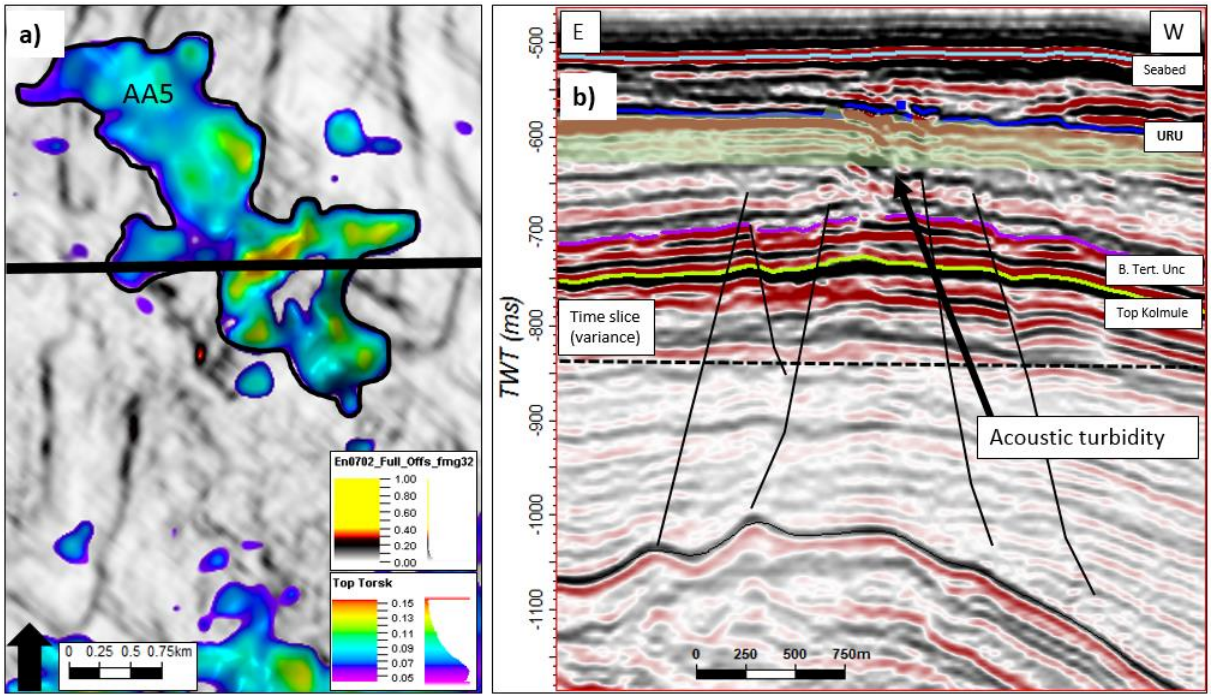

Figure 4.26 a) *Overview of amplitude anomaly 5, AA5. The RMS amplitude is extracted from a 50 ms (TWT) window below the Top Torsk horizon (green transparent zone in* ***b****). The RMS lies over a variance time slice from 840 ms (TWT). The location of AA5 is indicated in Fig 4.21* ***b)*** *Seismic section through AA5, with at least four N – S striking shallow faults within the Kolmule formation. Distorted reflectors in the middle of the four faults*.

4.5.6 Amplitude Anomaly 6

Amplitude Anomaly 6 (AA6) is located 2,2 km southwest of AA5 (Fig. 4.21 and Fig 4.27). In map view, the AA6 resembles what seems to be two separate anomalies, but from the seismic profiles, they are interpreted as one. The AA6 has an elongated shape in the W – E direction, and the strongest reflectors occur in a narrow vertical pipe-like structure. The pipe structure stretches approximately 254 ms (TWT) in the vertical direction from the Nordland Group and down to the Kolmule/Kviting horizon. The anomaly is located just 15 ms below the seabed reflector. The top of the anomaly is visible from 510 ms (TWT) and the base occurs at 650 ms (TWT). There are strong reflectors under the pipe structure in the Kolmule formation, and below these, there appears to be acoustic masking and turbidity disturbing the reflectors. The amplitude anomaly covers an area of roughly 0,6 km^2. The reflectors show higher continuity on each side of the pipe-structure within the Torsk Formation, and thus the highest distortion of the reflectors are within the pipe structure itself. The anomaly occurs in both The Nordland Group and in the Torsk Formation.

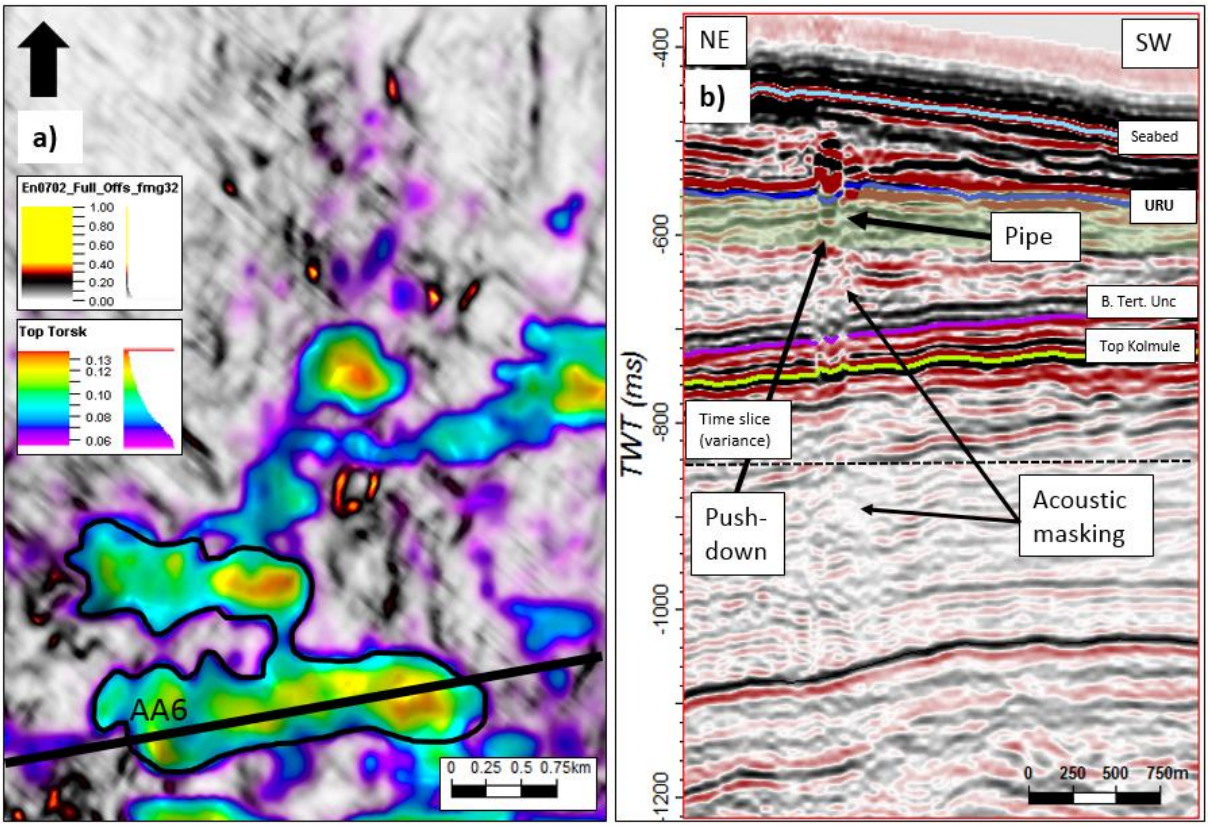

Figure 4.27 a) *Overview of the amplitude anomaly 6, AA6. The RMS map is extracted from 70 ms (TWT) from the Top Torsk horizon (green transparent zone in* ***b****), over a variance time slice at 840 ms (TWT). The location of AA6 is indicated on Fig 4.21* ***b)*** *Seismic section trough AA6, no deeper-seated fault is recognized under the anomaly, nor any shallow intra-Kolmule faults.*

4.5.7 Amplitude Anomaly 7

Amplitude Anomaly 7 (AA7) is located 780 meters south of AA6 (Fig. 4.21 and Fig 4.28). The anomaly has an elongated shape with the longest axis in a W – E direction, similar to AA6. The anomaly occurs within a 143 ms (TWT) window, stretching from 22 ms (TWT) below the seabed reflector and bisecting both the Torsk and BTU and downwards to the Top Kolmule/Kviting horizon. The longest axis of the anomaly is 1028 m and the short N – S axis measures 357 m. The AA7 covers an area of 0,3 km^2 and is the smallest of all the anomalies. Two shallow faults penetrating the Kolmule and Torsk Formations lie adjacent (Fig 4.28a) to the area with the strongest distortion of the reflectors. Both faults seem to reach the anomaly, but the eastern most of the two seems to limit the anomaly to the west in the Kolmule formation. Directly below the anomaly, where it is at it's thinnest, there seems to be some acoustic masking with pushdown on some of the reflectors. The anomaly occurs in the Nordland Group, Torsk Formation and bisects the BTU reflector.

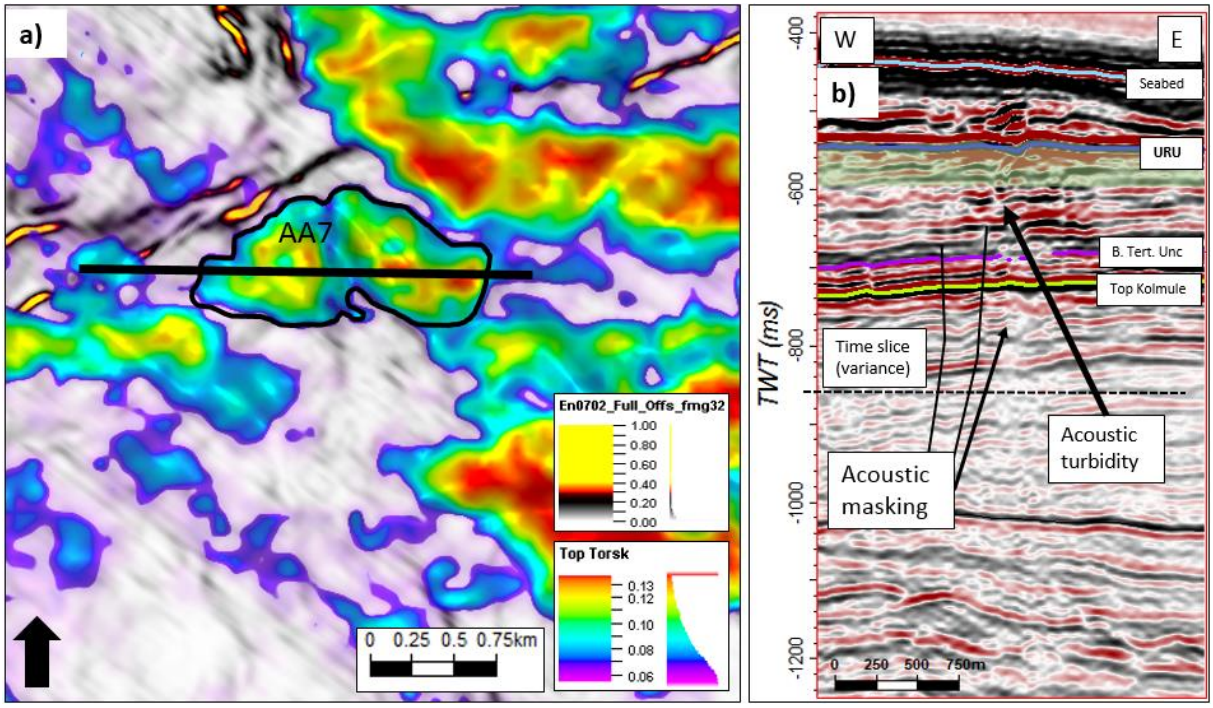

Figure 4.28 a) *Overview of amplitude anomaly 7, AA7. The RMS map is extracted from a 50 ms (TWT) window below the Top Torsk horizon (green transparent zone in **b**). The RMS extraction in a) lies over a variance time slice at 840 ms (TWT). The location of AA7 is indicated in Fig 4.21* ***b)*** *Seismic section through AA7. Distorted reflectors and pipe stricter with no immediate relation to any underlying fault(s).*

4.5.8 Amplitude Anomaly 8

Amplitude Anomaly 8 (AA8) is located just 100 meters north of AA7 (Fig. 4.21 and Fig 4.29). In map view, it has a meandering shape with the eastern delimitation curving upwards in a northwest direction. The long axis including the curve is 2667 meters in the E – W and northwest direction, and the shortest axis in the N – S direction is 327 meters. AA8 covers an area of roughly 0.81 km^2. The anomaly is traceable down to the BTU reflector and occurs within a 191 ms (TWT) window. The top of the AA8 is visible from 20 ms (TWT) below the seabed, at a TWT of 450 ms, and the base of the anomaly at the BTU reflector occurs at 641 ms (TWT). The reflectors appear chaotic within the upper Nordland Group and Torsk Formation, but below in the Kolmule formation the reflectors are more transparent and influenced by acoustic masking and turbidity. The pipe structure is 232 ms (TWT) in the vertical direction, and the narrow feature is traceable down to the Top Kolmule reflector. Directly under the pipe structure, a deep-seated Jurassic – Permian fault is located (Fig. 4.29c), crossing the anomaly from below. The deep-seated fault has a NE – SW strike and the reflectors above the fault tip show a slight increase in amplitude turbidity to the left of the fault (Fig 4.29b). AA8 occurs in both the Nordland Group and the Torsk Formation.

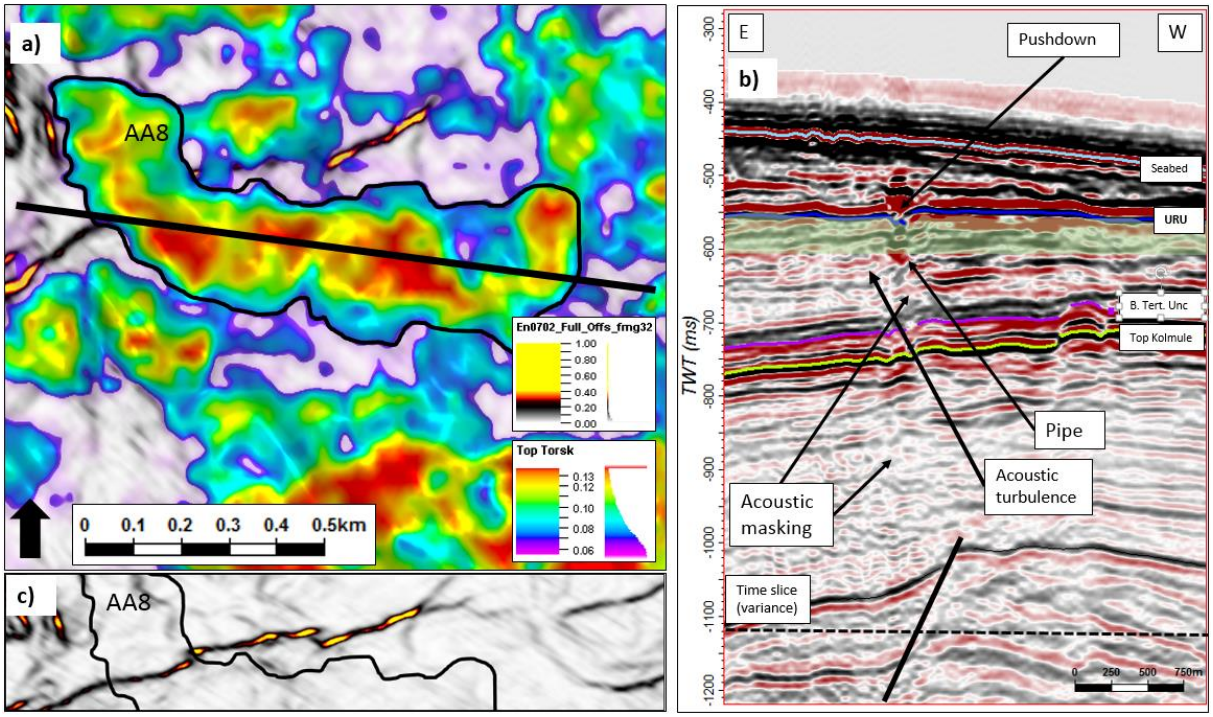

Figure 4.29 a) *Overview of amplitude anomaly 8, AA8. The RMS map is extracted from a 50 ms (TWT) window (green transparent zone in **b**). The RMS extraction lies over a variance time slice at 1120 ms (TWT). The position of AA8 is indicated in Fig 4.21. **b)**. Seismic section through AA8. The seismic profile line is located in **a)**. A deep-seated SW – NE striking fault lies underneath the anomaly (indicated in **c**). The pipe structure penetrates the Kolmule/Kviting and BTU horizons and the reflectors within the Kolmule Formation is highly distorted. **c)** Variance time slice at 1120 ms (TWT) with outline of AA8 to indicate the deep-seated SW – NE striking fault.*

4.5.9 Amplitude Anomaly 9

Amplitude Anomaly 9 (AA9) is located adjacent to AA8 (Fig. 4.21 and Fig 4.30), but from the seismic profiles it has been interpreted as two different features. In map view, AA9 has it's longest axis in an E – W direction and the shortest axis in the N – S direction. The Anomaly has two separate long axis in the eastern delimitation. The longest axis in E – W direction measures 2347 meters and the shortest axis in N – S direction is 814 meters. The top of AA9 is visible from 30 ms (TWT) below the URU at 565 ms (TWT) and the base of the anomaly presumably at 635 ms (TWT). The strongest reflectors occur in the uppermost 50 ms (TWT) of the anomaly, and right below the high amplitudes, the reflectors are strongly distorted and affected by acoustic turbidity. This is also the same area where the anomaly bisects the BTU reflector. Below the AA9, in the Kolmule Formation there is an area with acoustic masking and transparency traceable down to the BCU Top Knurr. The acoustic masking is traceable roughly 290 ms in the vertical direction from the Top Kolmule/Kviting reflector. The anomaly does not occur in the Nordland Group but is traceable in the Torsk Formation and at the BTU reflector.

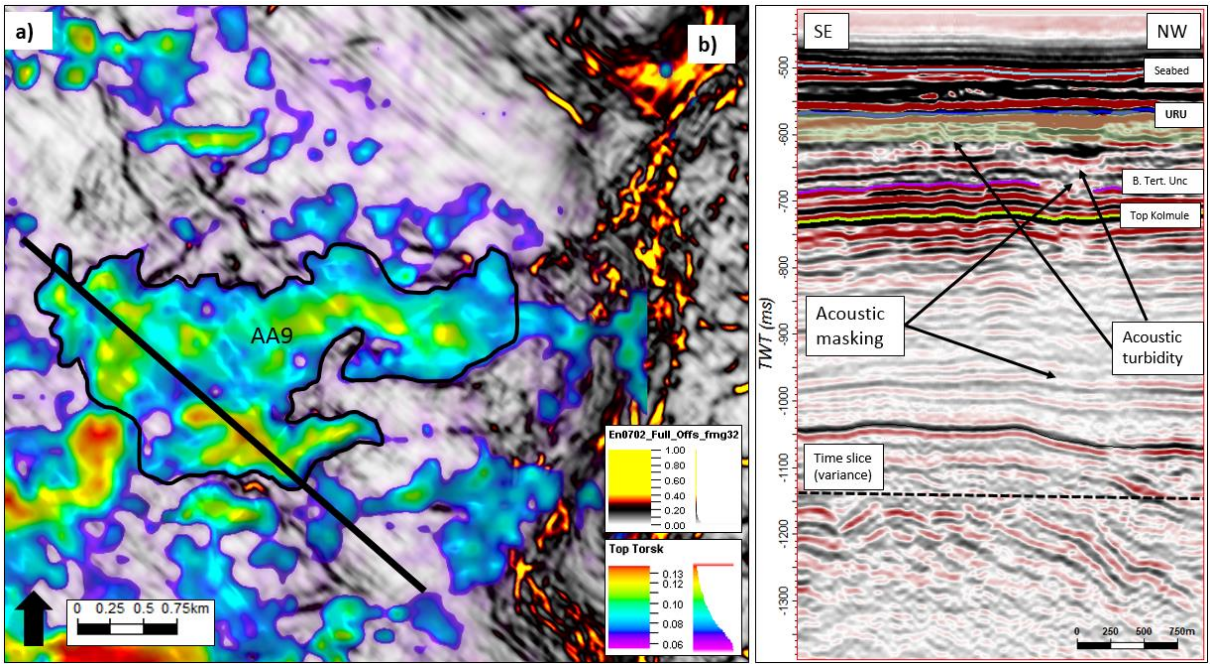

Figure 4.30 a) *Overview of amplitude anomaly 9, AA9. RMS map is extracted from a 50 ms (TWT) window (green transparent zone in* ***b****). The RMS extraction lies over a variance time slice at 1120 ms (TWT). The position of AA9 is indicated in Fig 4.21.* ***b)*** *Seismic section through AA9. The seismic profile line is indicated in a). The anomaly have a long lateral distribution with a vertical masking zone under the anomaly. At the AA9 the reflectors are highly distorted.*

4.5.10 Amplitude Anomaly 10

Amplitude Anomaly 10 (AA10) is located 175 m south of AA8 (Fig. 4.21 and Fig 4.31). In map view, the anomaly has an elongated cigar shape, with longest axis directed towards WNW – SES, and the shortest axis pointing in an N - S direction. The anomaly is 3334 meters long and at the shortest width is 769 meters. In total, it covers an area of 2,25km^2. The anomaly is located between 542 ms (TWT) and 660 ms (TWT), and in the Torsk Formation, the anomaly has a laterally flat shape with strong reflectors. The highest amplitude is visible within the Torsk Formation, where the reflectors are particularly strong. The anomaly seems to only occur in the Torsk Formation. Below the anomaly in the Kolmule Formation, the reflectors are affected by acoustic masking extending vertically downwards in approximately 300 ms. At least three deep-seated faults penetrating the Jurassic strata lies directly beneath the anomaly. Each of them also show signs of local inversion directly at the upper fault tip (Fig 4.31b). The deep-seated faults all share the same NE – SW strike.

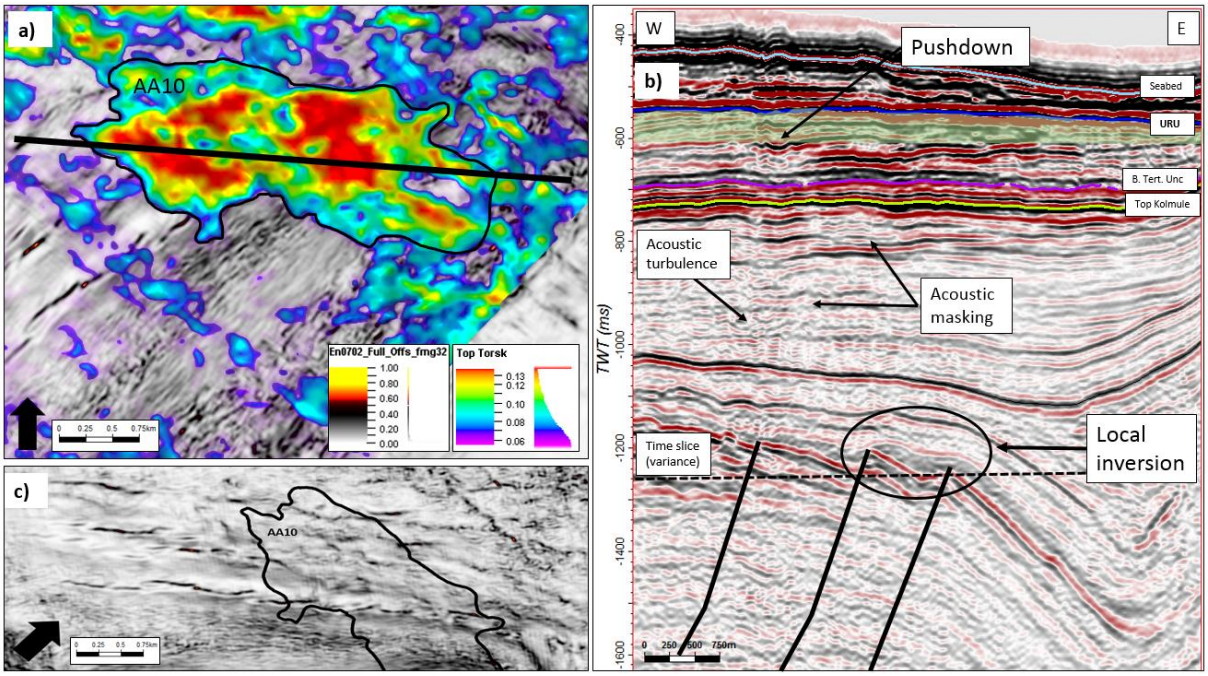

Figure 4.31 a) *Overview of the Amplitude anomaly 10, AA10. The RMS map is extracted from a 50 ms (TWT) window (green transparent zone in* ***b****). The position of AA10 is indicated in Fig. 4.21.* ***b)*** *Seismic section through AA10. The seismic profile line is indicated in* ***a****). Three deep-seated SW – NE striking faults lie directly under the anomaly. Distorted reflectors and acoustic masking is recognized within the Torsk and Kolmule formation. Signs of local inversions over the upper fault tip of the deep-seated faults are indicated in* ***b****).* ***c)*** *A variance time slice at 1120 ms (TWT) showing an overview of the three deep-seated faults and the orientation of the AA10 above the faults.*

4.5.11 Summary of Amplitude Anomalies within the Torsk Formation

After studying the amplitude anomalies, some trends are recognized. They share the same expressions on the seismic RMS maps, and all except AA6 are related to faults somehow (see also table 4.2). The shallowest anomaly, AA7 is visible from 505 ms (TWT) on the seismic section and the deepest anomaly (as in, deepest upper termination) is the AA4, at 626 ms (TWT). The Shallowest base TWT is AA2 at 617 ms, and the deepest base TWT is at 686 ms, at AA5. A summary of the top and base TWT of the different anomalies is presented in table 4.1 including their size and Formation they affect. Table 4.2 gives an overview of the anomalies and the relation to both shallow and deeper-seated faults including their orientation.

Table 4-1 *Overview of the amplitude anomalies 1 – 10, their distribution and covered area, including the stratigraphic intervals they affects and the average top and base TWT they occur in on the seismic profiles.*

Anomaly	Length (m)	Width (m)	Area (km^2)	Formation	Top TWT	Base TWT
AA1	3070	1577	4,8	Nordland, Torsk	520	657
AA2	2930	1370	4,1	Nordland, Torsk	587	617
AA3	1527	595	0,93	Nordland/Torsk	527	645
AA4	1157	612	0,71	Torsk	626	663
AA5	1351	615	0,42	Nordland/Torsk	536	686
AA6	1153	566	0,62	Nordland/Torsk/Kolmule	510	650
AA7	1028	357	0,34	Nordland/Torsk/Kolmule	505	648
AA8	2667	327	0,81	Nordland/Torsk/Kolmule	450	641
AA9	2347	814	1,4	Torsk/Kolmule	565	635
AA10	3334	769	2,2	Torsk	542	660

Table 4-2 *Overview of the amplitude anomalies 1 - 10 and their relation to shallow and deeper-seated faults. The table also includes the different faults strike orientation*

Anomaly	Orientation of Faults within Kolmule/Kviting/Torsk Formations	Orientation of Deeper-seated faults
AA1	NE – SW	E - W
AA2	NE – SW	E - W
AA3	NW - SE, N - S	NE – SW, NW - SE
AA4	NW - SE, N - S	NE – SW
AA5	N - S	N - S
AA6	-	-
AA7	NE - SW	-
AA8	NE – SW	NE – SW
AA9	NE – SW, NW - SE	NE – SW
AA10	NW - SE	NE – SW

4.6 Seafloor observations

Mapping and seismic interpretation of the EN0702 Survey revealed several morphological depressions with circular or sub-circular shapes. They occur both as single features on the seabed, in plough marks made by drifting icebergs or as closely spaced small-scale depressions. From a morphologically point of view, the features are in this study classified into two groups; small scale pockmarks and isolated depressions (IDs). It is also the area where the highest density of smaller pockmarks occurs in Ingøydjupet, and at the Finnmark Platform (Fig. 4.32). The shallower areas show a lower distribution of the circular depressions. However, the depressions in the shallow areas are of much greater size. The circular depressions on the seabed can be observed both as single standing features, and within the glacial features. Small-scale pockmarks in the study area seem to occur more frequently and in greater number within the glacial features, and especially within the highly eroded area with parallel running lineations (Fig. 4.32a, two areas outlined in red south of the large pockmark field). Earlier studies from the same area have concluded that these are pockmarks (e.g. Chand et al. (2008), Chand et al. (2009), Chand et al. (2012) and Ostanin et al. (2013)).

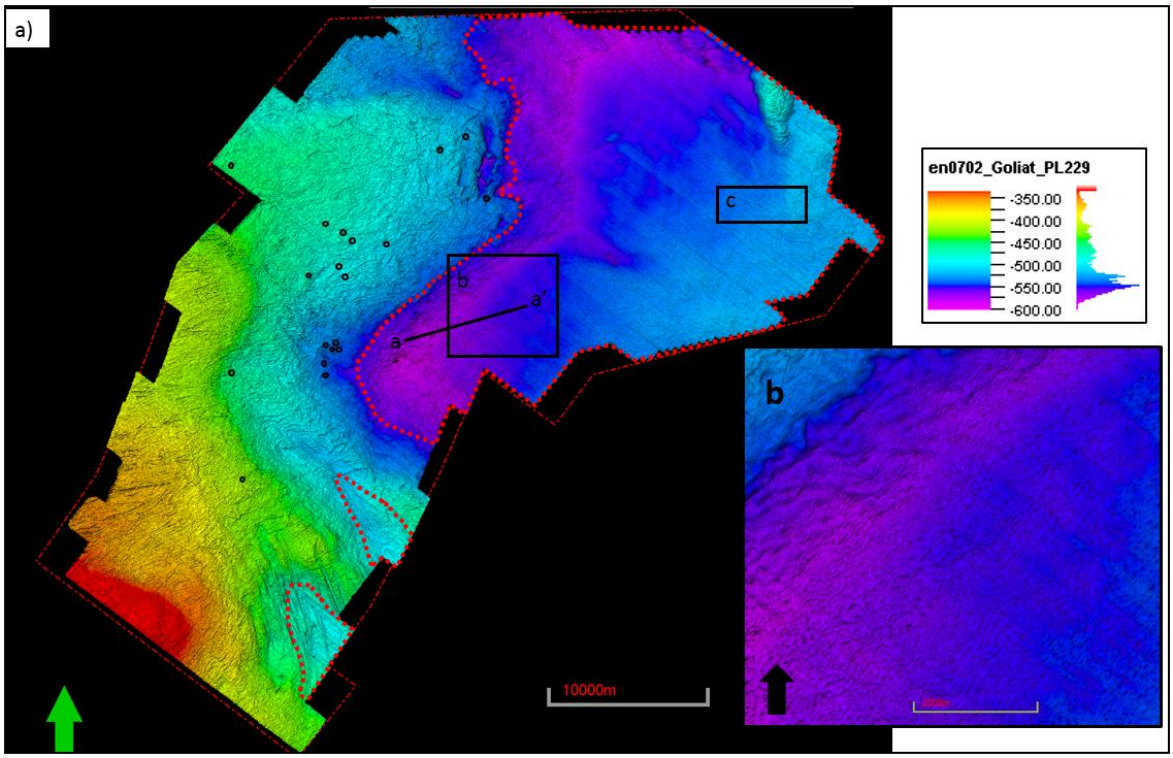

Figure 4.32 a) *Overview of the areas affected by pockmarks (red dotted line). The black circles outlines the areas where mega scale depressions occur, and the red boarder line indicates the areas with high density of pockmarks.* ***b)*** *Close-up of the high-density pockmark area indicated by black box in* ***a)****.*

4.6.1 Small-scale depression and pockmarks

This chapter will focus on the different depressions observed on the seafloor. At the end of the chapter, there will be a short summary including a table to give a better overview of the results.

The high resolution of the seismic data set reveals areas with high density of depressions with a circular to sub-circular shape on the seafloor. The small-scale depressions are interpreted as any feature less than 160 m in diameter. There are more than a thousand of them in this dataset, with some areas having more than 165 pockmarks/km^2, and they seem to be confined to the deeper, low gradient area to the northeast of the study area, Ingøydjupet (Fig. 4.32a). They also appear in high density in the more heavily eroded glacial features and in the area where the glacial sediment layer is at its thinnest. They are closely spaced with some appearing less than 10 meters apart from each other. These depressions or pockmarks vary in size from less than 30 meters in diameter and up to 160 meters, but most of them lie in the interval between 45-55 m. They occur as elongated and circular features with depths from 2 ms (TWT) to 15 ms (TWT) and some occur to be merged in what is called composite pockmarks (Judd and Hovland, 2009). Many of the pockmarks are elongated with their longest axis pointing in a SW – NE direction, and with an asymmetric shape, with one of their front slopes having a gentler dip than the back slope. Some of them have such an elongated shape that it is a bit unclear whether to classify them as pockmarks or as gullies or troughs, but for simplicity reasons, they are all considered pockmarks in this study. Pockmarks may often occur in chains of 5-10 pockmarks or more (Hovland, 1981). It seems that the size of the pockmarks decrease towards the TFFZ and especially the pockmarks left of the escarpment are less prominent on the seismic surface and thus most likely smaller in size. The sediment cover on the Finnmark platform is much thinner than in the basin area, and there seems to be a connection between the thickness of the sediments, and the size of the pockmarks. They occur over areas with both shallow faults, and in the outer rim of the stratigraphy containing polygonal faults. Most of the area outside the platform seems to be devoid of any pockmarks, apart from the ones found in the scour and plough marks made by the glaciers. Within the survey area it is clear that the pockmarks extend

far into the Finnmark platform, and geologically it would be interesting to see how far towards the shore they are distributed.

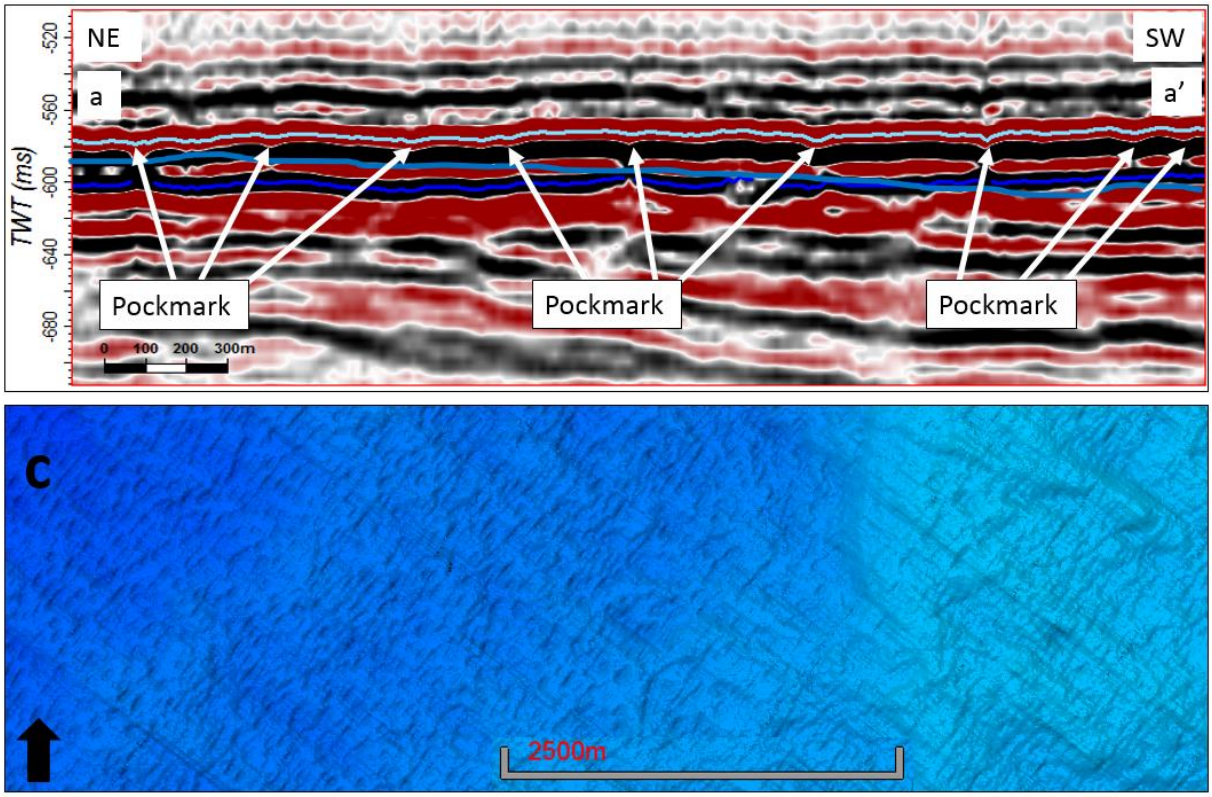

Figure 4.33 *Seismic profile line indicated in Fig. 4.32 a.* ***c)*** *Close-ups of area indicated in Fig 4.32***a**.

4.6.2 Isolated depressions (ID's)

Isolated depressions are in this study defined as any circular to sub-circular feature more than 160 meter in diameter that is not found in the high-density pockmark area but appears as an isolated feature on the seabed. The ID's in this study are not necessarily considered to be pockmarks, as they might be a result of icebergs piercing the seafloor, and not a result of gas seepage or fluid flow, although some of them appear in close correlation to deeper lying fluid flow structures. This seems to be in accordance with previous studies on the crater-like depressions (e.g. Bass and Woodworth-Lynas (1988) and Eden and Eyles (2001)). The ID's vary in size from 160 meter and up 493 meter. Their depth average from 21 ms (TWT) to 25 ms (TWT) corresponding to 15,75 and 18,75 m (TVD) respectively (Vp = 1500 m/s). They occur both in iceberg plough marks and outside of the glacial features. Their shape is commonly circular to sub-circular, while some are elongated with their longest axis up to 493 meter. In the EN0702 survey, more than 20 ID's are visible and interpreted from the seafloor map based on the seabed reflection, and a few of them will be presented in the following chapters. The areas

with highest density of ID's are divided into four different blocks, a southwest (SW) block, western (W) block, north (N) block, and a southern (S) block respectively.

As in chapter 4.5, the following chapter will go into detail on a few of the interpreted isolated depressions with focus on depth, area and geometry, and whether they are related to glacial features or not. At the end of the chapter, there will be a short summary and a table presenting the results in a more straightforwardly way.

4.6.2.1 ID's in the NW of EN0702

The highest density of ID's are found in the northwest of the study area. There seems to be no correlation between furrows, plough marks and the depressions (Fig 4.32b and Fig. 4.34). They are located from less than 115 meters to 2 km apart, and they all share the circular to sub-circular shape. The water depth in the area varies from 550 ms (TWT) to 450 ms (TWT)

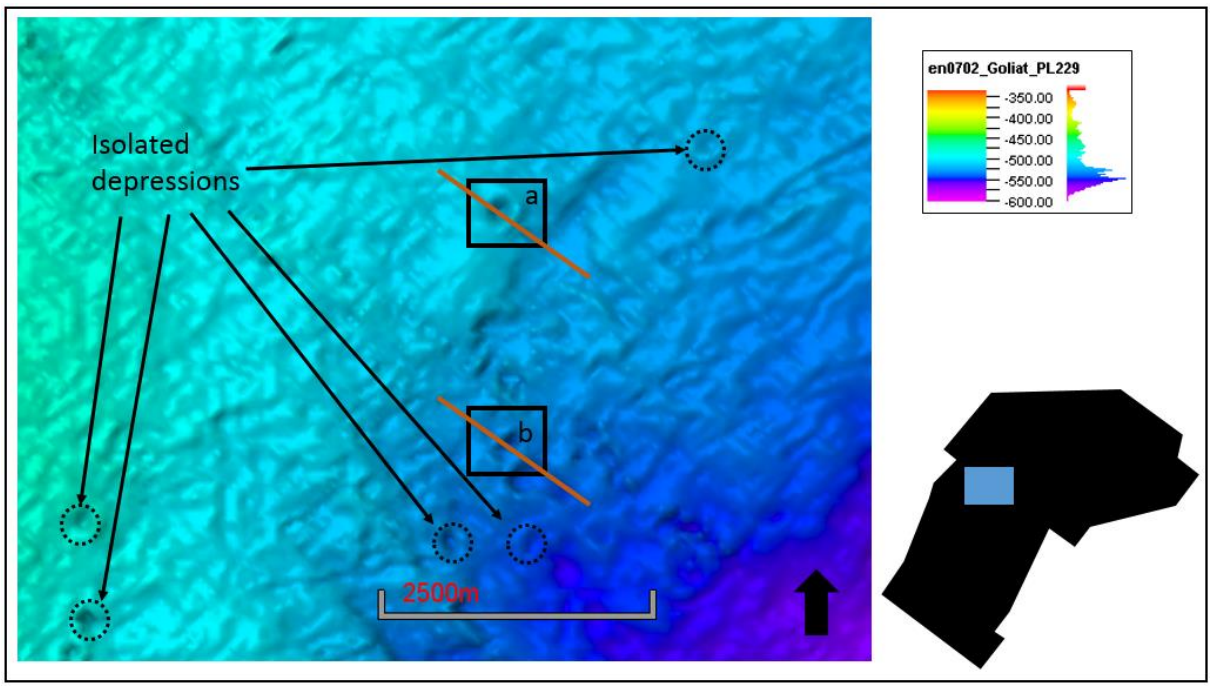

Figure 4.34 *Overview of some of the ID's in the northwestern area of the survey. The area is indicated by the blue box on the survey polygon of the EN0702 to the right.*

4.6.2.2 ID NW1

The NW1 is one of the northernmost of the ID's in the NW area of the study area (Fig 4.34 and 4.35). The long axis measures 287 m, and the short axis is 250 m. This is one of the deepest depressions with a measured depth of 30 ms (TWT). The depression covers an area of 0,22 km^2. The longest axis have a SW – NE strike. The depression does not affect the sediments

below the URU, and the seismic expression terminates at the Top Torsk/URU horizon on the seismic profile (Fig 4.20). The deformation of the reflector is traceable down to 43 ms (TWT) in the Nordland Group, 10 ms (TWT) above the Top Torsk/URU horizon.

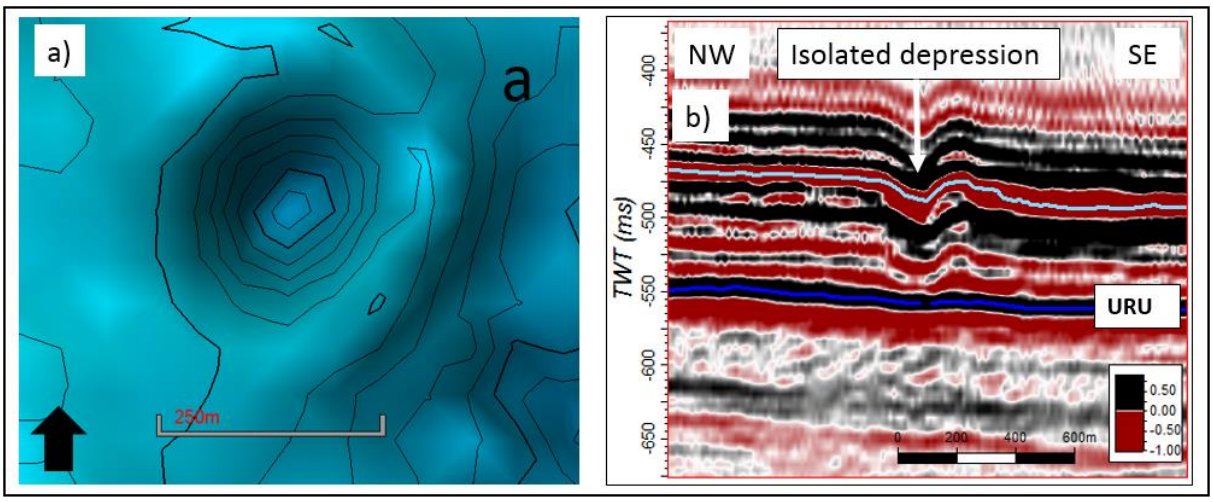

Figure 4.35 a) *close-up of an ID indicated in Fig. 4.27 (box a).* ***b)*** *NW – SE oriented profile crossing the ID, showing the circular to sub-circular shape of the depression.*

4.6.2.3 ID NW2

ID NW2 lies 1858 m SE of ID NW1 (Fig 4.34 and 4.36). The longest axis is 362 m, and the short axis is 220 m. The depth is approximately 22 ms (TWT). The longest axis is oriented in a SW – NE direction, similar to the NW1. The area of the depression is 0,25 km^2 Just like the latter, the depression does not affect any sediments below the Top Torsk/URU horizon, and are confined to the Nordland Group. The discontinuity of the reflector is traceable down to 23 ms (TWT), 10 ms (TWT) above the Top Torsk/URU horizon on the seismic profile.

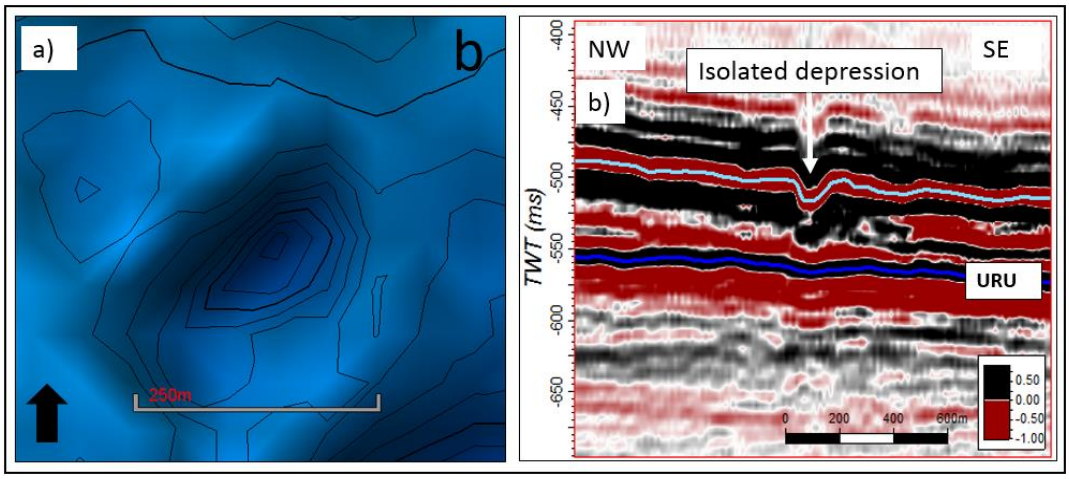

Figure 4.36 a) *Close-up of ID indicated in Fig. 4.34 (box b).* ***b)*** *Seismic profile line oriented NW – SE over the depression.*

4.6.2.4 ID's in the west of EN0702

The depressions in this area seem to appear a long a linear line with a SW – NE orientation (Fig 4.37). Most of them are located in water depths between 500 ms (TWT) and 450 ms (TWT), roughly 1 km from the NW block. The sediment cover (depth down to the Top Torsk/URU) is greater here compared to the NW block. The depression does not appear to show any immediate relationship to glacial features, but it should not be ruled out.

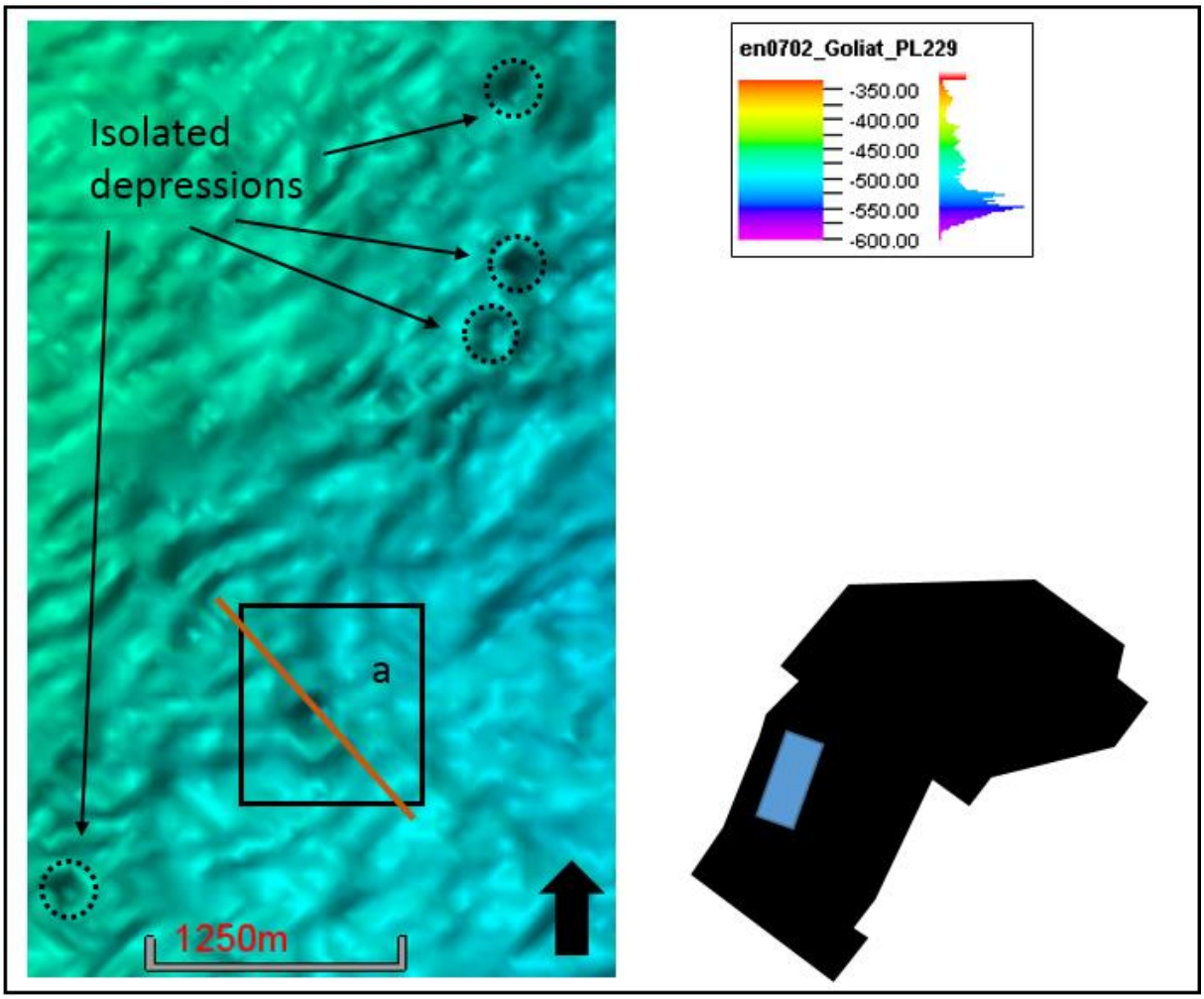

Figure 4.37 *Overview of some of the ID's in the western area of the survey. The location of the area is indicated in the blue box on the black EN0702 polygon.*

4.6.2.5 ID W1

ID W1 is located in the southern parts of the western block (Fig 4.37 and 4.38). The longest axis is 300 m and the shortest axis is 236 m. The longest axis is oriented in a N – S direction. The depth of the W1 is 28 ms (TWT) and it covers an area of 0,21 km^2. The seismic deformation is traceable down to 60 ms (TWT), 22 ms (TWT) above the Top Torsk/URO horizon on the seismic profile, and thus only affects the Nordland Group.

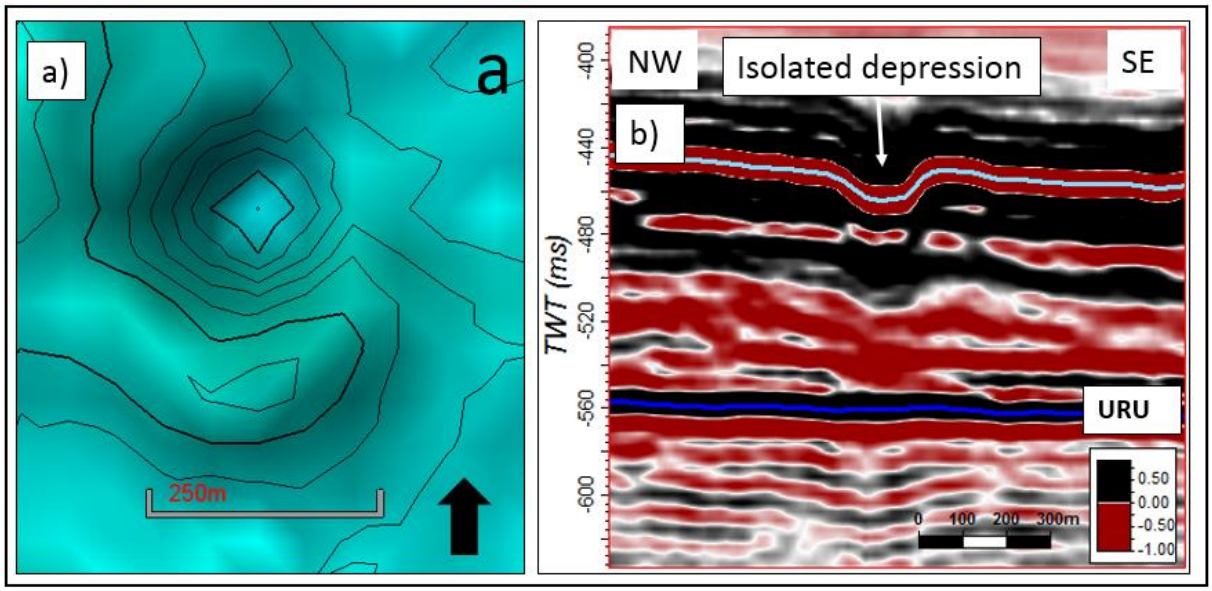

Figure 4.38 a) *Close-up of one of the ID's indicated in Fig. 4.37.* ***b)*** *Profile line crossing the ID in* ***a)*** *in a NW – SE direction. The location of the profile line is indicated on Fig 4.37.*

4.6.2.6 ID's in the Central area of EN0702

The depressions in the Central block are located 3 km from the western block. The depressions here are closely spaced, between 300 and 25 meter. The water depth in this area is between 525 and 550 ms (TWT). The Nordland Group is 65 ms (TWT) in this area. There are no observed fluid leakage structures in the near vicinity of these depressions. The depression have no visible relationship to any glacial erosional features, as can be observed from the seabed reflector.

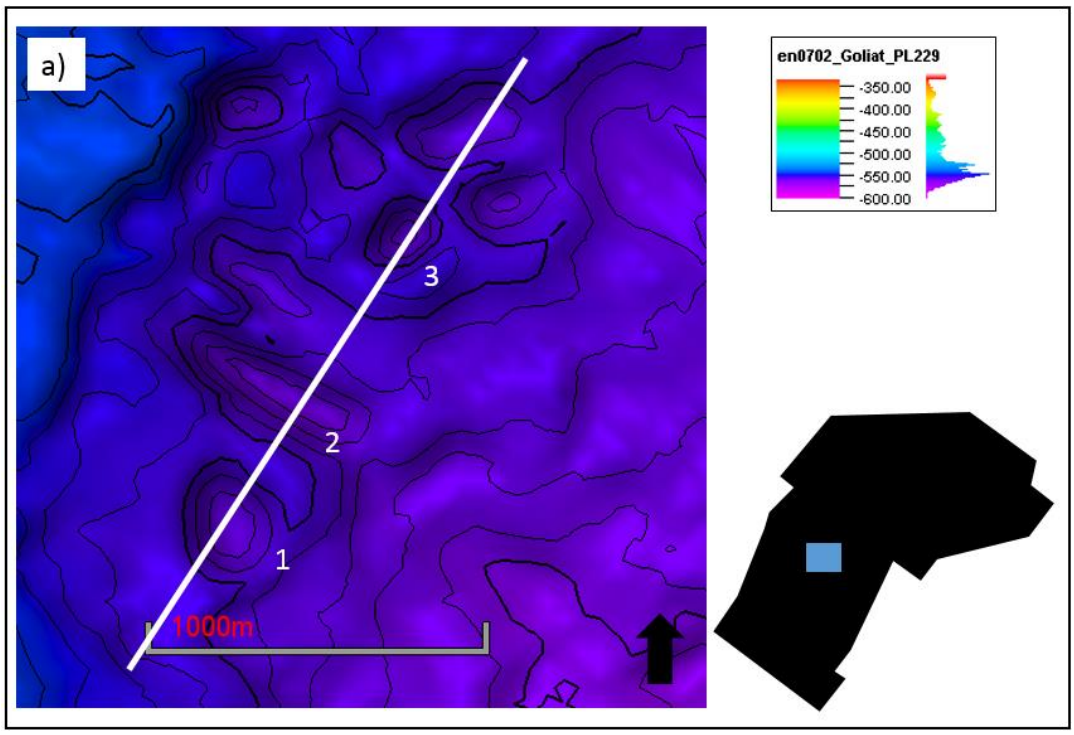

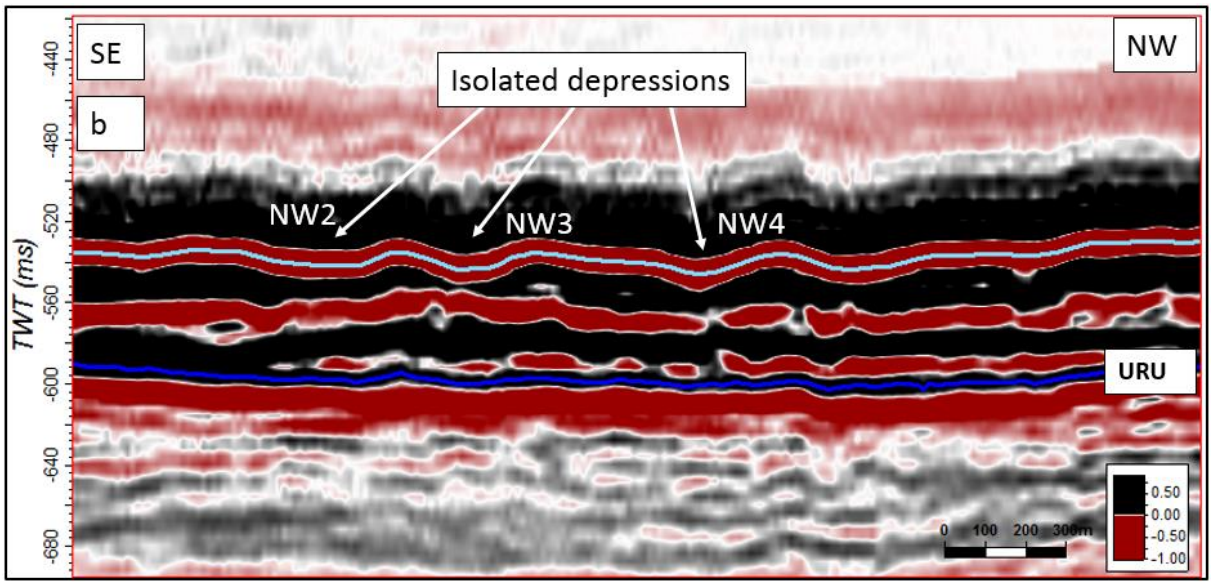

Figure 4.39 a) *Close-up of three ID's situated linearly in map view in the central parts of the survey. Their location is indicated on the black EN0702 survey polygon.* ***b)*** *Seismic profile line crosscutting the three ID's indicated in* ***a)****. The location of the profile line is shown in* ***a)****.*

4.6.2.7 ID C1, C2 and C3

The ID's C1, C2 and C3 are closely spaced, with 100 and 350 meters between them respectively (Fig. 4.39). C1 has a length of 283 m, and sub-circular shape. The depth is 21 ms (TWT), corresponding to 15,75 m (TVD) (Vp = 1500 m/s), The deformation of the seismic reflection is traceable only 13 ms (TWT) down in the Nordland Group. The C2 is located 100 m NE of C1 and has a more elongated shape with the longest axis oriented in a NW – SE direction. The longest axis measures 493 m and the short axis is 207 m. The depth of C2 is 25 ms (TWT) corresponding to 18,75 m (TVD) (Vp = 1500 m/s). The C3 is located 350 m NE of C2 and has a more sub-circular shape. It is 277 m in diameter, and it's the deepest of the three depressions at 26 ms (TWT) (Vp = 1500 m/s gives a depth of 19,5 m (TVD)). Like C1, both C2 and C3 have deformation of the seismic reflection traceable down to 13 ms (TWT) in the Nordland Group, this is roughly 25 ms (TWT) above the Top Torsk/URU horizon.

4.6.2.8 ID's in the south of EN0702

The depressions located within the south block of the study area are all situated within parallel features, made by scouring at the base of a mobile glacier. The area is located approximately 10 km SE of the Western block (Fig. 4.40, 4.41 and 4.42). The water depth in this area ranges from 490 ms (TWT) to 430 ms (TWT). The Nordland Group is roughly 100 ms (TWT) thick in this area, and the depth of the parallel furrow and scour marks are up to 30 ms. The block

lies on over of the TFFZ, and the deeper stratigraphy is characterized by heavy faulting and deformation.

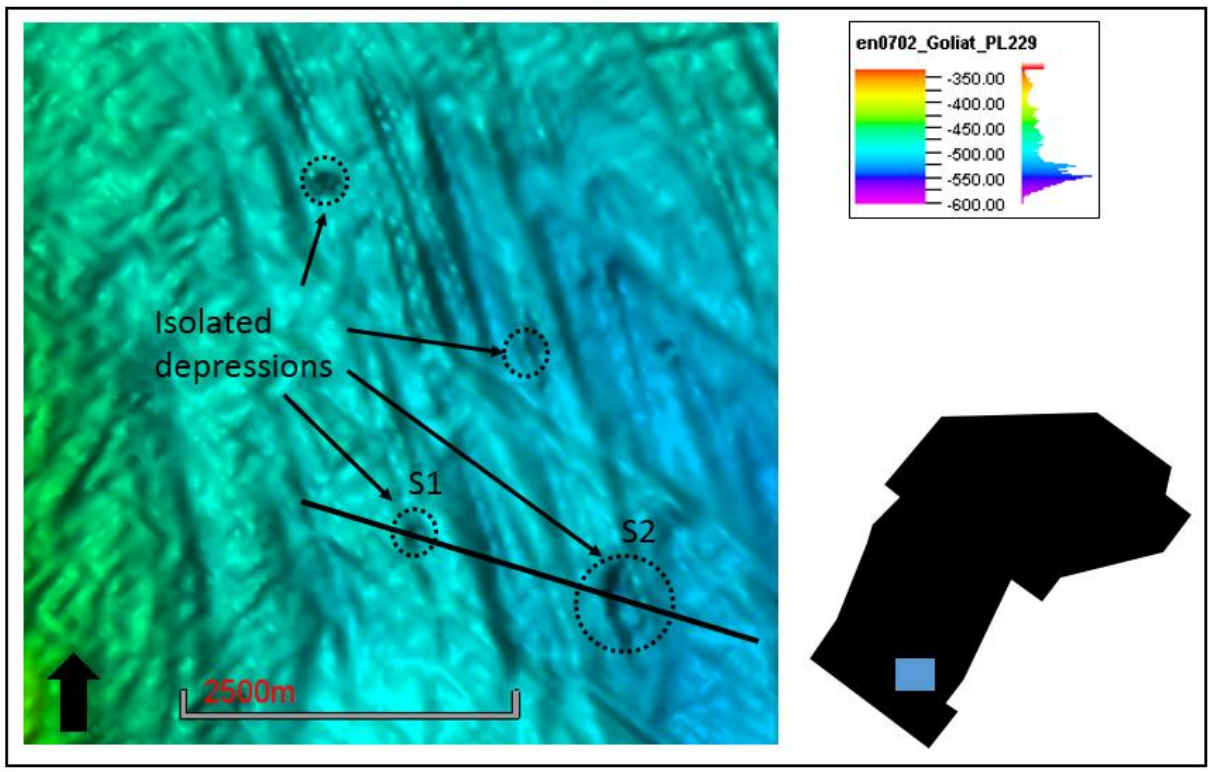

Figure 4.40 *Overview of the ID's in the southern parts of the study area. Their location is indicated on the black EN0702 survey polygon.*

4.6.2.9 ID S1 and S2

ID S1 is a sub-circular depression located within a 3 km long erosional furrow (Fig. 4.40). The S1 depression is 192 m long and has a depth of 20 ms (TWT). The deformation is traceable down to 41 ms (TWT) below the seabed, 33 ms (TWT) above the Top Torsk/URU horizon. The S1 covers an area of 0,11 km^2.

ID S2 is located 1.3 km SE of S1 (Fig. 4.40), and has a more elongated shape (Fig. 4.42), with the longest axis oriented in a NNW – SSE direction. The longest axis measures 477 m and the short axis is 291 m. The deformation of the seismic reflector seems to be traceable down to the Top Torsk/URU horizon, approximately 60 ms (TWT), but the reflectors in this area are highly distorted and it is not completely certain where the URU reflector continues east of the TFFZ. The depth of S2 is 24 ms (TWT), and the depression covers an area of 0,42 km^2, making it the biggest depression observed in the study area.

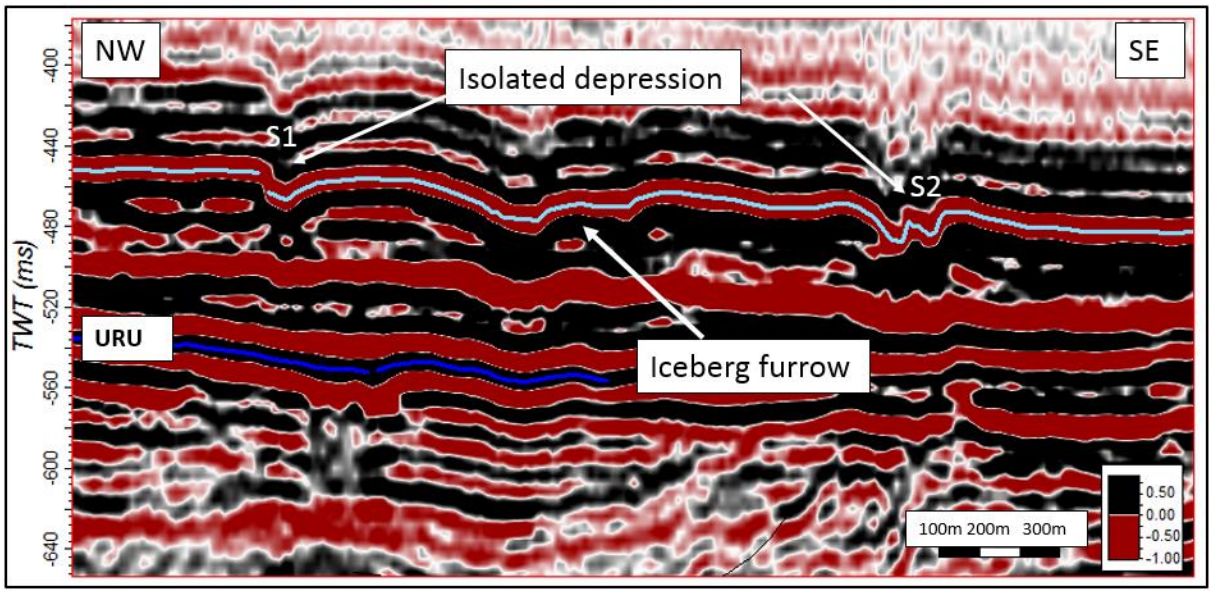

Figure 4.41 *Seismic profile line showing two of the ID's in Fig. 4.40 (S1 and S2). The profile line cross cuts the ID's in an NW - SE direction. Location of profile line is indicated in Fig. 4.40*

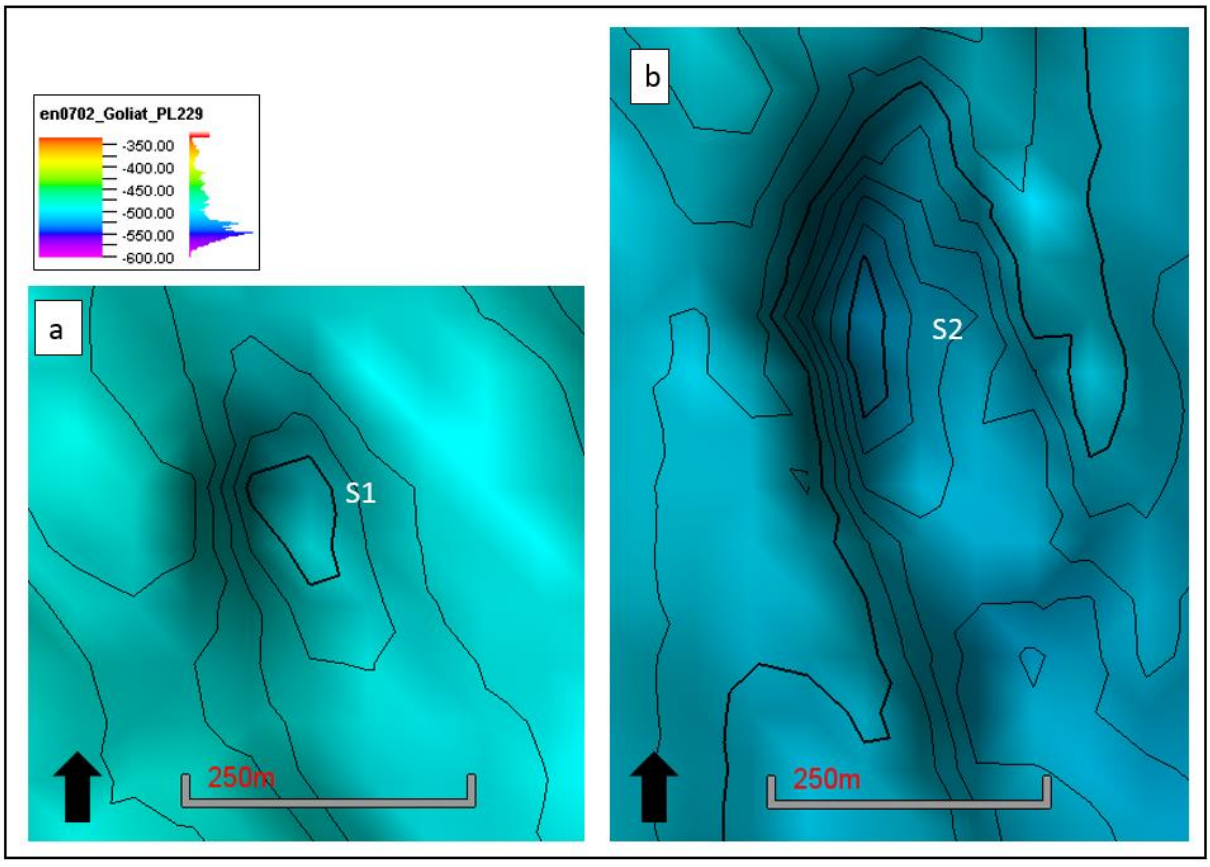

Figure 4.42 *Close-up of the two ID's indicated in fig 4.40 and 4.41. Location shown in Fig. 4.40*

4.6.2.10 Summary of depressions on the seafloor

Table 4-3 gives a short summary of the interpreted and presented isolated pockmarks in this chapter. In general, they cover an average area of 0.6 km^2, and the average TWT depth is 24,5ms, which corresponds to 18,37 m (TVD) respectively. No apparent correlations between deeper features (e.g. faults or signs of fluid flow) are observed in this study, but it should not be ruled out that they might me present.

Table 4-3 *summarization of the mega scale depressions (IPs) presented in chapter 4.6.2.*

ID	Long axis (m)	Short axis (m)	Area (km^2)	Depth ms (TWT)	Depth m (Vp = 1.500 m/s)
NW1	287	250	0,05	30	22,5
NW2	362	220	0,06	22	16,5
W1	300	236	0,05	28	21
C1	283	283	0,06	21	15,75
C2	493	207	0,07	25	18,75
C3	277	277	0,06	26	19,5
S1	192	192	0,03	20	15
S2	477	291	0,10	24	18

5 Discussion

In this chapter, the main objective will be to discuss the observed structures, stratigraphy and possible fluid flow features from the 3D seismic dataset EN0702. The overall goal is to integrate these observations and try to explain processes and mechanisms of fluid leakage and fluid accumulation and, it's potential link to deeper-seated hydrocarbon reservoirs.

5.1 Leakage processes

Fluid flow in sedimentary basins is driven by pressure differences, where fluids flow from areas with high pressure to areas with lower pressures (Bjørlykke, 1993). The flow of migration or hydrocarbons in sedimentary basins must be considered as a two-phase process, where the primary expulsion of hydrocarbons happens as a result of increased pressures in the source rock when the kerogen is altered into petroleum (Bjørlykke, 1993). After the formation of hydrocarbons, the buoyancy differences will drive the hydrocarbons upwards if this is possible, either along carrier beds with high enough permeability and porosity, or along zones of weakness like fault planes and fractures. If the hydrocarbons find a way to migrate, the continuous leakage might cause accumulation in shallower strata, or flow all the way through the overlying beds and leak out at the seabed. Below, I will discuss structures that facilitate fluid migration and their relevance in the Goliat field area.

5.1.1 Leakage along fault planes

Fluid migration along fault planes is one of the most important factors for fluid flow in basins worldwide (Berndt, 2005). Faults act as conduits for fluids from the subsurface, especially in deeper basins where the stratigraphy could be partly or completely lithified (Ligtenberg, 2005). The fluids will naturally flow through zones of weakness along the fault plane, until it reaches an impermeable barrier (Ligtenberg, 2005). The faults examined in chapter 4.2 are found all over the study area, and are common throughout the whole Hammerfest Basin (Ostanin et al., 2012). In the study area, they are particularly concentrated at the flanks and over the rollover structure (Fig 4.10 and 4.14, closely spaced faults).

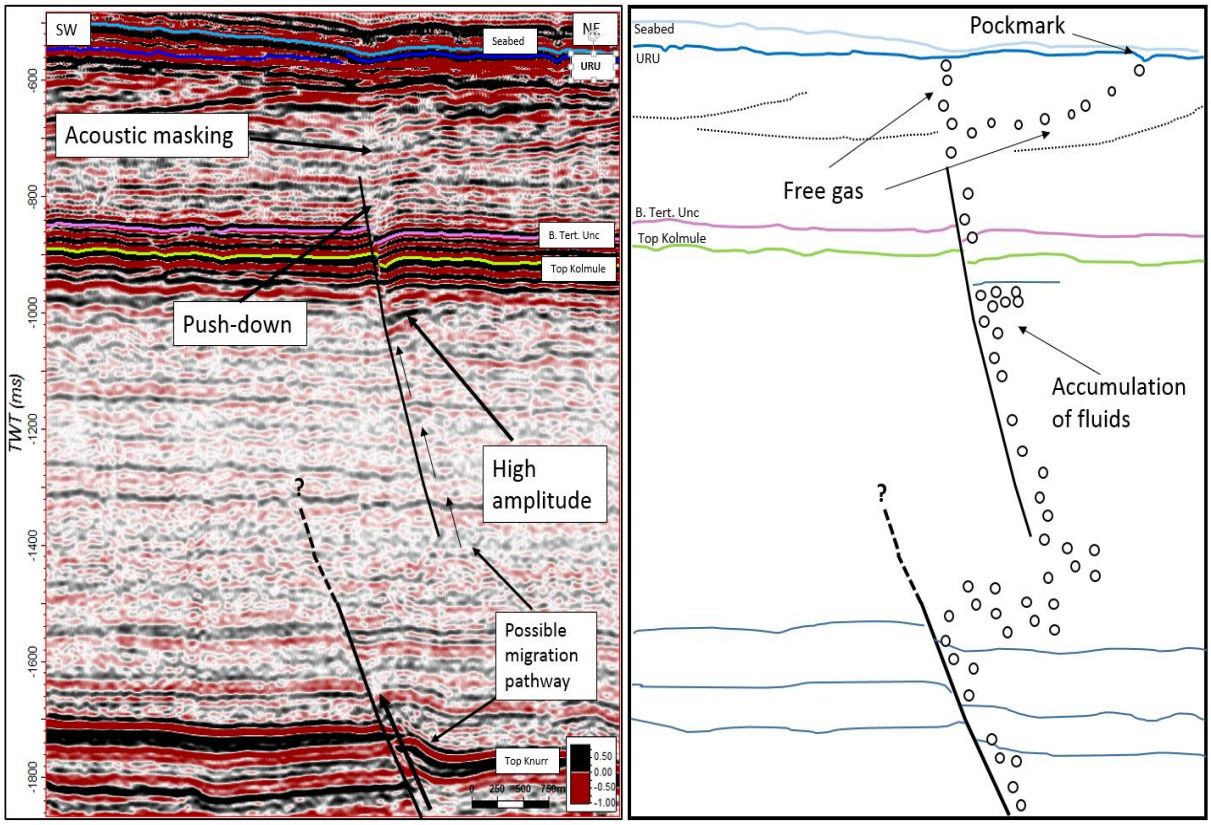

Figure 5.1 *Conceptual sketch of how deeper-seated faults can help as migration pathways for thermogenic fluids, into shallower strata where younger faults also may act as migration pathways for fluids. Location of seismic profile is shown in Fig. 4.14.*

The Torsk Formation over the Goliat oil field is characterized by numerous possible fluid flow features, including zones with low reflectivity, high amplitude areas with bright spots, seismic masking and acoustic turbidity, all considered to indicate the presence of shallow, free gas (Løseth et al., 2009). Seismic turbidity often follows the fault plane vertically (Fig. 4.15, 4.16 and 4.18), probably indicating that seismic energy is attenuated and scattered by gas-rich fluids migrating along the fault plane. Small amplitude anomalies along stratigraphic beds adjacent to the fault plane (Fig. 4.15 and 5.2), likely indicate that fluids migrating upwards along the fault plane get trapped laterally into more permeable beds. The AA3 – AA10 are situated over the Goliat hydrocarbon reservoirs (Fig. 4.21 and Fig. 4.24 – 4.31), where there are no Lower Kolmule polygonal faults recognized from the seismic over the rollover structure. The polygonal faults are only found over the rollover structure further north, where the structure deepens and the thickness of the Kolmule Formation increases. It is therefore likely that there is a correlation between the sediment thickness and the appearance of the Lower Kolmule polygonal faults (Ostanin et al., 2012). The amplitude anomalies in this area are thus not likely to be related to the Lower Kolmule polygonal fault system.

The AA3 – AA10 do, however tend to widen out along with the same fault plane as the deeper-seated Jurassic - Permian faults, where they are connected to the Upper Kolmule polygonal fault system (Fig. 4.19). Several fluid flow features are observed where deeper-seated faults connect with the Upper Kolmule polygonal faults (Fig. 4.19). Although most of the amplitude anomalies are concentrated in the area close to the hydrocarbon reservoirs, it should not be ruled out that they may in fact be present throughout the whole study area, but due to poor image quality, they are difficult to detect in the seismic and on the attribute maps.

As mentioned in chapter 4.2 the Goliat area is situated adjacent to the Finnmark platform in a large rollover structure, close to the highly deformed TFFZ (Fig 4.2). The geometry of the rollover may indicate that the cap rock is at its thinnest at the flanks of structure, as these areas will experience higher strain (Fossen and Gabrielsen, 2005). Studies of the seismic show that this is indeed the case. Fig. 4.14 shows that the areas with the highest amount of faults are at the rollover structure's flanks close to the TFFZ and to the North and northwest in the study area. The top seal, Hekkingen formation (just below the BCU in Fig. 4.2) is bisected by numerous faults, and the deformation is more extensive on the flanks of the rollover. If the top seal is thinner in the same area, it should be logical to assume that leakage would occur here. Amplitude anomaly 10 is located over the southeastern flanks of the structure. The gas could have escaped through the faults bisecting the caprock. As the area underwent uplift and erosion, the pressure relief would cause the gas to expand vastly, increasing the strain and help trigger the formation of faults. The semi-transparent caprock and the leakage along faults is a possible explanation as to why the gas was released from the oil and leaked out of the reservoir, while the oil remained in the reservoir. Sales type II or III trap would fit the Goliat structure according to Sales description of different trap types (Sales, 1993). Karlsen and Skeie (2006) also describes how a thin cap-rock would lose methane through diffusion processes and molecular sieving, leaving the oil in the reservoir while the gas escapes (Figure 5.3).

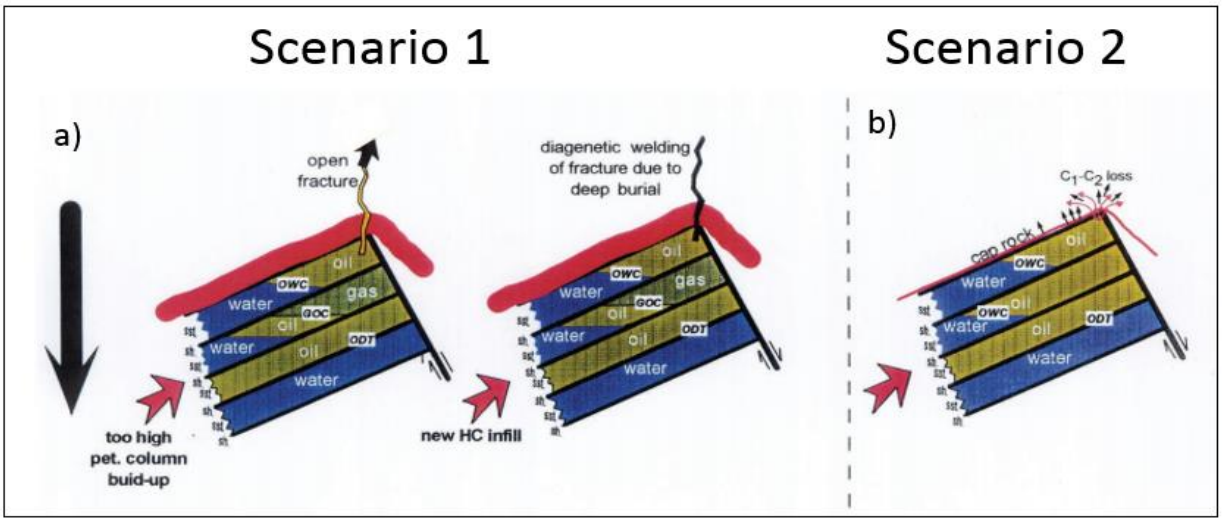

Figure 5.2 *The model gives a schematic overview of the cap rocks integrity based on its thickness in a continuously subsiding basin.* ***a)*** *In scenario 1, the thick cap rock allows the gas to accumulate. As the basin subside, it will eventually be expelled as the source rocks reach the level they become mature. This might cause the cap rock to expel oil or it could result in the build-up of an overpressure high enough to induce cap rock fracturing.* ***b)*** *On the contrary, in scenario 2 the cap rock is thin enough for the gas to continuously bleed out, and leave the heavier oil in place. Modified after Karlsen and Skeie (2006).*

5.1.2 Origin of polygonal faults in the Goliat area

Two different Polygonal fault tiers are recognized in this study. Polygonal faults are not induced by tectonically or gravitational driven forces, instead their formation and distribution are controlled both laterally and vertically by the lithology (Cartwright and Dewhurst, 1998; Dewhurst et al., 1999; Cartwright et al., 2003). Polygonal faults are found in sedimentary basin globally, and form in tectonically stable or passive margin basins (Sun et al., 2010; Cartwright, 2011).

As mentioned in chapter 1.2.5, different mechanisms behind the genesis of polygonal faults have been discussed. Cartwright et al. (2003) argues that synerisis is one of the most likely causes of fault initiation, which builds on the processes where spontaneous contraction happens without any evaporation. This implies that the sediments must consist of very fine-grained sediments and mudstones containing fluids in order to rearrange the matrix such that it's possible to shrink instantaneously. Polygonal faults may develop as a result of compaction and consolidation processes during burial. The compaction can lead to dewatering of the sediments, which is connected to fluid migration as shown in Fig. 5.3.

The polygonal fault's so-called tiers studied in the EN0702 dataset affect different stratigraphic levels. They are similar in appearance and map view, but have different characteristics in seismic sections. The Lower Kolmule polygonal faults are confined to an interval between 1.2 s and 1.5 s (TWT) (Fig. 4.13 and 4.14). The seismic expression of the fault tier is consistent throughout the whole study area. The Upper Kolmule polygonal faults are on the contrary to the Lower Kolmule polygonal faults not confined to a single tier. By this, it means that their seismic expression deviates from the traditional polygonal faults, as they bisect different stratigraphic boundaries. This implies that the Upper Kolmule polygonal faults may have been reactivated as extensional faults.

Ostanin et al (2012) discusses the Upper Cretaceous polygonal fault network found in the Hammerfest Basin. They interpreted the faults that bisect the Paleocene – Eocene stratigraphic intervals to be reactivated polygonal faults, or Paleocene – Early Eocene Faults (PEEFs) (Figure 5.1 and 5.3). These are found throughout the Hammerfest Basin, and is likely the same type of faults are in this thesis called the upper Kolmule polygonal faults. The difference between the lower Kolmule polygonal faults and the upper Kolmule polygonal faults is the stratigraphic intervals they affect. While the Lower Kolmule Polygonal faults are confined to a short stratigraphic interval between 1.2 s (TWT) and 1.5 s (TWT), the Upper Kolmule polygonal faults are traceable down to the Top Knurr horizon, and up into the Paleocene – Eocene Torsk Formation, indicating that they have been reactivated as extensional faults. The seismic expression of these faults are that of polygonal faults, but their general characteristics in the study area show that they have been reactivated, maybe more than once, and are thus similar to the PEEFs (Fig 5.1). Because the Upper Kolmule polygonal faults affect different stratigraphic levels, the possibility for them being conduits of fluids from deeper stratigraphy to shallower levels are present, as explained in Fig. 5.1 **c)**.

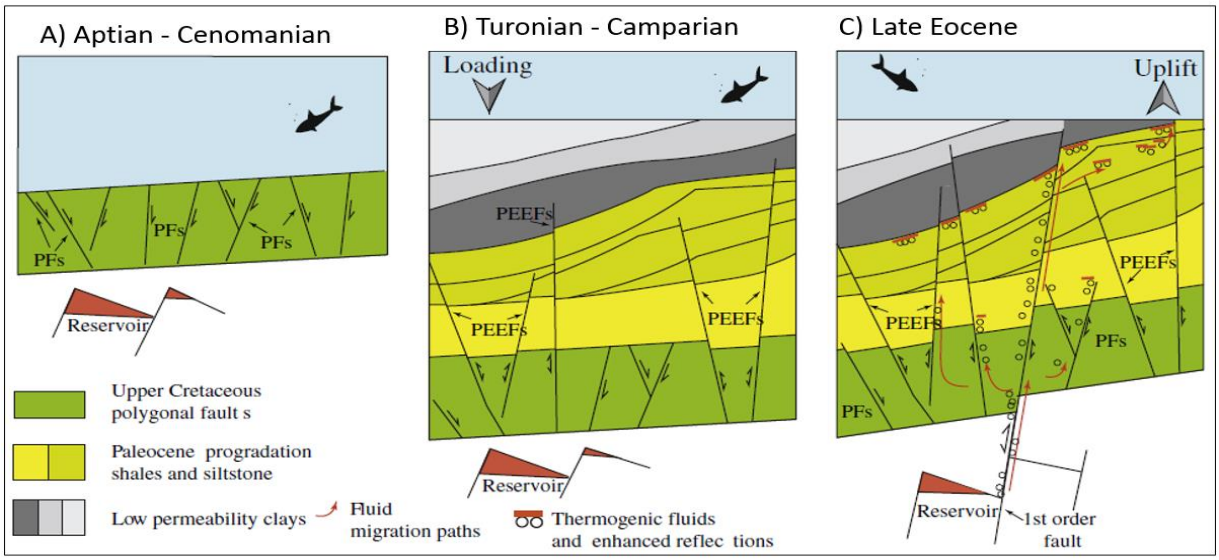

Figure 5.3 *Illustration of the development of polygonal faults and the reactivation of polygonal faults to form PEEFs.* ***A)*** *The likely timing for the formation of the polygonal faults.* ***B)*** *Loading of new sediments could have resulted in the reactivation of the polygonal faults and from PEEFs.* ***C)*** *The Late Eocene uplift combined with the reactivation of regional deep-seated faults could result in further PEEF reactivation. Fluids from the deeper-seated reservoirs migrate through the deep-seated faults, where the PEE's acts as secondary migration pathways for the thermogenic fluids. In areas of impermeable barriers, enhanced reflectors may show up on the seismic. Modified from Ostanin et al., 2012*

5.1.3 Timing of fault activity, reactivation and fluid flow

The Lower Kolmule polygonal faults are only found where the Kolmule stratigraphy is at it's thickest in the study area. The faults are waning towards the rollover structure. Because the area has experienced severe uplift with following erosion (Vorren et al., 1991; Dimakis et al., 1998; Cavanagh et al., 2006) after the Cenozoic, studies suggest that as much as 1000 m of sediments have been eroded in the central parts of the Hammerfest Basin (Linjordet and Olsen, 1992; Cavanagh et al., 2006; Ohm et al., 2008). Due to this, it is therefore difficult to make any exact, or even relative estimates of when the polygonal faults in the Lower Kolmule Formation were initiated. On the contrary, the Upper Kolmule polygonal faults seem however to terminate below URU (no bisecting of the URU is observed in the study area) so the fault activity had most likely ceased by that time, which is also in accordance with the observations of Ostanin et al. (2012). The Upper Kolmule Polygonal faults seems to intensify and show a higher density over the rollover structure (Fig. 4.10), as often observed in anticlines where the outer arch experiences higher extensional strain than the inner arch (Fossen and Gabrielsen, 2005). It is also mostly in these areas the observed columnar vertical structures, or pipe-structures are located. Pipe-structures related to fluid flow seem to occur in areas with high strain, often associated with higher density of faults (Fossen and Gabrielsen, 2005).

Both the Lower Kolmule and Upper Kolmule polygonal fault systems have the potential to work as easy migration pathways for fluids. They may act as conduits for fluids through otherwise impermeable stratigraphic layers, additionally is also a much faster way of migration compared to vertical diffusion flow through stratigraphy with low porosity and permeability (Laberg et al., 1998; Brown, 2000; Gay and Berndt, 2007). The faults observed in the study could, due to reactivation, operate as migration pathways for thermogenic fluids ascending from the Jurassic reservoirs through the Cretaceous strata and further up into the Paleocene – Eocene stratigraphy. Here it could migrate both laterally along the polygonal fault systems and if the permeability and porosity were right, the fluids would be able to migrate horizontally as shown in Fig. 5.3. This would correlate well with AA1 and AA2.

5.1.4 Vertical columnar features

Many of the vertical columnar features interpreted as pipe-structures in this work are associated with pushdown or pullup of the seismic reflector. Pushdowns are a result of local low-velocity regions, while the pullup appears as a response to a shallower high-velocity region (Løseth et al., 2009). They appear on seismic as narrow vertical zones where the reflectors are disturbed. They are often associated with depressions or craters on the seafloor (Løseth et al., 2011). Several pipe structures are observed in the study area and mentioned in chapter 4.3 and 4.4. They are found along with possible leakage along fault planes, as shown in Fig 4.16 and 4.18. Fig. 4.20 is also interpreted as a pipe structure, but no pockmarks or depressions are associated with any of the mentioned pipes. Pipe structures are also found where there are amplitude anomalies. AA6 (Fig. 4.27) and AA8 (Fig. 4.29) are examples of pipe structures related to amplitude anomalies, also here, without the presence of any pockmarks.

5.1.5 Fault strike and the potential of fault leakage

Studies of core samples and the measurement of maximum horizontal stress azimuth (S_{Hmax}) were conducted by Linjordet and Olsen (1992), based on well data and core-samples from the Snøhvit oil and gas field in the central parts of the Hammerfest Basin. They found that the S_{Hmax} in the east of the Hammerfest Basin is at 135N and in the west at 35N, based on measurements of the Torsk Formation. The stress field from the Aptian, Lower Kolmule Formation was measured to be at 0N in the west and from 170N to 165N to the East. Faults oriented orthogonal to the maximum horizontal (extensional) stress are more likely to fail, and stay "open" to fluid migration (Linjordet and Olsen, 1992), as the normal stress is at it's lowest across the fault

plane (Ligtenberg, 2005). In the study area there seems to be a direct link between the deeper oil reservoirs in the Goliat structure and several of the shallower amplitude anomalies in the Torsk Formation. By using the information from Linjordet and Olsen (1992), it should be possible to get an indication as to which faults would likely work as migration pathways for the hydrocarbons. Ostanin et al. (2012) argues that by studying the N – S oriented S_{Hmax} in the Aptian, it should indicate that the E – W faults and fractures would be impermeable, while the N – S oriented faults would, in theory be open to fluid flow migration. AA3, 4 and 5 all have N – S oriented faults directly underneath them, and under AA5, the deeper-seated Jurassic – Permian faults have the same orientation. Additionally, one of the main orientation for the Lower Kolmule Polygonal faults is in NNW – SSE, and these could potentially also be facilitated as migration pathways. The main timing for the filling of the Goliat structure is believed to have happened in the early Paleogene (Berglund et al., 1986; Linjordet and Olsen, 1992), so the favourable stress orientation in the Aptian, was before the fluid migration started. Thus, it is of little importance, except for accumulation of fluids along the N – S oriented fault planes. The 0N and 170N – 165N in the Pleistocene – Eocene Torsk Formation is however oriented, so the E – W faults would be open during this time. This could suggest that fluids that leaked along the N –S oriented faults in Aptian, could follow the newly initiated E – W oriented faults, and possibly some of the SE – NW and NE – SW oriented faults into shallower strata. The change in S_{Hmax} from Aptian to Paleocene – Eocene could indicate that there is a relationship between the stress orientation and the leakage of fluids from deeper-seated reservoirs through the network of Lower Kolmule polygonal faults and up into the shallower Torsk Formation through the Upper Kolmule polygonal fault tier.

As most of the amplitude anomalies are found within proximity to the Goliat oil accumulation it is logical to draw the conclusion that these have the same thermogenic source, but vertical columnar structures like the one presented in Fig. 4.20 seem to be unrelated to these accumulations, and could thus have a different origin. However, if the polygonal fault network in Lower Kolmule could act as pathways, it is possible that the fluids in this area share the same source as the accumulations directly above the reservoir. This cannot be seen directly on the seismic, but as mentioned in chapter 4.3.1, the min curvature map reveals an N – S trending Upper Kolmule polygonal fault just beneath the pipe structure, which according to the S_{Hmax} studies therefore could be leaking. The study area shows a highly complex geology with more than one set of polygonal faults, possibly interacting, and it could also be that the Lower

Kolmule Polygonal fault tier could work as a plumbing system, distributing fluids to more distal parts of the study area. This cannot be seen directly on the seismic, but as mentioned in chapter 4.3.1, the min curvature map reveals an N – S trending Upper Kolmule polygonal fault just beneath the pipe structure, which according to the S_{Hmax} studies therefore could be leaking. Ostanin et al (2012) claims that polygonal faults and PEEF's are restricted to the upper 1500 m of sediments, meaning that the S_{Hmax} and the distribution of the Lower Kolmule polygonal fault system could potentially play an important part in the distribution of fluids to the area.

It is likely that several of the deep-seated faults bisection the BCU could act as conduits for thermogenic fluids to shallower stratigraphy, and from there two different sets of polygonal faults, where one shows extensional reactivation could act as migration pathways for the thermogenic fluids towards the surface (Fig 5.4). The same figure corresponds with the observations of AA2, and is based on a seismic section through the anomaly. The bubbles indicate free gas and fluid accumulations. As the bubbles represent gas in the sediments, and no seepage through the seafloor towards the sea surface is observed, it indicates that this is a process that has previously happened.

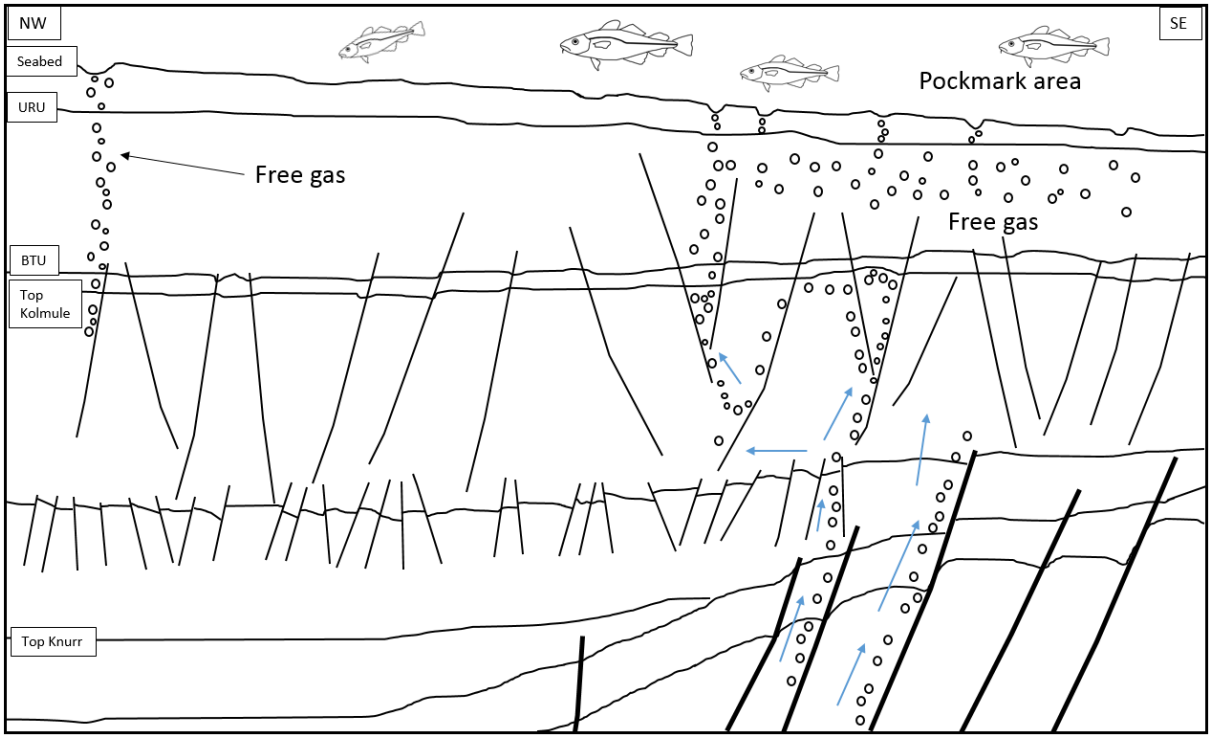

Figure 5.4 *A schematic overview of the possible correlation between deeper-seated faults, polygonal faults and the distribution of fluids in the Goliat area. The bubbles indicates free gas and fluid accumulation, while the blue arrows indicate possible fluid migration pathways. The bubbles lies underneath the seabed, indicating that there is no active seepage today. The figure corresponds with the observations from AA1.*

Pau et al. (2014) discusses the timing of pockmark formation, and found that they could have been initiated about 15ca ka-1 BP in the Bølling interstadial, as a result of methane expulsion and rising sea level temperatures when the ice overburden was removed. The destabilisation of the methane hydrates caused the fluids to seep upwards and from the seabed into the water. They also claim that the seepage was persistent for several thousands of years.

This seems to be in accordance with Crémière et al. (2016) who U-Th dated carbonate crusts in glaciomarine sediments in the SW Barents Sea and Norwegian Sea. The dating indicated a main fluid flux around 17 and 7 ka.

Both of these studies correlate well with the seismic indicators on trapped gas below the seabed in the study area.

5.2 Shallow gas accumulations

Gas trapped in the upper most part of the subsurface is known as shallow gas accumulations. But the definition of "shallow gas" varies in the literature. Therefore, in this work, any accumulation above the Base Cretaceous Unconformity, is regarded as shallow accumulations. Several authors have documented the migration of fluids in the South West Barents Sea (e.g. Chand et al. (2012) Ostanin et al. (2013), Vadakkepuliyambatta et al. (2013)) and on the seismic they are visible and recognized as chimney and pipe structures, acoustic masking, and shadow zones along with high amplitude areas, pushdowns and acoustic turbidity. The buried sediments that are impregnated with hydrocarbons are mainly containing methane, with some minor additional components like ethane and carbon dioxide (Judd and Hovland, 2009). Most of the gas in the subsurface is generated by either biogenic or thermogenic processes (Davis, 1992; Floodgate and Judd, 1992).

Previous studies (e.g. Laberg et al. (1998)) have proposed that the shallow accumulations could be a result of leakage from deeper-seated hydrocarbon reservoirs.

The uplift and erosion of the overburden have cleared most of the Late Cretaceous and Tertiary sediments in the SW Barents Sea, which have caused the gas to expand. As a result, there has been a depleting of the deeper accumulations, especially in traps with leaking cap rocks (Ohm et al., 2008). This seems to be the general trend in the Barents Sea region where many exploration wells find structures with dismigrated petroleum charge (Nyland et al., 1992; Doré and Jensen, 1996; Cavanagh et al., 2006; Ohm et al., 2008). The Goliat accumulations, however

seem to deviate from this trend (Ohm et al., 2008). The Goliat structure might be an example of a structure where a semi-permeable cap rock has allowed gas to percolate out through the seal, but retaining the oil, and thus deviate from the favourable situation where the cap rock is non-leaking (Ohm et al., 2008).

5.2.1 Sources of hydrocarbons in the Goliat area

Ohm et al. (2008) discovered that the oil from the Goliat field is a mixture of hydrocarbons from several intervals of source rocks. It is therefore likely that hydrocarbons in the study area may have more than one source, and due to the tectonic history, the source could be of both proximal and distal origin.

The presence of an underlying hydrocarbon reservoir could explain why the amplitude anomalies are only confined to a small part of the study area, and it also implies that little lateral migration has occurred in the Torsk formation.

Ohm et al. (2008) and Doré (1995) discusses the different source rocks in the SW Barents sea based on the TOC, hydrogen Index (HI) and the hydrocarbons potential to produce oil and/or gas (S2). In chapter 2.4, three different sources are pointed out. One is the Late Jurassic Hekkingen Formation and the two others, Snadd and Kobbe Formations are from the Middle and Upper Triassic. Fig 5.5 modified after Ohm et al. (2008) shows that all the mentioned source rocks are present in the study area, and within the oil window (red dotted line). The Hekkingen Formation is currently expelling oil in the Hammerfest Basin, and it is likely to assume this might be the source for the shallow gas in the area. However, as the SW Barents Sea has undergone several phases of uplift and erosion, this may have caused cap rocks to fail and oil could have re-migrated from previous traps, e.g. from the deeper Tromsø basin and into the Hammerfest Basin (Ohm et al., 2008).

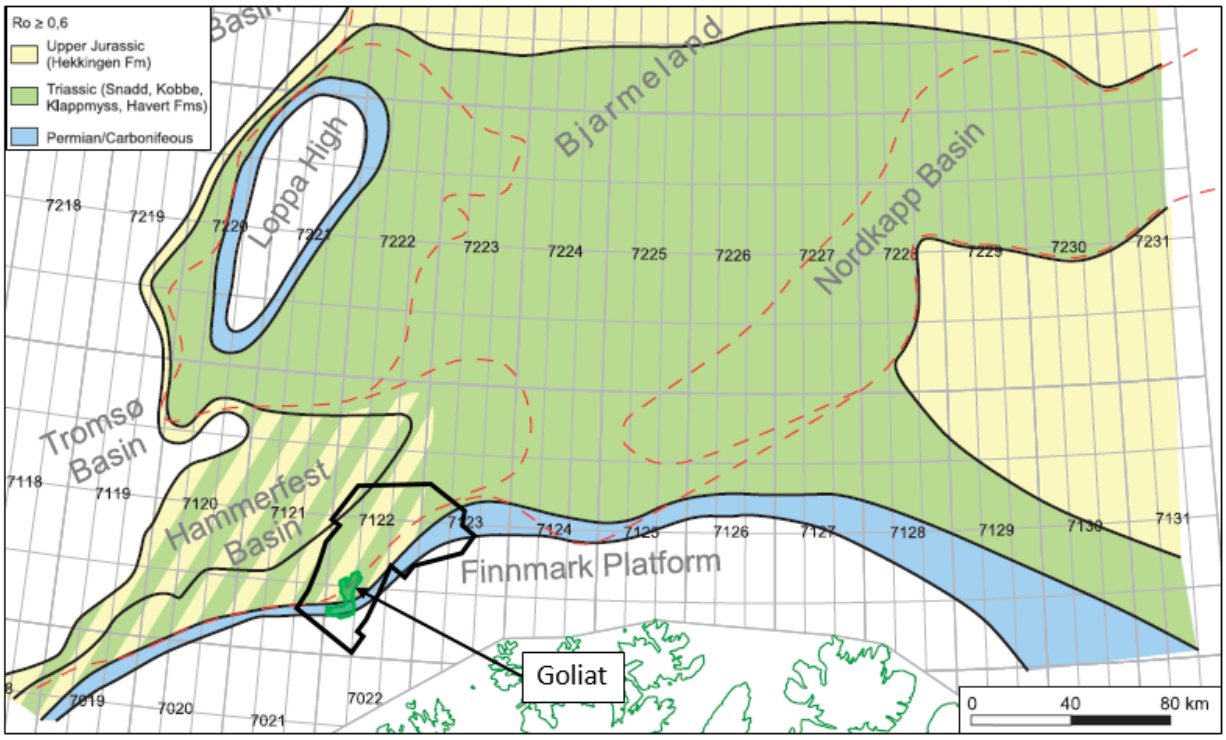

Figure 5.5 *A tentative maturity map over the southwestern Barents Sea. Both Jurassic and Triassic source rocks are available in the Hammerfest basin and within the study area (marked with black outline of the EN0702 survey). The Goliat oil accumulations are shown in dark green. It is easy to draw the conclusion that the oil in the area is sourced from the Upper Jurassic Hekkingen formation or The Triassic Formations, but studies show that the oil may in fact be a combination of several sources (Ohm et al., 2008). Modified after Ohm et al. (2008).*

5.2.2 Mechanisms behind shallow gas accumulations

The origin of shallow gas accumulations relies on the presence of a source rock, which has the ability to generate hydrocarbons. Either this means that in areas where shallow gas accumulations occur, a source rock must be present within the same area, or the gas could accumulate through secondary migration from stratigraphic and structural traps within the area. Previous studies (e.g. Laberg et al. (1998)) have proposed that the shallow accumulations could be a result of leakage from deeper-seated hydrocarbon reservoirs.

As most of the amplitude anomalies in this study are found along the URU (see also following subchapter), it is likely that the unconformity acts as an impermeable barrier in most places. Several of the anomalies can be traced parallel to the interpreted seabed reflection and anomalies running parallel to the seabed within a certain interval can sometimes be recognized as what could be bottom simulating reflectors (BSRs). Especially AA1, AA3, AA4 and AA8 – AA10 seem to follow this trend. Although no BSRs is recognized specifically in the study area in this work, there have been several studies on BSRs in the Hammerfest Basin (e.g. Chand et al. (2008) and Chand et al. (2012). It is however important to mention that no gas hydrates have

been identified in the seismic dataset from the study area in this work, as it is never possible to identify hydrates by use of p-wave seismic data alone, thus it will not be considered further.

5.2.3 Distribution of amplitude anomalies

The amplitude anomalies described in chapter 4.5 are mostly confined to an area of less than 50 km^2 in the SE parts of the survey area close to the TFFZ (Fig. 4.21). AA3 – AA10 are found close together, while AA1 and AA2 are located approximately 3km north of AA3 – AA10. Fig 4.21 shows the location of the amplitude anomalies and the position of the wells mentioned in chapter 3.1.7 and as shown in Figure 4.2, all offset wells are in direct contact with or in close vicinity to the mapped amplitude anomalies.

As mentioned previously in chapter 4.4 and briefly in 5.1 many of the amplitude anomalies are situated above faults affecting different stratigraphy. Table 4.2 gives an overview of the related faults, both deep-seated and shallow, and in most cases the anomalies have both fault types present. The location of the anomalies could indicate that there is or previously have been leakage directly from the deeper seated reservoirs, and since the hydrocarbon reservoirs are situated directly beneath these anomalies, this is not an illogical assumption.

5.3 Leakage on the seafloor

Depressions covering large areas of the seafloor have been identified in the EN0702 dataset (Fig.4.32). They are observed mainly in the deeper parts of the Ingøydjupet, where the seabed is near horizontal with little topographic variation in a fine-grained muddy sedimentary setting. In chapter 4.6, the depressions were divided into two groups; isolated pockmarks (IPs) and small-scale depressions/pockmarks although both of them could be classified as pockmarks. The former is mainly observed in the shallow areas where the seafloor shows a more rugged topography. The smaller pockmarks appear in clusters of up to 165 pockmarks per km^2 in the deeper parts of the study area (estimated from the seabed seismic reflector). The pockmarks in the study area vary from 30 – 160 m in diameter (measured from the seismic data, which might not be as accurate as bathymetric data), while most of them lie within the 45 – 55m in diameter range. Fig. 4.32 shows the distribution and areas where the small pockmarks are clustered together. In the southeastern parts of the study area, two depressions marked by a red dotted line in Fig. 4.32 outline areas where pockmarks are found in glacial features. Both the areas are interpreted to be furrows and depressions made by scouring at the base of the glaciers in the Plio-Pleistocene (Andreassen et al., 2008).

Bathymetrical data from Mareano is available from the southwestern parts of the study area. They are of higher resolution compared to the EN0702 dataset. Thus, more details and smaller features can be resolved, as shown in Figure 5.6. The figure shows a comparison between the seismic surface map interpreted in this work and the multibeam data acquired by Mareano in the same area. The outline of the pockmark area in Fig. 5.6 shows that on the bathymetry data, the pockmark area extends further out towards west compared to the seismic interpretation to the right.

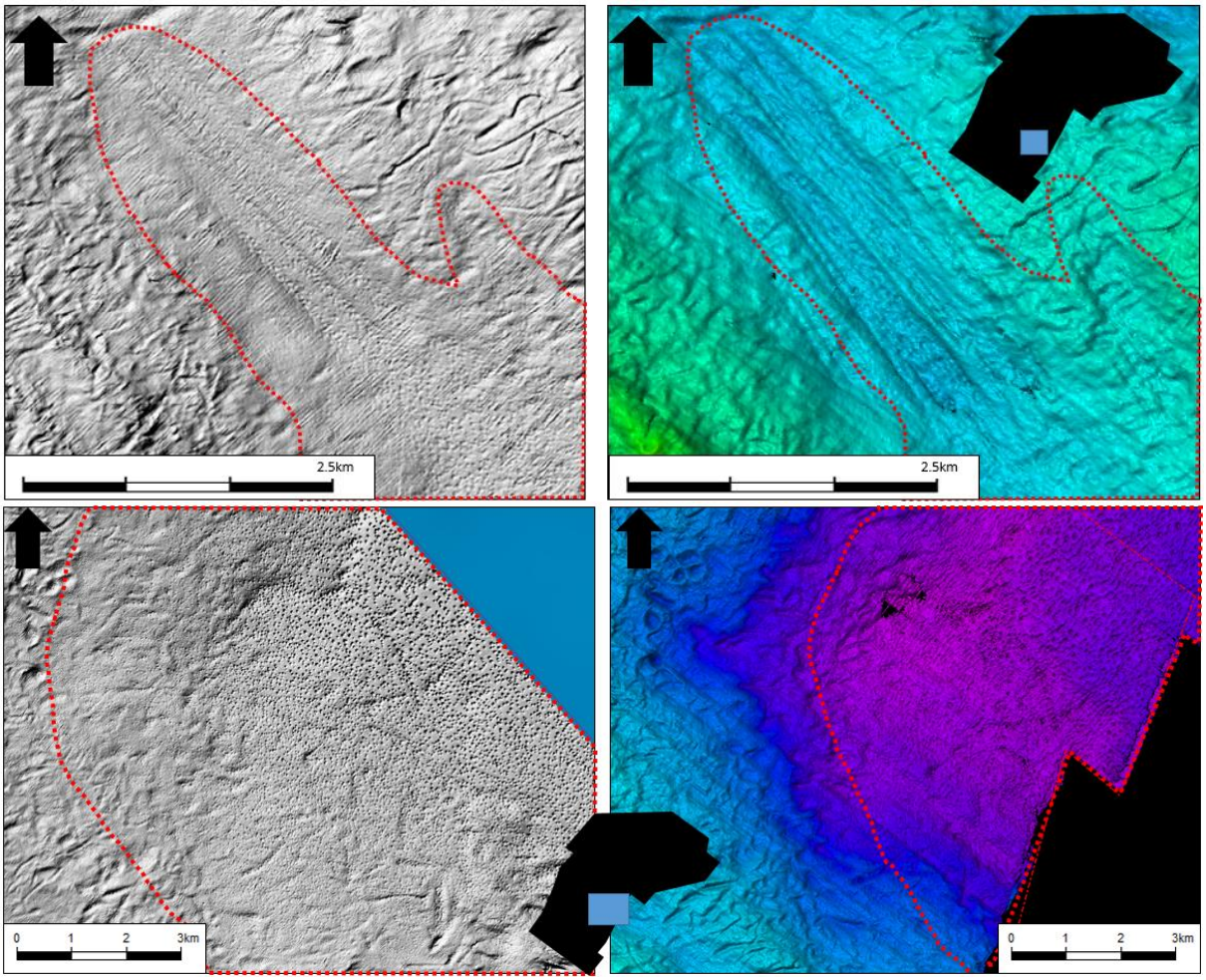

Figure 5.6 *Grey scale images of bathymetry data from Mareano compared to the interpreted seabed reflector in the seismic data. The bathymetry data's higher resolution makes it possible to imply that the pockmark area extends further out than what is visible in the seismic data. Grey scale bathymetrical images are obtained from the Mareano database at mareno.no*

Chand et al. (2009) made similar observations when they conducted a study of the S – SW parts of the EN0702 survey area. They found pockmark densities from 135 to 210 per km^2, with the highest density in the deeper areas, and less density where it shallows. In the same study, they used multibeam bathymetry and backscatter data, which helps to discriminate and visually enhance the pockmarks. They also observed that the pockmarks were confined to the deeper

parts, and along some of the local depressions. Additionally, they found a correlation between the reflectivity and the sediment type, as the pockmarks were located in areas with low reflectivity, associated with soft sediments (Fig. 5.7).

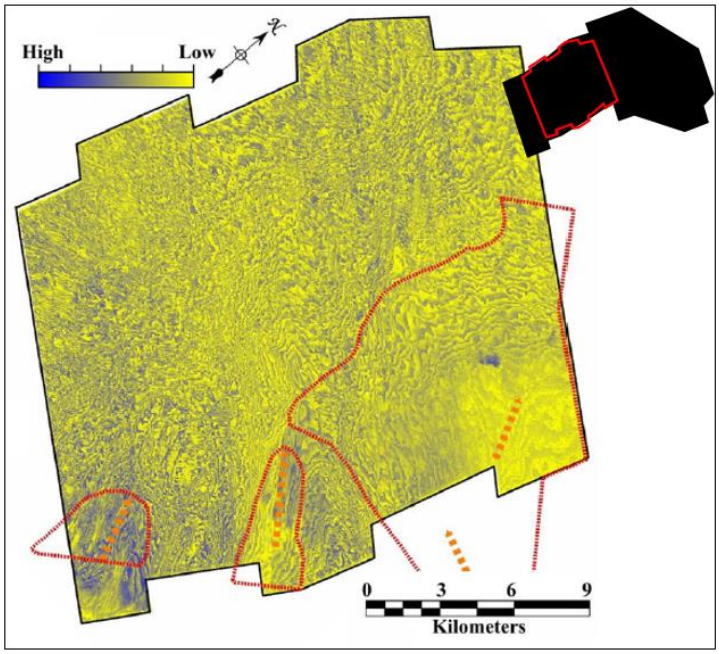

Figure 5.7 *Reflection map extracted from the seabed reflections first half cycle. The change in amplitude is clearly seen towards the NW corner of the study area, where the density of pockmarks are at its highest. The low amplitude is associated with fine-grained soft sediments. Modified after Chand et al. (2009). Survey area is located within the black EN0702 polygon in the upper right corner.*

As observed in this work, previous studies (e.g. Solheim and Elverhøi (1985) and Chand et al. (2009)) have also discussed the appearance of pockmarks in glacier-created depressions, and that deep scours and plough marks made at the eroding base of the ice might make it easier for fluids to escape through the sediments, following the creating of pockmarks.

5.3.1 Pockmarks and the location of amplitude anomalies

The amplitude anomalies presented in the result chapter, 4.5 are mostly found in near vicinity of each other (AA3 – AA10), only AA1 and AA2 are located approximately 3 km north of AA3 – AA10 as mentioned in chapter 5.2.2. By comparing the seabed surface extracted from the seismic reflector it seems that the enhanced reflectors or AA3 – AA10 are located in areas devoid of pockmarks, so there seems to be no apparent correlation between the two. AA1 and AA2 are located where the seabed is deepening, and there are pockmarks over both of them. Although from the seismic, the pockmarks can only be recognized over AA2, the high

resolution bathymetry data from Mareano (Fig 5.6) reveals that there are pockmarks over AA1 also. It is possible that both AA1 and AA2 share the same source, or are connected as a larger accumulation. Their seismic expression and location makes it likely that they could be connected, and that the fluids encounter a stratigraphic barrier within these two areas with the result of increased amplitudes.

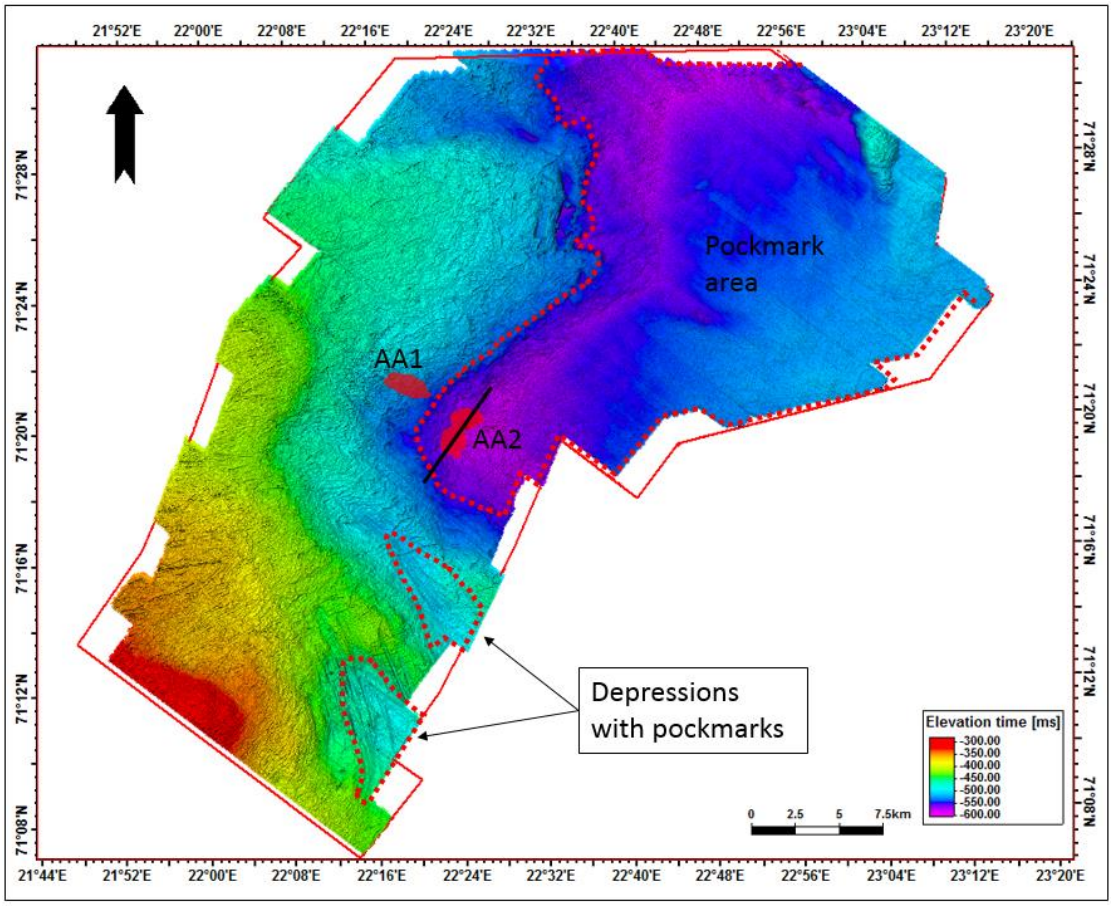

Figure 5.8 *Overview of the area where pockmarks can be interpreted from the seismic, and the location of amplitude anomaly 1 and 2. The red dotted line marks the boarder of the visible pockmark field from the seabed reflector of the seismic data, however, high resolution bathymetry data from Mareano reveals that the pockmark area extends further into the shallow Tromsøflaket.*

As AA3 – AA10 are located in an area devoid of pockmarks, it is possible that they are not related to seepage or leakage from the deeper seated reservoirs in the area, and that they have other sources. Chand et al. (2009) claimed that in order to create amplitude anomalies as prominent as the ones observed in the seismic data, a large amount of gas hydrates or free gas must be present, as both gas hydrates and free gas in the sediments have similar seismic signatures (Guerin and Goldberg, 2002). As no signs of gas hydrates are observed in this study, it would be interesting to conduct further studies with focus on gas hydrates within the same area.

At the end of the paper, Chand et al. (2009) mentions that a large fault in the western part of the survey area extends into from an area devoid of pockmarks and into the high density pockmark area. He argues that the fault is an important migration pathway for fluids to the Nordland Group sediments. This fault is the same fault that in this work is denoted the Tromsø-Finnmark Fault zone or TFFZ. The fault is a part of the fault complex that separates the basin from the Finnmark platform. Fig. 4.2 and 4.21 show the location of the fault(s) marked in black, and the same observation is made from the seismic data in this thesis. The highest density of pockmarks is found in relation to this fault zone, and especially in high numbers on the Finnmark platform, indicating that the TFFZ could be an important conduit for deeper-lying fluids to the Quaternary sediments.

The link between similar amplitude anomalies and pockmarks have been described by (Bünz et al., 2005) along the mid-Norwegian margin at the Storegga slide, where the amplitude anomalies where consistent with the presence of gas hydrates or free gas below the gas hydrates.

In general, pockmarks are a common feature throughout the Hammerfest basin, and they have previously been linked to subsurface fluid flow (e.g. Chand et al. (2008), Chand et al. (2009), Pau et al. (2014)).

The pockmarks found in the Barents Sea are likely a result of the several phases of uplift and erosion the Barents Shelf has been subject to since the last glaciation (Andreassen et al., 2004). The evidence of this is also observed from bathymetry, and the presence of plough-marks, furrows and mega scale glacial lineations, which the ice-streams and icebergs have left behind.

5.3.2 Isolated Depressions

In chapter 4.6.2 a few isolated depressions were presented. By studying seismic sections through them, attribute maps and reflectors, there is no direct evidence from the seismic that could correlate them to fluid flow. The isolated depressions could be an expression for drop-stones from icebergs, or areas where the keel of the iceberg came to a halt over a longer period. The wind and ocean currents could have caused rotational movement, until it melted enough to drop stones, or being carried away by the wind and ocean currents.

Bass and Woodworth-Lynas (1988) discussed that this could be the explanation behind several of the crater-like structures and depressions on the Labrador shelf. They argued that if the keel came to rest above the seafloor, it could create a crater chain or a normal scour if the keel would

remain at or below the seafloor over time. This could be the case in the studied dataset in this thesis, but bathymetrical data has not been obtained from the area where these depressions occur, and the seismic resolution is too low to observe such structures in detail.

6 Summary and conclusion

- Two distinct tiers of polygonal faults affecting different stratigraphic intervals are observed. The Lower Kolmule polygonal fault tier only affects a seismic window between 1.2 s and 1.5 s (TWT). The upper Kolmule polygonal faults affect both the Kolmule Formation and the Base Tertiary unconformity and penetrate up in the Torsk Formation. The latter is believed to be reactivated as extensional faults during later uplift and erosion.
- A potential link between deep-seated faults bisecting the Base Cretaceous Unconformity and fluid migration is observed from the seismic by interpreting features related to fluid flow, often occurring as disturbed reflectors and vertical columnar pipe-like structures.
- Amplitude anomalies are observed on RMS attribute maps extracted from the Torsk Formation. The anomalies are confined to the Torsk Formation and Nordland Group, and appear as lateral extensive anomalies. Many of the anomalies lie parallel to the URU These amplitude anomalies represent shallow accumulations of gas.
- The gas accumulations are mostly confined to a 50km^2 area over the Goliat hydrocarbon reservoirs, except for two accumulations located 3 km further north.
- Most of the shallow gas accumulations are related to faults, both shallow and deep-seated, which could explain their location, as they are situated directly over the Goliat hydrocarbon reservoirs. Only AA1 and AA2 deviated from this trend.
- AA3 – AA10 are situated in an area devoid of pockmarks and depressions, and no direct link between the anomalies and pockmarks have been established. AA1 and AA2, however both area located in areas where pockmarks are present, and so they could be linked.
- Shallow gas accumulations occur because there are obstacles and traps in the shallow sediments. The shallow gas is many places trapped under the URU, indicating that this could act as a semi-impermeable barrier.
- Possible leakage along fault planes are found in several places of the study area. They are often related to pipe-structures and underlying deep-seated faults.
- The origin of polygonal faults in the study area is likely linked to dewatering and compaction. Dewatering of the sediments is also often associated with fluid migration

along the fault planes, where the polygonal faults may act as a plumbing system for a larger area.

- Different sets of faults give rise to several potential migration pathways for fluids in the subsurface. A possible link between the maximum horizontal stresses S_{Hmax} and "open" faults are found. The S_{Hmax} could be a potential explanation behind the shallow gas accumulations in the study area.
- Depressions covering large parts of the seafloor in the study area are interpreted as pockmarks, they are located within depressions and where the seafloor is deeper and the topography is less rugged. They are organized in two groups based on their size and distribution. Small-scale depressions/pockmarks are mostly found in large clusters with a density up to 165/km^2. Isolated depressions are only observed in the shallower parts of the seafloor with a more rugged topography. They are not found to have any relation between free gas and deeper thermogenic sources, but this should not be ruled out.

7 References

ANDERSON, E. M. 1951. *The dynamics of faulting and dyke formation with applications to Britain,* Hafner Pub. Co.

ANDREASSEN, K., LABERG, J. S. & VORREN, T. O. 2008. Seafloor geomorphology of the SW Barents Sea and its glaci-dynamic implications. *Geomorphology,* 97**,** 157-177.

ANDREASSEN, K., NILSSEN, E. G. & ØDEGAARD, C. M. 2007a. Analysis of shallow gas and fluid migration within the Plio-Pleistocene sedimentary succession of the SW Barents Sea continental margin using 3D seismic data. *Geo-Marine Letters,* 27**,** 155-171.

ANDREASSEN, K., NILSSEN, L. C., RAFAELSEN, B. & KUILMAN, L. 2004. Three-dimensional seismic data from the Barents Sea margin reveal evidence of past ice streams and their dynamics. *Geology,* 32**,** 729-732.

ANDREASSEN, K., ØDEGAARD, C. & RAFAELSEN, B. 2007b. Imprints of former ice streams, imaged and interpreted using industry three-dimensional seismic data from the south-western Barents Sea. *Geological Society, London, Special Publications,* 277**,** 151-169.

BAHORICH, M. & FARMER, S. 1995. 3-D seismic discontinuity for faults and stratigraphic features: The coherence cube. *The leading edge,* 14**,** 1053-1058.

BASS, D. & WOODWORTH-LYNAS, C. 1988. Iceberg crater marks on the sea floor, Labrador Shelf. *Marine Geology,* 79**,** 243-260.

BERGLUND, L., AUGUSTSON, J., FÆRSETH, R., GJELBERG, J. & RAMBERG-MOE, H. 1986. The evolution of the Hammerfest Basin. *Habitat of hydrocarbons on the Norwegian continental shelf***,** 319-338.

BERNDT, C. 2005. Focused fluid flow in passive continental margins. *Philosophical Transactions of the Royal Society of London A: Mathematical, Physical and Engineering Sciences,* 363**,** 2855-2871.

BJØRLYKKE, K. 1993. Fluid flow in sedimentary basins. *Sedimentary Geology,* 86**,** 137-158.

BROWN, A. 2000. Evaluation of possible gas microseepage mechanisms. *AAPG bulletin,* 84**,** 1775-1789.

BROWN, A. 2004. Interpretation of three-dimensional seismic data: The American Association of Petroleum Geologists and the Society of Exploration Geophysicists. *Tulsa, OK,* 535.

BULAT, J. 2005. Some considerations on the interpretation of seabed images based on commercial 3D seismic in the Faroe‐Shetland Channel. *Basin Research,* 17**,** 21-42.

BÜNZ, S., MIENERT, J. & BERNDT, C. 2003. Geological controls on the Storegga gas-hydrate system of the mid-Norwegian continental margin. *Earth and Planetary Science Letters,* 209**,** 291-307.

BÜNZ, S., MIENERT, J., BRYN, P. & BERG, K. 2005. Fluid flow impact on slope failure from 3D seismic data: a case study in the Storegga Slide. *Basin Research,* 17**,** 109-122.

CARTWRIGHT, J. 2007. The impact of 3D seismic data on the understanding of compaction, fluid flow and diagenesis in sedimentary basins. *Journal of the Geological Society,* 164**,** 881-893.

CARTWRIGHT, J. 2011. Diagenetically induced shear failure of fine-grained sediments and the development of polygonal fault systems. *Marine and Petroleum Geology,* 28**,** 1593-1610.

CARTWRIGHT, J., JAMES, D. & BOLTON, A. 2003. The genesis of polygonal fault systems: a review. *Geological Society, London, Special Publications,* 216**,** 223-243.

CARTWRIGHT, J. & LONERGAN, L. 1996. Volumetric contraction during the compaction of mudrocks: A mechanism for the development of regional‐scale polygonal fault systems. *Basin Research,* 8**,** 183-193.

CARTWRIGHT, J. A. 1994. Episodic basin-wide fluid expulsion from geopressured shale sequences in the North Sea basin. *Geology,* 22**,** 447-450.

CARTWRIGHT, J. T. & DEWHURST, D. 1998. Layer-bound compaction faults in fine-grained sediments. *Geological Society of America Bulletin,* 110**,** 1242-1257.

CATHLES, L., SU, Z. & CHEN, D. 2010. The physics of gas chimney and pockmark formation, with implications for assessment of seafloor hazards and gas sequestration. *Marine and Petroleum Geology,* 27**,** 82-91.

CAVANAGH, A. J., DI PRIMIO, R., SCHECK-WENDEROTH, M. & HORSFIELD, B. 2006. Severity and timing of Cenozoic exhumation in the southwestern Barents Sea. *Journal of the Geological Society,* 163**,** 761-774.

CHAND, S., MIENERT, J., ANDREASSEN, K., KNIES, J., PLASSEN, L. & FOTLAND, B. 2008. Gas hydrate stability zone modelling in areas of salt tectonics and pockmarks of the Barents Sea suggests an active hydrocarbon venting system. *Marine and Petroleum Geology,* 25**,** 625-636.

CHAND, S. & MINSHULL, T. 2003. Seismic constraints on the effects of gas hydrate on sediment physical properties and fluid flow: a review. *Geofluids,* 3**,** 275-289.

CHAND, S., RISE, L., OTTESEN, D., DOLAN, M., BELLEC, V. & BØE, R. 2009. Pockmark-like depressions near the Goliat hydrocarbon field, Barents Sea: morphology and genesis. *Marine and Petroleum Geology,* 26**,** 1035-1042.

CHAND, S., THORSNES, T., RISE, L., BRUNSTAD, H., STODDART, D., BØE, R., LÅGSTAD, P. & SVOLSBRU, T. 2012. Multiple episodes of fluid flow in the SW Barents Sea (Loppa High) evidenced by gas flares, pockmarks and gas hydrate accumulation. *Earth and Planetary Science Letters,* 331**,** 305-314.

CHAOUCH, A. & MARI, J. 2006. 3-D Land Seismic Surveys: Definition of Geophysical Parameter. *Oil & Gas Science and Technology-Revue de l'IFP,* 61**,** 611-630.

CRÉMIÈRE, A., LEPLAND, A., CHAND, S., SAHY, D., CONDON, D. J., NOBLE, S. R., MARTMA, T., THORSNES, T., SAUER, S. & BRUNSTAD, H. 2016. Timescales of methane seepage on the Norwegian margin following collapse of the Scandinavian Ice Sheet. *Nature communications,* 7.

DAVIES, R., IRELAND, M. & CARTWRIGHT, J. 2009. Differential compaction due to the irregular topology of a diagenetic reaction boundary: a new mechanism for the formation of polygonal faults. *Basin Research,* 21**,** 354-359.

DAVIES, R. J. & IRELAND, M. T. 2011. Initiation and propagation of polygonal fault arrays by thermally triggered volume reduction reactions in siliceous sediment. *Marine Geology,* 289**,** 150-158.

DAVIS, A. 1992. Shallow gas: an overview. *Continental Shelf Research,* 12**,** 1077-1079.

DEWHURST, D. N., CARTWRIGHT, J. A. & LONERGAN, L. 1999. The development of polygonal fault systems by syneresis of colloidal sediments. *Marine and Petroleum Geology,* 16**,** 793-810.

DIMAKIS, P., BRAATHEN, B. I., FALEIDE, J. I., ELVERHØI, A. & GUDLAUGSSON, S. T. 1998. Cenozoic erosion and the preglacial uplift of the Svalbard–Barents Sea region. *Tectonophysics,* 300**,** 311-327.

DORÉ, A. 1991. The structural foundation and evolution of Mesozoic seaways between Europe and the Arctic. *Palaeogeography, Palaeoclimatology, Palaeoecology,* 87**,** 441-492.

DORÉ, A. 1995. Barents Sea geology, petroleum resources and commercial potential. *Arctic***,** 207-221.

DORÉ, A. & JENSEN, L. 1996. The impact of late Cenozoic uplift and erosion on hydrocarbon exploration: offshore Norway and some other uplifted basins. *Global and Planetary Change,* 12**,** 415-436.

DURAN, E. R., DI PRIMIO, R., ANKA, Z., STODDART, D. & HORSFIELD, B. 2013. 3D-basin modelling of the Hammerfest Basin (southwestern Barents Sea): A quantitative assessment of petroleum generation, migration and leakage. *Marine and petroleum geology,* 45**,** 281-303.

EDEN, D. J. & EYLES, N. 2001. Description and numerical model of Pleistocene iceberg scours and ice‐keel turbated facies at Toronto, Canada. *Sedimentology,* 48**,** 1079-1102.

ELDHOLM, O., FALEIDE, J. I. & MYHRE, A. M. 1987. Continent-ocean transition at the western Barents Sea/Svalbard continental margin. *Geology,* 15**,** 1118-1122.

FALEIDE, J., GUDLAUGSSON, S., ELDHOLM, O., MYHRE, A. & JACKSON, H. 1991. Deep seismic transects across the sheared western Barents Sea-Svalbard continental margin. *Tectonophysics,* 189**,** 73-89.

FALEIDE, J. I., GUDLAUGSSON, S. T. & JACQUART, G. 1984. Evolution of the western Barents Sea. *Marine and Petroleum Geology,* 1**,** 123IN1129IN5137-128IN4136IN8150.

FALEIDE, J. I., SOLHEIM, A., FIEDLER, A., HJELSTUEN, B. O., ANDERSEN, E. S. & VANNESTE, K. 1996. Late Cenozoic evolution of the western Barents Sea-Svalbard continental margin. *Global and Planetary Change,* 12**,** 53-74.

FALEIDE, J. I., TSIKALAS, F., BREIVIK, A. J., MJELDE, R., RITZMANN, O., ENGEN, O., WILSON, J. & ELDHOLM, O. 2008. Structure and evolution of the continental margin off Norway and the Barents Sea. *Episodes,* 31**,** 82.

FALEIDE, J. I., VÅGNES, E. & GUDLAUGSSON, S. T. 1993. Late Mesozoic-Cenozoic evolution of the south-western Barents Sea in a regional rift-shear tectonic setting. *Marine and Petroleum Geology,* 10**,** 186-214.

FIEDLER, A. & FALEIDE, J. I. 1996. Cenozoic sedimentation along the southwestern Barents Sea margin in relation to uplift and erosion of the shelf. *Global and Planetary Change,* 12**,** 75-93.

FLOODGATE, G. & JUDD, A. 1992. The origins of shallow gas. *Continental Shelf Research,* 12**,** 1145-1156.

FOSSEN, H. 2016. *Structural geology*, Cambridge University Press.

FOSSEN, H. & GABRIELSEN, R. 2005. Strukturgeologi. *Fagbokforlaget, Staranger*.

GABRIELSEN, R. & FÆRSETH, R. 1989. The off-shore extension of the Trollfjord-Komagelv fault zone—a comment. *Norsk Geologisk Tidsskrift,* 69**,** 57-62.

GABRIELSEN, R. H., FAERSETH, R. B. & JENSEN, L. N. 1990. *Structural Elements of the Norwegian Continental Shelf. Pt. 1. The Barents Sea Region*, Norwegian Petroleum Directorate.

GAY, A. & BERNDT, C. 2007. Cessation/reactivation of polygonal faulting and effects on fluid flow in the Vøring Basin, Norwegian Margin. *Journal of the Geological Society,* 164**,** 129-141.

GOULTY, N. 2008. Geomechanics of polygonal fault systems: a review. *Petroleum Geoscience,* 14**,** 389-397.

GUDLAUGSSON, S., FALEIDE, J., JOHANSEN, S. & BREIVIK, A. 1998. Late Palaeozoic structural development of the south-western Barents Sea. *Marine and Petroleum Geology,* 15**,** 73-102.

GUERIN, G. & GOLDBERG, D. 2002. Sonic waveform attenuation in gas hydrate‐bearing sediments from the Mallik 2L‐38 research well, Mackenzie Delta, Canada. *Journal of Geophysical Research: Solid Earth,* 107.

GUZZETTA, G. & CINQUEGRANA, R. 1987. "Fluid tectonics": a little appreciated facet of buoyancy tectonics. *Tectonophysics,* 139**,** 321-324.

HARLAND, W. B. 1969. Contribution of Spitsbergen to Understanding of Tectonic Evolution of North Atlantic Region: Chapter 58: Arctic Regions.

HENRIET, J., DE BATIST, M., DE BRUYNE, H., HELDENS, P., HUYLEBROECK, J., MOSTAERT, F., SEVENS, E., AUFFRET, J. & D'OLIER, B. 1989. Preliminary seismic-stratigraphic maps and type sections of the Paleogene deposits in the Southern Bight of the North Sea. *The Quaternary and Tertiary Geology of the Southern Bight, North Sea. Belgian Geological Survey, Ministry Economic Affairs (Brussels)***,** 29-44.

HENRIKSEN, E., BJØRNSETH, H., HALS, T., HEIDE, T., KIRYUKHINA, T., KLØVJAN, O., LARSSEN, G., RYSETH, A., RØNNING, K. & SOLLID, K. 2011. Uplift and erosion of the greater Barents Sea: impact on prospectivity and petroleum systems. *Geological Society, London, Memoirs,* 35**,** 271-281.

HOVLAND, M. 1981. Characteristics of pockmarks in the Norwegian Trench. *Marine Geology,* 39**,** 103-117.

HOVLAND, M. 2007. Discovery of prolific natural methane seeps at Gullfaks, northern North Sea. *Geo-Marine Letters,* 27**,** 197-201.

HOVLAND, M., GARDNER, J. & JUDD, A. 2002. The significance of pockmarks to understanding fluid flow processes and geohazards. *Geofluids,* 2**,** 127-136.

INDREVÆR, K., GABRIELSEN, R. H. & FALEIDE, J. I. 2017. Early Cretaceous synrift uplift and tectonic inversion in the Loppa High area, southwestern Barents Sea, Norwegian shelf. *Journal of the Geological Society,* 174**,** 242-254.

JUDD, A. & HOVLAND, M. 2007. Seabed fluid flow—the impact on geology. *Biology and the Marine Environment*.

JUDD, A. & HOVLAND, M. 2009. *Seabed fluid flow: the impact on geology, biology and the marine environment*, Cambridge University Press.

KARLSEN, D. & SKEIE, J. 2006. Petroleum migration, faults and overpressure, part I: Calibrating basin modelling using petroleum in traps—a review. *Journal of Petroleum Geology,* 29**,** 227-256.

KING, L. Aspects of regional surficial geology related to site investigation requirements- eastern Canadian shelf. Mar 1979, 34 p, Preprints: Offshore Site Investigation Conference, 1980.

KING, L. H. & MACLEAN, B. 1970. Pockmarks on the Scotian shelf. *Geological Society of America Bulletin,* 81**,** 3141-3148.

KNUTSEN, S.-M. & LARSEN, K. 1997. The late Mesozoic and Cenozoic evolution of the Sørvestsnaget Basin: A tectonostratigraphic mirror for regional events along the Southwestern Barents Sea margin? *Marine and petroleum geology,* 14**,** 27-54.

KVENVOLDEN, K. 1998. A primer on the geological occurrence of gas hydrate. *Geological Society, London, Special Publications,* 137**,** 9-30.

LABERG, J., ANDREASSEN, K. & KNUTSEN, S.-M. 1998. Inferred gas hydrate on the Barents Sea shelf—a model for its formation and a volume estimate. *Geo-Marine Letters,* 18**,** 26-33.

LEITH, T., WEISS, H., MØRK, A., ÅRHUS, N., ELVEBAKK, G., EMBRY, A., BROOKS, P., STEWART, K., PCHELINA, T. & BRO, E. 1992. Mesozoic hydrocarbon sourcerocks of the Arctic region. *Arctic Geology and Petroleum Potential, Norw. Petrol. Soc. Spec. Publ,* 2**,** 1-25.

LIGTENBERG, J. 2005. Detection of fluid migration pathways in seismic data: implications for fault seal analysis. *Basin Research,* 17**,** 141-153.

LINJORDET, A. & OLSEN, R. G. 1992. The Jurassic Snohvit Gas Field, Hammerfest Basin, Offshore Northern Norway: Chapter 22.

LIU, X. & FLEMINGS, P. B. 2006. Passing gas through the hydrate stability zone at southern Hydrate Ridge, offshore Oregon. *Earth and Planetary Science Letters,* 241**,** 211-226.

LONERGAN, L., CARTWRIGHT, J. & JOLLY, R. 1998. The geometry of polygonal fault systems in Tertiary mudrocks of the North Sea. *Journal of Structural Geology,* 20**,** 529-548.

LONERGAN, L. & CARTWRIGHT, J. A. 1999. Polygonal faults and their influence on deep-water sandstone reservoir geometries, Alba Field, United Kingdom central North Sea. *AAPG bulletin,* 83**,** 410-432.

LØSETH, H., GADING, M. & WENSAAS, L. 2009. Hydrocarbon leakage interpreted on seismic data. *Marine and Petroleum Geology,* 26**,** 1304-1319.

LØSETH, H., WENSAAS, L., ARNTSEN, B., HANKEN, N.-M., BASIRE, C. & GRAUE, K. 2011. 1000 m long gas blow-out pipes. *Marine and Petroleum Geology,* 28**,** 1047-1060.

MIENERT, J., POSEWANG, J. & BAUMANN, M. 1998. Gas hydrates along the northeastern Atlantic margin: possible hydrate-bound margin instabilities and possible release of methane. *Geological Society, London, Special Publications,* 137**,** 275-291.

MURILLO, W. A., VIETH-HILLEBRAND, A., HORSFIELD, B. & WILKES, H. 2016. Petroleum source, maturity, alteration and mixing in the southwestern Barents Sea: New insights from geochemical and isotope data. *Marine and Petroleum Geology,* 70**,** 119-143.

MYHRE, A. M. & ELDHOLM, O. 1988. The western Svalbard margin (74–80 N). *Marine and Petroleum Geology,* 5**,** 134-156.

NILSEN, K. T., VENDEVILLE, B. C. & JOHANSEN, J.-T. 1995. Influence of regional tectonics on halokinesis in the Nordkapp Basin, Barents Sea.

NORTH, F. 1985. *Petroleum geology,* Springer.

NYLAND, B., JENSEN, L., SKAGEN, J., SKARPNES, O. & VORREN, T. 1992. Tertiary uplift and erosion in the Barents Sea: magnitude, timing and consequences. *Structural and tectonic modelling and its application to petroleum geology, Norwegian Petroleum Society (NPF) Special Publication,* 1**,** 153-162.

OHM, S. E., KARLSEN, D. A. & AUSTIN, T. 2008. Geochemically driven exploration models in uplifted areas: Examples from the Norwegian Barents Sea. *AAPG bulletin,* 92**,** 1191-1223.
OSTANIN, I., ANKA, Z., DI PRIMIO, R. & BERNAL, A. 2012. Identification of a large Upper Cretaceous polygonal fault network in the Hammerfest basin: Implications on the reactivation of regional faulting and gas leakage dynamics, SW Barents Sea. *Marine Geology,* 332**,** 109-125.
OSTANIN, I., ANKA, Z., DI PRIMIO, R. & BERNAL, A. 2013. Hydrocarbon plumbing systems above the Snøhvit gas field: structural control and implications for thermogenic methane leakage in the Hammerfest Basin, SW Barents Sea. *Marine and Petroleum Geology,* 43**,** 127-146.
PAU, M., HAMMER, Ø. & CHAND, S. 2014. Constraints on the dynamics of pockmarks in the SW Barents Sea: evidence from gravity coring and high-resolution, shallow seismic profiles. *Marine Geology,* 355**,** 330-345.
PETRACCHINI, L., ANTONELLINI, M., BILLI, A. & SCROCCA, D. 2015. Syn-thrusting polygonal normal faults exposed in the hinge of the Cingoli anticline, northern Apennines, Italy. *Frontiers in Earth Science,* 3**,** 67.
SALES, J. K. 1993. Closure vs. seal capacity—A fundamental control on the distribution of oil and gas. *Basin modeling: Advances and application: Norwegian Petroleum Society (NPF) Special Publication,* 3**,** 399-414.
SELLEY, R. C. & SONNENBERG, S. A. 2014. *Elements of petroleum geology,* Academic Press.
SHERIFF, R. 1980. Seismic stratigraphy, published by International Human Resources Development Corporation. *Boston, Massachusetts***,** 85-116.
SHERIFF, R. 1985. Aspects of Seismic Resolution: Chapter 1.
SHERIFF, R. E. 1992. *Reservoir geophysics,* Soc of Exploration Geophysicists.
SHERIFF, R. E. 2012. *Seismic stratigraphy,* Springer Science & Business Media.
SLOAN, E. & KOH, C. 1998. Hydrates of natural gases. New York: Marcel Dekker.
SLOAN, E. D. 1998. Gas hydrates: Review of physical/chemical properties. *Energy & Fuels,* 12**,** 191-196.
SLOAN JR, E. D. & KOH, C. 2007. *Clathrate hydrates of natural gases,* CRC press.
SMELROR, M., PETROV, O., LARSSEN, G. B. & WERNER, S. 2009. Geological history of the Barents Sea. *Norges Geol. undersøkelse***,** 1-135.
SOLHEIM, A. & ELVERHØI, A. 1985. A pockmark field in the Central Barents Sea; gas from a petrogenic source? *Polar research,* 3**,** 11-19.
STORVOLL, V., BJRLYKKE, K. & MONDOL, N. H. 2005. Velocity-depth trends in Mesozoic and Cenozoic sediments from the Norwegian Shelf. *AAPG bulletin,* 89**,** 359-381.
STUEVOLD, L. M., FAERSETH, R. B., ARNESEN, L., CARTWRIGHT, J. & MÖLLER, N. 2003. Polygonal faults in the Ormen Lange field, Møre basin, offshore mid Norway. *Geological Society, London, Special Publications,* 216**,** 263-281.
SUN, Q., WU, S., LÜ, F. & YUAN, S. 2010. Polygonal faults and their implications for hydrocarbon reservoirs in the southern Qiongdongnan Basin, South China Sea. *Journal of Asian Earth Sciences,* 39**,** 470-479.
SVENDSEN, J. I., GATAULLIN, V., MANGERUD, J. & POLYAK, L. 2004. The glacial history of the Barents and Kara Sea region. *Developments in Quaternary Sciences,* 2**,** 369-378.
TWISS, R. J. & MOORES, E. M. 1992. *Structural geology,* Macmillan.
VADAKKEPULIYAMBATTA, S., BÜNZ, S., MIENERT, J. & CHAND, S. 2013. Distribution of subsurface fluid-flow systems in the SW Barents Sea. *Marine and Petroleum Geology,* 43**,** 208-221.
VEEKEN, P. C. 2013. *Seismic Stratigraphy and depositional facies models,* Academic Press.
VORREN, T. O., RICHARDSEN, G., KNUTSEN, S.-M. & HENRIKSEN, E. 1991. Cenozoic erosion and sedimentation in the western Barents Sea. *Marine and Petroleum Geology,* 8**,** 317-340.
WHITICAR, M. J. 1994. Correlation of natural gases with their sources. *Memoirs-American Association of Petroleum Geologists***,** 261-261.
WIDESS, M. 1973. How thin is a thin bed? *Geophysics,* 38**,** 1176-1180.

WINSBORROW, M. C., ANDREASSEN, K., CORNER, G. D. & LABERG, J. S. 2010. Deglaciation of a marine-based ice sheet: Late Weichselian palaeo-ice dynamics and retreat in the southern Barents Sea reconstructed from onshore and offshore glacial geomorphology. *Quaternary Science Reviews,* 29**,** 424-442.

WORSLEY, D. 2008. The post‐Caledonian development of Svalbard and the western Barents Sea. *Polar Research,* 27**,** 298-317.